SYNTHESIS, CHARACTERIZATION, AND FILM FABRICATION OF INORGANIC AND HYBRID SEMICONDUCTOR MATERIALS FOR OPTOELECTRONIC APPLICATIONS

by

WOOSEOK KI

A Dissertation submitted to the

Graduate School – New Brunswick

Rutgers, The State University of New Jersey

in partial fulfillment of the requirements

for the degree of

Doctor of Philosophy

Graduate Program in Chemistry and Chemical Biology

written under the direction of

Professor Jing Li

and approved by

_____

_____

_____

_____

New Brunswick, New Jersey

October, 2008

ABSTRACT OF THE DISSERTATION

Synthesis, Film Fabrication and Characterization of Inorganic and Hybrid Semiconductor Materials for Optoelectronic Applications

by

WOOSEOK KI

Dissertation Director:

Professor Jing Li

We have developed and studied selected properties of a novel type of inorganic-organic hybrid semiconductor materials in order to enhance the functionality over their parent structures. Since these hybrid semiconductor materials are composed of both inorganic and organic segments, one may expect them to have the advantage of combining the excellent electrical, optical, thermal and transport properties from the inorganic component with the flexibility, processability and structural diversity from the organic component. As a continuing effort, we have synthesized, modified, and characterized a number of selected structures with potential for solid state lighting applications. For example, we have developed the first inorganic-organic semiconductor bulk material, double-layered 2D-Cd_2Q_2(*ba*)(Q = S, Se), capable of producing direct white light. This type of materials could be promising for use as a single-material white-light-emitting source in white LEDs. Luminescence properties of these hybrid

semiconductors can be tuned systematically by changing their composition and doping level. In addition, a thin pellet of one of our hybrid semiconductor materials without any modifications showed low electrical conductivity. Significant improvement may be anticipated with compositional and structural modifications on this system.

Solution processed deposition techniques provide great opportunities for optical and optoelectronic devices, such as displays, solid state lighting, and solar cells, because it enables to fabricate flexible devices with low-cost and large area fabrications. Most semiconductors show very low solubility in organic solvents, thus limiting the opportunities to prepare thin films using soluble precursors. In this study, we have developed a simple, efficient, and low-cost solution-processed deposition route to fabricate metal chalcogenide semiconductor thin films by using soluble precursors via spin-coating techniques. Surface morphology was directly influenced by the choice of organic solvents as well as the spin-coating sequences, thus affecting the electrical transport of the films. In the case of hybrid semiconductors, a conducting polymer was employed to help forming more uniform composite films.

ACKNOWLDEGEMENTS

First, I would like to give thanks to my LORD GOD who is the Alpha and the Omega.

I would like to express my deepest gratitude to my advisor Dr. Jing Li, a wonderful advisor as well as a mentor, for her guidance, advice, and constant support in helping me to conduct and complete this work. Without her insight and encouragement, it would not be possible to finish this research. I also thank her for many casual conversations about numerous aspects that are invaluable and very helpful for preparing me for my future carrier.

I would also like to gratefully thank Dr. John Brennan, Dr. Eric Garfunkel, and Dr. Dunbar Birnie not only for serving on my thesis committee, but also for their valuable comments and suggestions.

I would like to thank our collaborators, Dr. Gene Hall for serving as an in-field proposal committee as well as for sample analysis, Dr. Thomas J. Emge and Dr. Xiaoying Huang for helping analyze single crystal data, Dr. David L. Young, Dr. Sangwook Cheong, Dr. Hongxing Jiang, Dr. Yong Zhang and Dr. Manish Chhowalla for measuring electrical and optical properties of our samples.

Many thanks to all members of Dr. Li's research group: Dr. Long Pan, Dr. Jeongyong Lee, Dr. Kunhao Li, Dr. Moothetty Padmanabhan, Gary DiFilippo, Princy Varughese, and Sanhita Pramanik for their help and friendship, and my undergraduate students, Sri Reddy, Ashay Patel, and Jonathan Burg for their hard work in sample preparation and characterization.

I owe my sincere appreciation to my family: my mother, Kui-Le Lee who gave birth to me, raised me, and loved me and also my brothers and sisters for invaluable support, care, and love.

I would like to thank my in-law parents, brothers, and sisters for their support, love, and prayer over the years.

I am also grateful to Pastor Lee's family for their mentoring and prayer during my studies.

Finally and most of all, I greatly thank my beloved wife, Jieun Youn for her love, support, patience, and prayer over the past years of our marriage.

Financial supports from the National Science Foundation (DMR-0422932 and DMR-0706069) are gratefully appreciated.

DEDICATION

To

My God and my Ezer, Jieun Youn

TABLE OF CONTENTS

LIST OF TABLES

LIST OF FIGURES

LIST OF ABBREVIATIONS

en	ethylenediamine
pda	1,3-propanediamine
bda	1,4-butanediamine
ptda	1,5-pentanediamine
hda	1,6- hexanediamine
N_2H_4	hydrazine
$N_2H_4 \cdot H_2O$	hydrazine monohydrate
ea	ethylamine
pa	*n*-propylamine
ba	*n*-butylamine
pta	pentylamine
ha	*n*-hexylamine
1D	One-dimensional
2D	Two-dimensional
3D	Three-dimensional
CBD	Chemical bath deposition
TFT	Thin film transistor
SSL	Solid state lighting
LED	Light emitting diode
PXRD	Powder X-ray diffraction
TGA	Thermogravimetric analysis
AFM	Atomic force microscope

SEM	Scanning electron microscope
CIE	International commission on illumination
PL	Photoluminescence

CHAPTER ONE

Introduction

II-VI semiconductor materials are composed of two different elements from group II and group VI in the periodic table. These materials have made great impact in modern society because of their importance in electronic and optical applications, and because their physical properties can be tailored by simple modifications, such as doping, size, and shape.[1] They have played a major role in applications such as light emitting diodes, transistors, and photovoltaic solar cells. In particular, the past two decades have witnessed rapid progression in the field of photovoltaic solar cell technology around the world with the hope of producing materials capable of meeting our energy needs as a fascinating renewable energy source.[2]

A solar cell is a semiconductor device based on the photovoltaic effect, where light is converted to electrical energy. Research in this field can be divided into two areas: making cheaper and more efficient solar cells to effectively compete with other energy sources; and developing new materials to serve as light absorbers and charge carriers.

Numerous semiconductors have been developed that are both highly efficient and economically competitive for solar cell applications. The maximum conversion efficiency (η) that can be expected for single-junction solar cells with inorganic semiconductors at room temperature is 25%.[2(a)] A further increase of η can be achieved by using two-junction tandem cells with optimum gaps of 0.9-1.1eV and 1.6-1.8eV as well as by employing single junction cells with an optimum gap of 1.3-1.5eV.[3] Based on these findings, it is crucial to find suitable materials with optimum energy gaps to achieve high conversion efficiencies for photovoltaic applications.

Commercially available photovoltaic modules with relatively high efficiency, up to 24.4%, are wafer based crystal silicon solar cells possessing excellent stability and

reliability.[4] The main disadvantage of this technology is, however, the high photovoltaic module price, due to in part of the substantial amount of fabrication energy required to produce modules. On the other hand, thin film solar cells based on metal chalcogendies, such as cadmium telluride (CdTe) and copper indium diselenide (CIS) and copper indium gallium diselenide (CIGS), are substantially cheaper and involve more simple fabrication steps than wafer-based silicon modules.[2]

Thin film research is advantageous for photovoltaic applications since materials in the form of thin films reduce manufacturing costs and require fewer processing steps for PV modules and systems. To prepare photovoltaic semiconductor thin films, a large variety of thin film deposition techniques have been exploited in order to improve photovoltaic performance. In fact, the choice of any given deposition technology is based on the highest achievable efficiency, ease of manufacturing, reliability, and availability.

Most deposition methods are performed under high temperature or high vacuum. Such methods include chemical vapor deposition (CVD), physical vapor deposition (PVD), close-space vapor deposition (CSVT), electrodeposition, thermal evaporation, and sputtering.[5] For instance, $CuInSe_2$ thin films can approach the efficiency of the best polycrystalline Si wafer, because $CuInSe_2$ and its alloys are direct band gap semiconductors, where the band gap can be tuned from 1.0 to 2.68 eV by controlling alloy composition by thermal evaporation. [6]

The solar cells based on $Cu(In,Ga)Se_2$ films have produced the most efficient thin film for devices and modules over 19%.[7] These solar cells have been made by elemental source co-evaporation which requires a substrate temperature of 500°C as well as incorporation of Na into the film. Those processes however require high vacuum and

often high temperature. Since maintaining the vacuum is expensive and most process chambers are small, it will be obstacles to fabricate large area devices.

Currently, the “soft” process techniques, such as spin casting, chemical bath deposition, and stamping/printing, are of great interest, since they are suitable to process cost effective, flexible, and large area thin films at relatively low temperatures. Moreover, new solar cell device and optoelectronic devices have been extensively produced towards the next generation of photovoltaic modules based on solution processed deposition techniques.

Chemical bath deposition (CBD) is one of the most common techniques used to fabricate binary and ternary metal chalcogenide thin films for various applications, such as field effect transistors and photovoltaic solar cells.[8] The fundamental growth mechanism for CBD method is analogous to the CVD technique, except that the whole reaction in CBD takes place in solution. In general, the mechanism of CBD has been explained by using one of three models based on the choice of starting materials: ion-by-ion mechanism, hydroxide cluster mechanism, and complex-decomposition mechanism. Figure 1. shows a schematic diagram of the hydroixde cluster mechanism with cadmium sulfide (CdS) crystals.[9]

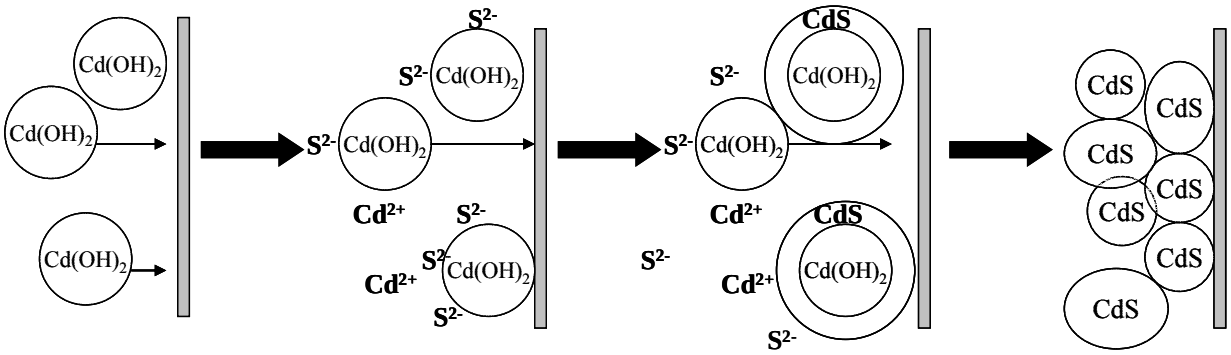

Figure 1 A schematic diagram of possible steps in the hydroxide mechanism

The initial step in this mechanism is adhesion of the hydroxide to the substrate and followed by continuous reaction with sulfur ions. This reaction will continue until hydroxide is converted to sulphide. Finally the particle of CdS will adhere to each other forming an aggregated film.

Many efforts have been made to improve electrical properties of CdS fabricated from CBD techniques. For instance, resistivity of CdS films decreased by administrating subsequent annealings in S_2 and indium/hydrogen as well as by thermal diffusion of indium.[10] This result found that annealing in a hydrogen environment reduces the film's resistivity by passivating the chemiabsorbed oxygen in the grain boundary. Chang *et al*., reported CdS thin film transistors that the field effect mobility was found to be 1.5cm^2/Vs.[8(d)] Although many efforts have been made to improve mobility of CdS thin film, most value of field effect mobility has been shown around 0.1~2 $cm^2V^{-1}s^{-1}$.[8(e)-8(g)]

A burgeoning area for use of CBD technique is in photovoltaic solar cell applications. The efficiency of CdS/CdTe solar cells was much improved by varying the thiourea/$CdCl_2$ ratio in the chemical bath solution used for the deposition of the CdS

layers as well as changing Cd sources.[11-12]

Thin films by CBD techniques, however, show relatively poor electrical properties due to surface scattering from grain boundary or impurities. In addition, characteristics of thin films are also strongly dependent on preparation conditions such as temperature, stirring, and concentration of precursors.

Another method to fabricate semiconductor thin films using solution processed deposition is spin coating techniques.[13] Spin coating is a simple technique for fabricating thin films onto various substrates in order to obtain uniform and continuous film. It is used in the preparation of films for various applications, such as dielectric/insulating layers, magnetic disk coatings, head lubricants, and organic display coatings. The target thin film is formed by depositing a coating solution and removing the remaining solution during spinning off. Precursors must be dissolved or dispersed into a solvent.

Because of these simple and cost effective procedures, spin coating techniques have been widely employed to make uniform and continuous film for optoelectronic applications, such as thin film transistors (TFTs) and photovoltaic solar cells. Current studies have demonstrated the first spin-coated inorganic thin film semiconductors, such as $CuInSe_2$, SnS_2 and $SnS_{2-x}Se_x$ for TFTs applications.[14] Mitzi *et al*. published the first report on the spin coating process of inorganic semiconductor thin films of SnS_2 and $SnS_{2-x}Se_x$ using a hydrazine based precursor.[14(a)] The mobility of $SnS_{2-x}Se_x$ films was reported to be greater than 10 $cm^2/V{\cdot}s$, an order of magnitude higher than the previously reported values. Pütz and Aegerter also reported spin coated MoS_2 film using organic amine to dissolve a precursor, $(NH_4)_2MoS_4$. However, there were no reported data on electrical properties.[14(c)]

Although very promising for device performance, semiconductor materials are often limited in use of solution processed techniques due to the low solubility of semiconductors in conventional solvents, the difficulties in finding suitable the solvents, undesirable reactions between solvents and precursors, and the toxicity of the solvents, such as hydrazine. In addition, it is difficult to form continuous and uniform films due to the evaporation driven surface tension effect. For these reasons, the solution processed deposition by spin coating is rarely used for thin films fabrications.

As a complimentary counterpart of inorganic counterparts, organic materials have recently received considerable attention for their possible use in various applications, such as photovoltaic solar cells, light emitting diodes (LEDs), and TFTs, because of their simple and low temperature fabrication. For example, the most common types of organic thin films, produced by spin coatings, are polymer based photovoltaic devices due to polymer's high solubility in common solvents. This offers an open opportunity for cost-effective, easy of processing, and large area fabrication. The Yang group fabricated highly efficient polymer solar cells based on a bulk heterojunctions of polymer poly(3-hexylthiophene) and methanofullerene by spin coating techniques.[15] They improved solar cell efficiency by controlling the active layer growth rate which caused an increased hole mobility and balanced charge transport. η was 4.4%. Kim *et al*.,[16] also fabricated new tandem polymer solar cells showed high power conversion efficiency, more than 6%. Each layer was deposited by polymer solution to make bulk heterojunction materials comprised of semiconducting polymers and fullerene derivatives.

While very promising with regard to ease of processing and cost-effective fabrication, organic compounds have critical disadvantages, including poor thermal,

mechanical, electrical transport. Over last few years, although a great progress has been made in organic materials to improve mobility, it is fundamentally limited by the bonding nature of organic molecules, such as weak van der Waals bonding compared to inorganic materials having strong covalent boding.[17] For instance, the most high carrier mobilities (>1 $cm^2/V•s$) of organic channel layers in organic field effect transistors have been obtained by vapor-deposition.[18-20]

Another rapidly growing application of semiconductor material researches has been studied on solid state lighting (SSL). SSL technology uses semiconducting materials to convert electricity into lights in the form of LEDs or organic light emitting devices (OLEDs). In the midst of rising power consumption, it is necessary to find energy saving technologies. It has been reported that SSL would reduce the global electricity used for lighting by ~50% by replacing conventional light sources by 2025.[21]

Tremendous efforts have been made to produce white light emitting devices with LED or OLED. To achieve white light emission, two paths have been developed, such as phosphorous conversion and Red-Green-Blue (RGB) systems. The Phosphor conversion approach is based on a blue or near ultraviolet (UV) LED coated with single or multiple phosphors. The most common way for the phosphor conversion to produce white light is to use blue LED and a yellow phosphor (usually cerium-doped yttrium aluminum garnet, YAG:Ce).[22] However, because of the low absorption efficiency of blue light, it leads to limit those materials' ability to achieve a good color rendering index and high conversion efficiency. For example, these white LEDs are not applicable for certain applications due to the fact that the white light generated is "cold". In order to obtain "warm" white light, several studies were performed by using two phosphors, such as YAG:Ce and yellow-

orange phosphors for the purposes of achieving good color rendering to enhance red emission.[23]

In the long term, the RGB approach by blending red, green, and blue phosphor might be favorable because of the high color rendering index. In addition, photons from each phosphor directly contribute to the white light intensity. However, individual colored LEDs respond differently to drive voltage, operating temperature, thus requiring a well controlled system. To overcome those problems, a recent discovery shows that "magic size" CdSe quantum dots (QDs) give rise to white-light emission spanning the entire visible spetrum, as a direct result of very high surface-to-volume ratio and, thus, a significantly larger number of midgap surface sites.[24] These ultrasmall QDs are promising for use as a direct white-light phosphor without involving complicated doping/mixing procedures as well as significant reduction of device efficiency due to problems such as self-absorption, relatively low light capture efficiency of phosphors, or nonradiative carrier losses.[25]

The synthesis and fabrication of novel semiconductor materials made of very different components with enhanced properties and performance provides a great new opportunity for the development of advanced technology. An increasing interest in developing inorganic-organic hybrid semiconductor materials is currently being pursued.[26] Since inorganic-organic hybrid materials are composed of inorganic and organic segments, one may expect them to have the advantage of combining the superior electrical, optical, thermal and transport properties from the inorganic component with the flexibility, processability and structural diversity from organic component in a single structure.

The novel electronic and optical properties of hybrid semiconductors have shown promise for the potential for applications in optoelectronic devices, such as photovoltaic solar cells and LEDs due to their broad band gap tunability and high adsorption coefficients. In particular, incorporation of inorganic nano-crystals into conjugate polymers has become a popular approach to prepare hybrid materials not only in order to improve carrier mobilities, but also to enhance absorption coefficients, photoconductivity, and tunability stemming from particle size. For example, hybrid photovoltaic devices produced by incorporating inorganic nanocrystal CdSe into conjugate polymer poly-3 hexylthiophene (P3HT) exhibits a solar energy conversion efficiency, η, of 1.7% by varying inorganic semiconductor size, resulting in an enhancement of absorption coefficient compared to bulk semiconductor.[27]

LEDs based on inorganic QDs coated with organic polymers also represent a very interesting class of materials for light emission.[28] Inorganic semiconductor colloidal quantum QDs by solution based organometallic synthetic methods are highly preferred in the past decade, because of their narrow size distribution, controllable shape, and optical tenability. This property stems from changing particle size, resulting in modification of optical and electric properties. Organic polymers also have a great advantage in terms of fabrication process. This combination allows large area fabrication by wet solution techniques with low costs. Recently, Seth Coe *et al*.[29] fabricated quantum dots light emitting diodes (QDs-LED) by combining inorganic QDs with organic bilayers via phase separation. This system provides electroluminescence quantum efficiency of light (~2%), and also narrow emission spectra compared to organic LEDs. A remaining challenge, however, is that inorganic colloidal QDs show low conductivity and carrier mobility, thus

reducing electroluminescence efficiency in QDs blended in polymer system, because of the weak correlations between individual dots.

In order to retain excellent transport properties of inorganic semiconductors, while introducing property tunability, we have recently developed a very unique class of II-VI inorganic-organic hybrid semiconductor materials.[30] The II-VI (inorganic) component in these structures forms layers (slabs) or chains (rods) which are separated by organic amine molecules (spacers) through chemical (coordinative) bonds. The II-VI structure motifs are single sized and uniformly (perfectly) ordered and are at the nanoscopic or subnanoscopic scale (at least in one dimension). Thus, the quantum confinement effect (QCE) induced by the organic spacers (very much the same as in passivated colloidal quantum dots) are independent of particle size. These crystal structures can be considered as perfectly ordered quantum wires (in the case of 1D II-VI chains) and quantum wells (in the case of 2D II-VI layers). In addition, blending two very different components in a single structure offers new functionality and enhanced properties that can't be achieved over their parent bulk semiconductors. For example, nearly zero uniaxial thermal expansion (ZTE) behavior of a group of 3D-ZnTe$(L)_{1/2}$ [L= N_2H_4, ethylenediamine, propyldiamine, butyldiamine, and pentyldiamine] has been observed. The ZTE behavior originates from compensation of contraction and expansion of two different components along the inorganic-organic stacking axis.[31]

These nanostructured hybrid semiconductor materials not only exhibit the same level of strong QCE as that of colloidal QDs, but more importantly, they have perfectly ordered periodic structures which allows the same level of strong carrier correlations as in the pure inorganic lattices and thus, high conductivity and carrier mobility may be

anticipated. With their broad band gap tunability and high adsorption coefficients (e.g., 10^6 cm^{-1}), they are promising for applications in optoelectronics including solar cells and light emitting diodes. These unique hybrid semiconductor materials have been synthesized via simple and mild solvothermal (hydrothermal) reactions.

Solvothermal and hydrothermal synthesis offers an effective route for making new inorganic and inorganic-organic hybrid materials with unique structures and interesting optical and electronic properties. Solvothermal reactions make use of organic solvents at elevated temperatures and pressures in a sealed container, while hydrothermal reactions occur in aqueous solution. In general, these reactions take place above the normal boiling point of the solvent used. Under mild solvothermal conditions, some physical and chemical properties of the solvents changes significantly thus affecting its reactivity or solubility. This enables the reaction to occur at significantly lower temperature and to generate new kinetic phases.[32] For these reasons, solvothermal method has been widely employed for synthesis of various functional inorganic-organic materials.[30,33]

In this thesis, as a continuing study of II-VI inorganic-organic hybrid semiconductor materials, we have expanded their structure space to include structures containing conjugated organic spacers, and we have modified and optimized selected systems to investigate their optical and electrical properties toward optoelectronic applications.

Some of these inorganic-organic hybrid semiconductor materials we have been developed are applicable in novel applications, such as SSL. Our recent study,[34] using a 360nm UV-LED coated with our hybrid materials, showed that they are promising

materials for SSL technologies. For practical applications, we have exploited several other processing techniques to process film samples of selected hybrid materials from bulk samples.

To make devices, as stated earlier, fabrication of thin films of inorganic-organic hybrid materials by solution techniques is quite challenging, because of their poor solubility. Although Kagan *et al*.,[35] demonstrated organic-inorganic hybrid thin films using the 2D layered perovskite structure of $(C_6H_5C_2H_4NH_3)_2SnI_4$ as the semiconducting channel for thin film transistor applications by using spin coating techniques, only a few hybrid materials can be dissolved in organic solvents. Therefore, our strategy is to use conjugate polymers in preparing hybrid films along with the assistance of ultrasonication. By applying ultrasonication to a polymer solution mixed with hybrid materials, we are able to create micro- or nano-sized particles suspended in solution, which is then deposited onto substrates by spin coating.

In order to make use of solution based deposition via spin coating techniques, we have also investigated a convenient solution synthetic route to fabricate II-VI and VI-VI semiconductor thin films using soluble precursors. The experimental procedure involved three steps: (a) Synthesizing the precursors first. (b) Dissolving the precursors in suitable organic solvent. (c) Depositing this solution onto substrates via spin coating. The concept of solution processed thin film fabrication of metal chalcogenides is illustrated in Scheme 1.

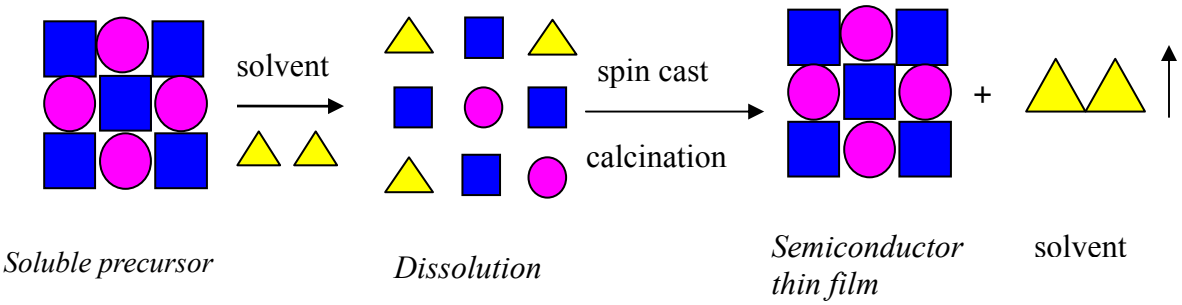

Scheme1. Schematic diagram of solution processed deposition for preparation of thin film (violet sphere: metal; blue square: chalcogen; yellow triangle: solvent)

Because of their potential applications of inorganic semiconductors, as described earlier, their optical and electrical properties have been studied to characterize the thin films. Interestingly, electrical properties of thin film are significantly influenced by the organic solvent used to dissolve the precursor due to each solvent's different wettability, viscosity, and vapor pressure. In addition, surface morphology significantly changed depending on the concentration of the precursors.

In next two chapters, we have explored film fabrications of metal chalcogenide semiconductors using soluble precursors via spin coating techniques which could offer another possible direction towards preparing large area and low-cost fabrications for potential applications such as TFTs, LEDs, and photovoltaic solar cells. Chapter 4 and 5 describe synthesis, characterization, and properties of inorganic-organic hybrid semiconductor materials. In chapter 6, film fabrication of those hybrid materials have been investigated by using a conducting polymer.

Reference

1. (a)Yang, H.; Santra, S. and Holloway, P. H. *J. Nanosci. & Nanotech*., **2005**, *5*, 1364. (b) Alivisatos, A.P. *Science* **1996,** *271,* 933 (c) Kumar, S and Nann, T. *Small* **2006**, *2*, 316

2. (a) Shah, A., Torres, P., Tscharner, R., Wyrsch, N. and Keppner, H. Science **1999,** *285,* 692 (b) Gunes, S.; Neugegauer, H. and Sariciftci, N.S. *Chem. Rev.* **2007**, *107*, 1324. (c) Barnham, K. W. J.; Mazzer, M. and Clive, B. *Nat. Mater.* **2006**, *5*, 161 – 164

3. Aruchamy, A. Photoelectrochemistry and Photovoltaics of Layered Semiconductors, Kluwer Academic Publishers (**1992**)

4. Zhao, J.; Wang, A.; Green, M. A. and Ferrazza, F. *Appl. Phys. Lett*. **1998**, *73*, 1991

5. (a) Guha, S. *Sol. Energy* **2004**, 77, 887. (b) Trigo, J. F.; Asenjo, B.; Herrero, J. and Gutiérrez, M. T. *Sol. Energy Mater. Sol. Cells* **2008***, 92,* 1145. (c) Brith, J. and Ferekides, C. *Appl. Phys. Lett.* **1993**, *62*, 2851. (d) Rakhshani, A. E. *J. Appl. Phys.* **2001**, *90***,** 4265. (e) Dharmadasa, I. M.; Samantilleke, A. P.; Chaure, N. B. and Young, J. *Semicond. Sci. Technol.* **2002**, *17***,** 1238. (f) Fulop, G.; Doty, M.; Meyers, P.; Betz, J. and Liu, C. H. *Appl. Phys. Lett.* **1982**, *40*, 327. (g) Al Allak, H. M.; Brinkman, A. W.; Richter, H. and Bonnet, D. *J. Cryst. Growth* **1996**, *159***,** 910.

6. http://www.nrel.gov/pv/highperformancepv/pdfs/papers/76.pdf

7. Ramanathan, K; Contreras, M. A.; Perkins, C. L.; Asher, S.; Hasoon, F. S.; Keane, J.; Young, D.; Romero, M.; Metzger, W.; Noufi, R.;Ward, J. and Duda, A. *Prog. Photovolt: Res. Appl.* **2003**, *11*, 225–230

8. (a)Birkmire, R.W.; McCandless, B. E.; Shafarman, W. N. and Varrin R. D. 9th ECPV Solar Energy Conf., Freiberg Germany, **1989**, p134 (b) Mauch, R. H.; Uuckh, M.; Hedstrom, J.; Lincot, D.; Kessler, J.; Klinger, R.; Stolt, L.; Vedel, J. and Schock, H.W. In: 10th ECPV Solar Energy Conf. Lisbon Portugal, **1991**, p1415 (c) Chu, T. L.; Chu, S.S.; Ferekides, C.; Wu, C. Q.; Britt, J. and Wang, C. J. *Appl. Phys.***1991**, 70, 7608 (d) Chang, Y. J.; Munsee, C. L.; Herman, G. S.; Wager, J. F.; Lee, D. H. and Chang, C. H. *Sur. interface Anal.* **2005**, *37*, 398-405 (e) Voss, C.; Subramanian, S. and Chang, C. H. *J. Appl. Phys.* **2004**, *96*, 5819-5823. (f) Gan, F.Y and Shih, I. *J. Vac. Sci. Tehcnol*. **2002**, *20*, 1365-1368. (g) Meth, J. S.; Zane, S. G.; Sharp, K. G. and Agrawal, S. *Thin Solid Films* **2003**, *444*, 227.

9. Hodes, G. "Chemical solution deposition of semiconductor films" Marcel Dekker, Inc **2003**

10. Melo, O.; Hernandez, L.; Angel, O. Z.; Morales, R. L.; Becerril, M., and Vasco, E. *App. Phys. Lett.* **1994**, *65*, 1278

11. Vigil-Galán,O.; Morales-Acevedo, A.; Cruz-Gandarilla, F.; Jiménez-Escamilla, M. G.; Aguilar-Hernández, J.; Contreras-Puente, G.; Sastré- Hernández, J.; Sánchez -Meza, E. and Ramón-Garcia, M. L. *Thin Solid Films* **2007**, *515*, 6085–6088.

12. Khallaf, H.; Oladeji, I. O.; Chai, G. and Chow, L. *Thin Solid Films* **2008**, *516*, 7306–7312.

13. (a)Mitzi, D. B.; Dimitrakopoulos, C. D.; Rosner, J.; Medeiros, D. R.; Xu, Z. and Noyan, C. *Adv. Mater*. **2002**, *14*, 1772. (b) Milliron, D. J.; Mitzi, D. B.; Copel, M. and Murray, C. E. *Chem. Mater.* 2006, *18*, 587–590. (c) Mitzi, D. B.; Copel, M. and Chey, S. J. *Adv. Mater*. **2005**, *17*, 1285.

14. (a)Milliron, D. J.; Mitzi, D. B.; Copel, M. and Murray, C. E. *Chem. Mater.* **2006**, *18*, 587. (b) Mitzi, D. B.; Koshbar, L. L.; Murray, C. E.; Copel, M.; Afzall, A. *Nature* **2004**, *428*, 299-302.

15. Li, G.; Shrotriyai, V.; Huang, J.; Yao, Y.; Moriarty, T.; Emery, K., and Yang, Y. *Nature Mater*. **2005**, *4*, 864-868

16. Kim, J. Y.; Lee, K.; Coates, N. E.; Moses, D.; Nguyen, T. Q.; Dante, M. and Heeger, A.J. *Science* **2007**, *317*, 222

17. Dimitrakopoulos, C. D. and Malenfant, P. R. L. *Adv.Mater*. **2002**, *14*, 99

18. Lin, Y.-Y.;Gundlach, D. J.; Nelson, S. F.; and Jackson, T. N. *IEEE Trans. Electron Devices* **1997,** *44*, 1325.

19. Zhang, J.; Wang, J.; Wang, H. and Yan, D. *Appl. Phys. Lett.* **2004** *84*, 142.

20. Torsi, L.; Dodabalapur, A.; Rothberg, L. J.; Fung, A. W. P. and Katz, H. E. *Phys. Rev. B* **1998,** *57,* 2271.

21. Navigant Consulting Inc., *Energy Savings Potential of Solid State Lightingin General Illumination Applications*, Washington, DC, **2003**. http://lighting.sandia.gov/

22. Nakamura, S. and Fasol, G. *The Blue Laser Diode: GaN Based Light Emitters and Lasers* (Springer, Berlin, 1997).

23. (a) Ellens, A.; Huber, G. and Kummer, F. U. S. Patent No. 6, 657, 379 (2 December 2003) (b) Xie, R. J.; Hirosaki,N.; Sakuma,K.; Yamamoto, Y. and Mitomo, M. *Appl. Phys. Lett*., **2004**, *84,*5404

24. Bowers, M. J.; McBride, J. R. and Rosenthal, S. J. *J. Am. Chem. Soc.* **2005**, *127*, 15378

25. Mueller, A. H.; Petruska, M. A.; Achermann, M.; Werder, D. J.; Akhadov, E. A.; Koleske, D. D.; Hoffbauer, M. A.; Klimov, V. I. *Nano Lett.* **2005**,*5*, 1039.

26. (a) Li, J. and Huang, X.Y. "Nanostructured Crystals: A Unprecedented Class of Size- Independent Semiconductor Nanomaterials with Systematic Structure-Property Tunability", in Handbook of Nanoscience and Technology, Oxford University Press. (b) Mitzi, D. B.; Chondroudis, K. and Kagan, C. R. *IBM J. RES. & DEV.* **2001**, *45*, 29. (c) Mizti, D.B. *J. Mater. Chem*., **2004**, *14*, 2355. (d) Holder, E.; Tessler, N. and Rogach, A. L. *J. Mater. Chem*., **2008**, *18*, 1064. (d) Sanchez, C.; Julián, B.; Belleville, P. and Popall, M. *J. Mater. Chem*., **2005**, *15*, 3559.

27. Huynh, W. U.; Dittmer, J. J. and Alivisatos, A. P *Science* **2002**, 295, 2425.

28. (a)Sun, X.W.; Huang, J. Z.; Wang, J.X. and Xu,Z. *Nano Lett.* **2008**, *8*, 1219. (b)Yang, H. and Holloway, P.H. *J.Phys.Chem*. B. **2003**, *107*, 9705 (c) Gao, M.; Richter, B.; Kirstein, S. and Möhwald, H. *J. Phys.Chem. B*. **1998**, *102*, 4096

29. Coe, S.; Woo, W.; Bawendi, M. and Bulovic, V. *Nature* **2002,** 420, 800-803

30. (a)Huang, X.-Y.; Li, J.; Fu, H. *J. Am. Chem. Soc.* **2000**, *122*, 8789. (b) Huang,X.; Li, J.; Zhang, Y.; Mascarenhas, A. *J. Am. Chem. Soc*. **2003,** *125*, 7049-7055. (c) Huang, X.Y.; Heulings IV, H. R.; Le, V.; Li, J. *Chem. Mater*. **2001**, *13*, 3754. (d) Heulings IV, H. R.; Huang, X.-Y.; Li, J.; Yuen, T.; Lin, C. L. *Nano Lett.*, **2001**, *10*, 521. (e) Huang, X.-Y.; Li, J. Mater. Res. Soc. Symp. Proc., **2002**, *728*, 17-22. (f) Huang, X.-Y.; Heulings IV, H. R.; Li, J.; Yuen, T.; Lin, C. L., *J. Nanosci. & Nanotech*., **2005**, *5*, 1487. (g) Fluegel, B.; Zhang, Y.; Mascarenhas, A.; Huang, X.-Y.; Li, J. *Phys. Rev. B*, *Phys*. *Rev*. *B,* **2004**, *70(20)*, 205308/1-205308/5. (h) Zhang, Y.; Dalpian, G. M.; Fluegel, B., Wei, S.-H.; Mascarenhas, A.; Huang, X.-Y.; Li, J.; Wang, L.-W. *Phys. Rev. Lett*., **2006**, *96*, 026405. (i) Moon, C.-Y.; Dalpian, G. M.; Zhang, Y.; Wei, S. -H.; Huang, X. -Y.; Li, J. *Chem. Mater.*, **2006**, *18*, 2805. (j) Huang, X. and Li, J. *J. Am. Chem. Soc.* **2007**, *129*, 3157-3162.

31. (a) Li, J.; Bi, W.; Ki, W.; Huang, X. and Reddy, S. *J. Am. Chem. Soc.* **2007**, *129*, 14140-14141. (b) Zhang, Y.; Islam, Z.; Ren, Y.; Parilla, P. A.; Ahrenkiel, S. P.; Lee, P. L.; Mascarenhas, A.; McNevin, M. J.; Naumov, I.; Fu, H.-X.; Huang, X.-Y.; and Li, J. *Phys. Rev. Lett.* **2007**, *99***,** 215901.

32. Laudise, R.A. *C&EN* **1987**, September 28, 30-43.

33. (a) Yuan, H. M.; Zhu, G. S.; Chen, J. S.; Chen, W.; Yang, G. D. and Xu, R. R. *J. Solid State Chem*. **2000***,151,*145. *(b)* Forste, P. M. and Cheetham, A. K. *Topics in Catalysis* **2003***, 24,*79. *(c)* Bauer, S. and Stock, N. *Angew. Chem.* **2007***, 119,* 6981.

34. Ki, W. and Li, J. *J. Am. Chem. Soc*. **2008,** *130*, 8114-8115.

35. Kagan, C. R.; Mitzi, D. B. and Dimitrakopoulos, C. D. *Science* **1999**, *286*, 945.

CHAPTER TWO

Group VI-VI Transition Metal Chalcogenide Thin Film Fabrication by Solution Based Deposition

2.1 Introduction

Layered transition metal chalcogenides (MQ_2, M=Mo, W; Q = S, Se, Te) have received great interest because of their highly anisotropic mechanical and electrical properties. These arise from their layered "sandwich-like" structure, where a hexagonal sheet of metal atoms is covalently bonded to two hexagonal sheets of chalcogen atoms from above and below and the so formed MQ_2 layers are held by weak van der Waals bonds. These materials have been used for applications such as lubricants and catalysis.[1]

Layered transition metal chalcogenide semiconductors have also been explored for photovoltaic energy conversion, because these compounds exhibit promising characteristics for the application in thin film solar cells. For instance, they have high adsorption coefficients (up to 3×10^5 cm^{-1}) with energy gaps of 1.2 to 1.7 eV.[2] Single crystal of WSe_2 showed energy conversion efficiencies of 17% in wet iodine-iodine solar cells.[3] In addition, the weak van deer Waals bonds between layers might provide the possibility to reduce the extent of high lattice mismatch in hetero-junction n-GaAs/$MoSe_2$ solar cells without interface states.[4] Layered transition metal chalcogenides also exhibit considerably high chemical stability due to the lack of dangling bonds.[5]

While it has been shown that micro- or nano structures of MoS_2 and WS_2 can be obtained from thermal decompositions stemming from ammonium thiosalts at various temperatures,[6] very little has been reported on solution based deposition of Group-VI metal dichalcogenides.[7] Most thin film fabrication methods mentioned above require high vacuum systems or temperatures.

Clearly, there is a great need to develop simple and low-cost solution based techniques to fabricate thin films of these semiconductors for applications in

photovoltaics. We reported thin film fabrication of MS_2 (M=Mo,W) semiconductors by simple and cost effective solution processed deposition via spin coating techniques.[8]

2.2 Experimental

2.2.1 Precursor synthesis for MoS_2 thin film fabrications

1.5mmol of $(NH_4)_2MoS_4$ was dissolved in methylamine. A dark red clear solution was obtained by constant stirring in an argon atmosphere at room temperature. This solution was then dried in a vacuum oven overnight. Dark red crystals were formed and their structure was solved by single crystal X-ray diffraction analysis. The molecular crystal structure, $(CH_3NH_3)_2MoS_4$, is shown in Figure 2.1

2.2.2 Procedures to synthesize MoS_2thin film fabrication

The molecular crystals 0.1687g $(CH_3NH_3)_2MoS_4$ were dissolved in 1mL ethylene glycol (99.9%), deposited by spin coating with a 3500rpm for 60sec onto SiO_2/Si substrate (d_{sio2}=4000A), and then dried at 70^oC for a few seconds on a hot plate in air. This spin coating sequence was repeated 5 times to make uniform and continuous films.

After two steps of calcinations: 200^oC for 1h and 600^oC for 2 h under N_2 atmosphere, the MoS_2 films were formed. Drop casting on clean glass was used to characterize structural and optical absorption by PXRD and UV-vis spectroscopy. The glass films show homogeneous metallic luster and a deep brown color.

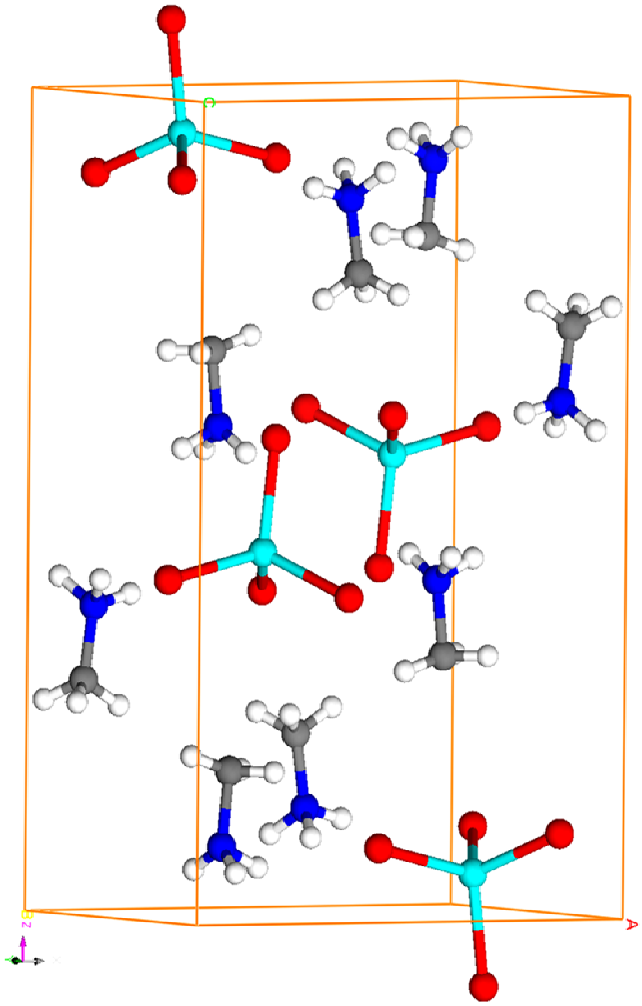

Figure 2.1 Molecular crystal structure of $(CH_3NH_3)_2MoS_4$: Orthorhombic (Pnma): a = 9.636(2) Å, b = 6.9820(10) Å, c = 15.763(3) Å, V =1060.5(3) $Å^3$, and Z= 4

2.2.3 Precursor synthesis for WS_2 thin film fabrications

A clear yellow-orange solution was obtained by dissolving 1.4mmol ammonium tetrathiotungstate ($(NH_4)_2WS_4$) into 1mL methylamine with stirring in argon atmosphere at room temperature. After the solution was dried in a vacuum oven overnight, yellow crystals were produced. Single X-ray diffraction showed that the crystal structure of $(CH_3NH_3)_2WS_4$ is isostructural with $(CH_3NH_3)_2MoS_4$. The crystal structure of $(CH_3NH_3)_2WS_4$ is orthorhombic (Pnma): a = 9.692Å b = 7.040Å c =15.745 Å, V =1074.31$Å^3$, and Z= 4.

2.2.4 Procedures to synthesize WS_2thin film fabrication

0.2520g $(CH_3NH_3)_2WS_4$ were dissolved in 0.8ml hydrazine, deposited by spin coater with 3500rpm for 60sec onto SiO_2/Si substrate (d_{sio2}=4000Å), and dried at 60^oC for several seconds on a hot plate in air. After two steps of calcinations, at 200^oC for 1hour, and 600^oC for 2 h under H_2/Ar atmosphere, the WS_2 thin films were formed.

Again, for structural and optical spectra, drop casting onto clean glass were used.

2.3 Results and Discussion

2.3.1 MoS_2 thin films

The molecular crystal structure of $(CH_3NH_3)_2MoS_4$ is shown in Figure 2.1. The solubility of the $(CH_3NH_3)_2MoS_4$ crystals was significantly improved compared with that of $(NH_4)_2MoS_4$ in ethylene glycol. In addition, the films prepared from precursor $(CH_3NH_3)_2MoS_4$ showed higher crystallinity compared with films prepared from $(NH_4)_2MoS_4$. Thermal decomposition of $(CH_3NH_3)_2MoS_4$ was performed from room temperature to ~600^oC by a thermogravimetric analysis (TGA) under N_2 atmosphere. As seen in Figure 2.2, the final product was identified as MoS_2, resulting in 44.4% weight loss which is in excellent agreement with the calculated weight loss of 44.5% from $(CH_3NH_3)_2MoS_4$ to MoS_2. Clearly, films calcined at 600^oC are both highly crystalline and exhibit a highly preferred orientation corresponding to the (00ℓ) plane in 2H-MoS_2 (ICDD 37-1492). Figure 2.3(a) shows the PXRD patterns of the thin film samples calcinated at 450 (i) and 600 ^oC (ii), respectively. The shift of the first peak to lower angle (~0.2Å) was also observed by Pütz *et al*.[7]

At low temperature, 450^oC, it appeared that amorphous MoS_2 was formed. It has been observed that the evolution from ammonium tetrathiomolybdate by thermal decomposition is the following sequences.[9] $(NH_4)_2MoS_4 \rightarrow MoS_3 \rightarrow MoS_2$ (amorphous) $\rightarrow MoS_2$ (crystalline).

MoS_3 is formed, releasing ammonia and H_2S gas in the temperature 200^oC-300^oC. Between 350^oC and 400^oC, poor crystalline MoS_2 is formed by eliminating sulfur or H_2S. Finally crystalline MoS_2 is formed above 500^oC. In our case, amorphous MoS_2 is formed

from $(CH_3NH_3)_2MoS_4$ at 450°C and crystalline MoS_2 is formed above 600°C which is analogues to the sequence for $(NH_4)_2MoS_4$.

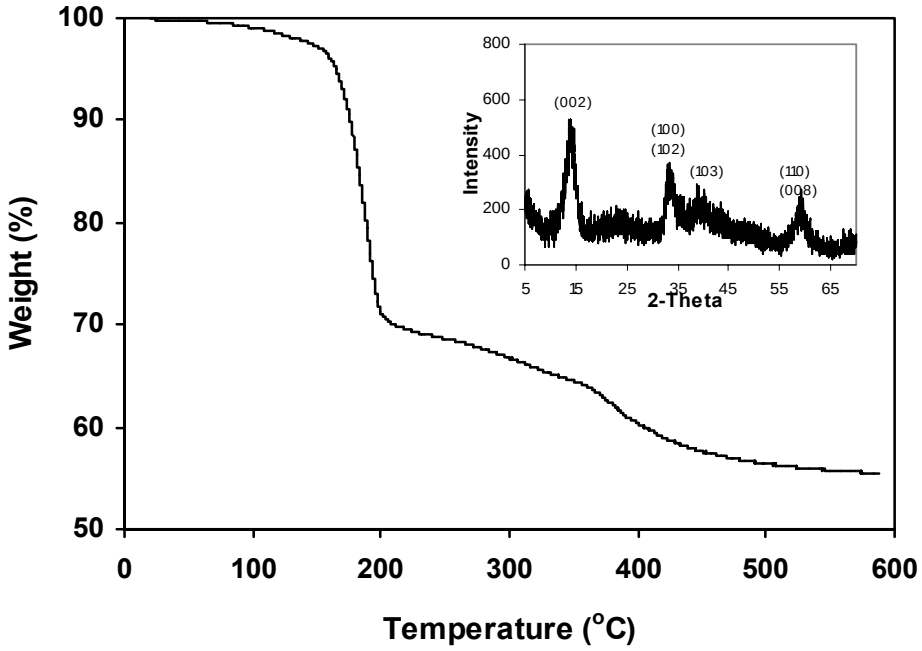

Figure 2.2 Thermogravimetric analysis of $(CH_3NH_3)_2MoS_4$ (ramp rate: 5°C/min). (Inset: The powder X-ray diffraction pattern after thermal decomposition of the precursor at ~600°C)

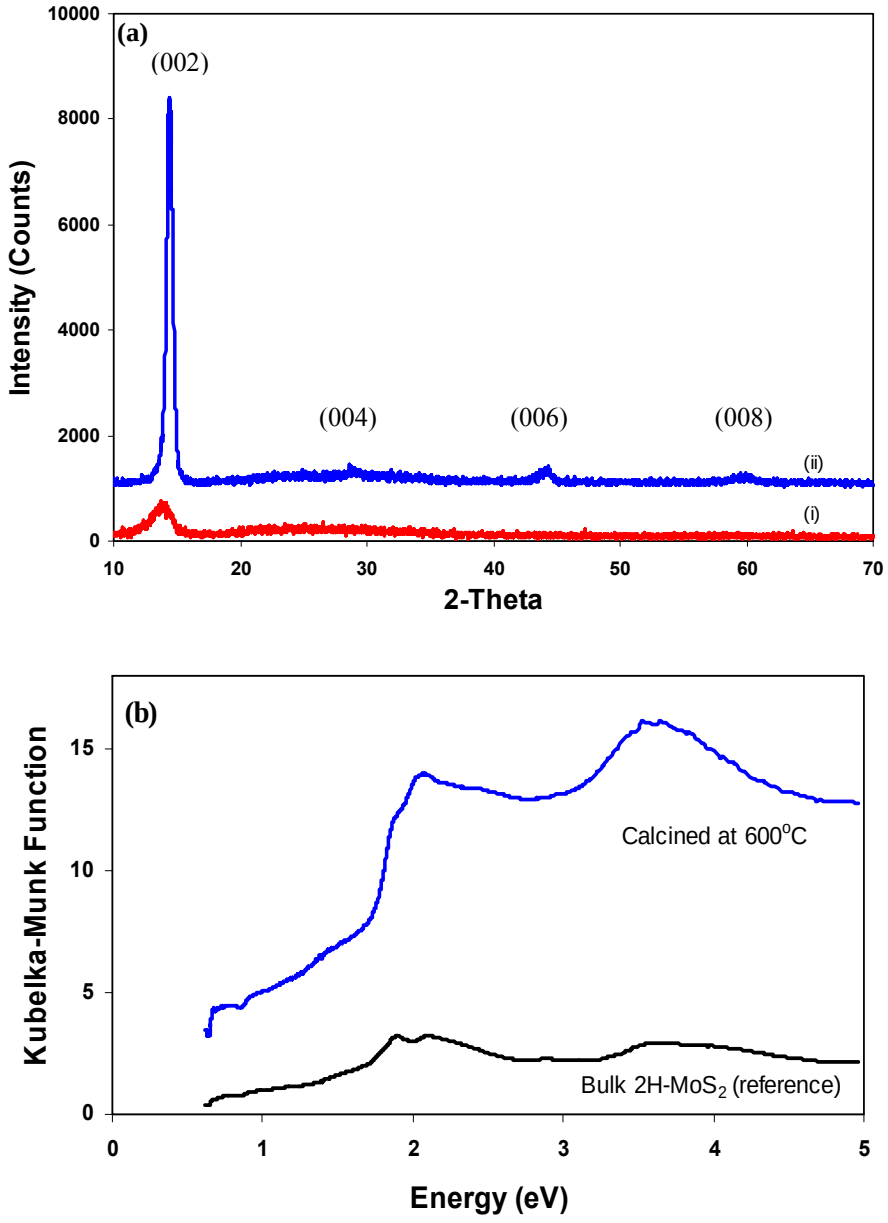

Figure 2.3 (a) Powder X-ray diffraction patterns of the MoS_2 films deposited onto glass slides compared with that of the ICDD database. (i) 450 ^oC and (ii) 600 ^oC. (b) Optical absorption spectra of the 2H-MoS_2 taken between 250nm to 2000nm.

Optical absorption spectra were measured by diffuse reflectance experiments. From the optical absorption edge band gap was estimated to be ~1.57eV (Fig.2.3(b)), which is consistent with that reported for 2H-MoS_2 nanoparticles (E_g = 1.74eV, ~10 nm).[10] Energy dispersed X-ray spectroscopy is a technique used for identifying the elemental composition of the specimen, or interest area. It has found both Mo and S exist in this film and oxygen and silicon peaks are from the silicon dioxide substrate.

Surface morphology of the films was analyzed by an atomic force microscope (AFM) with tapping mode as shown in Figure 2.4. Film morphology is highly dependent on the choice of solvents, as well as the spin coating procedure. Depending on the solvent used and spin coating sequence dramatically different grain morphology and surface coverage may result. For example, when hydrazine, a strong reducing agent, was used as the solvent, micro-sized grains and holes were created in the MoS_2 films with the multi-step spin coating. In addition, films were discontinuous and inhomogeneous. As a result, differential resistance of MoS_2 film was quite high (~1.6MΩ) due to the influence of grain boundaries compared to that of MoS_2 film using ethylene glycol (~1KΩ).

As seen in Figure 2.4, when single spin coating techniques was employed using ethylene glycol solvent, spherical grains with an average size of ~300nm as evaluated by "ImageJ" software,[11] while multi-step process yielded a more continuous and well-connected film with significantly larger particle sizes (average size: ~1.2μm). Clearly, thin plate-shaped crystals have a preferential orientation of (00ℓ), as seen in Figure 2.4(b).

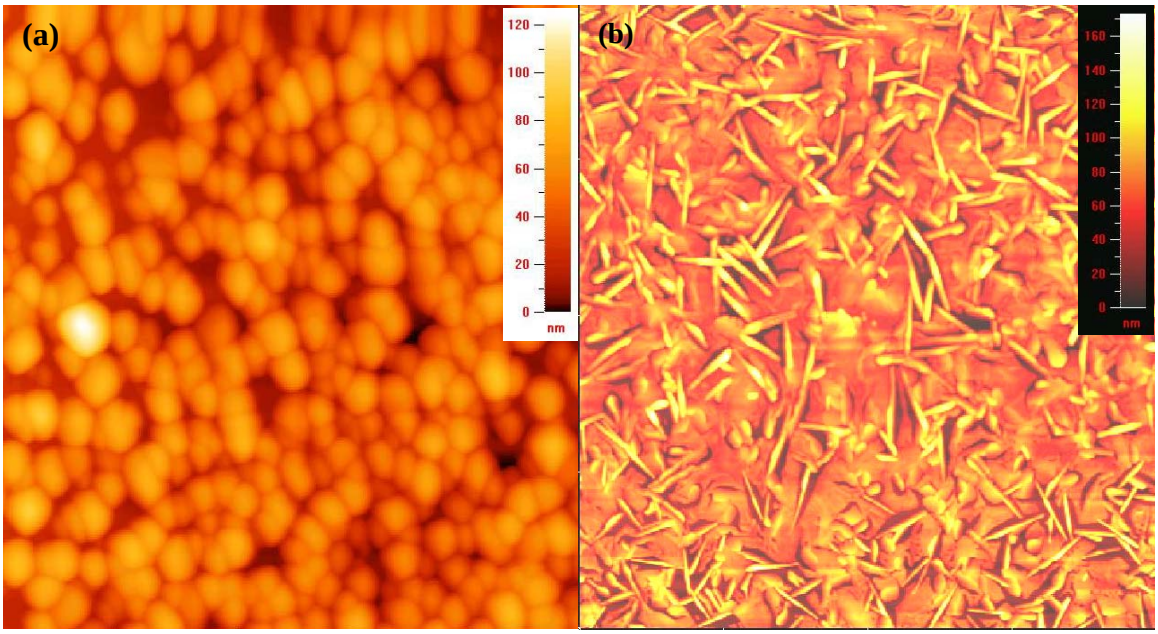

Figure 2.4 Topological images of the MoS_2 thin film by AFM with tapping mode: (a) single step spin casting with 5μm× 5μm scan. The average film thickness is ~45nm by AFM, (b) multi-step spin casting with 20μm × 20μm scan, the thickness was ~70nm, as evaluated by cross section by SEM (see Fig. 2.5(b)).

Current–voltage curve of the MoS_2 thin film deposited with multi-step is shown in Figure 2.5(a). Evaporated aluminum was used for the electrodes in order to have ohmic contact. Distance between two contacts was 150μm. Current-voltage characteristic shows ohmic behavior and differential resistance is 294 Ω at room temperature similar to sheet resistance of 676Ω from four point probe method.

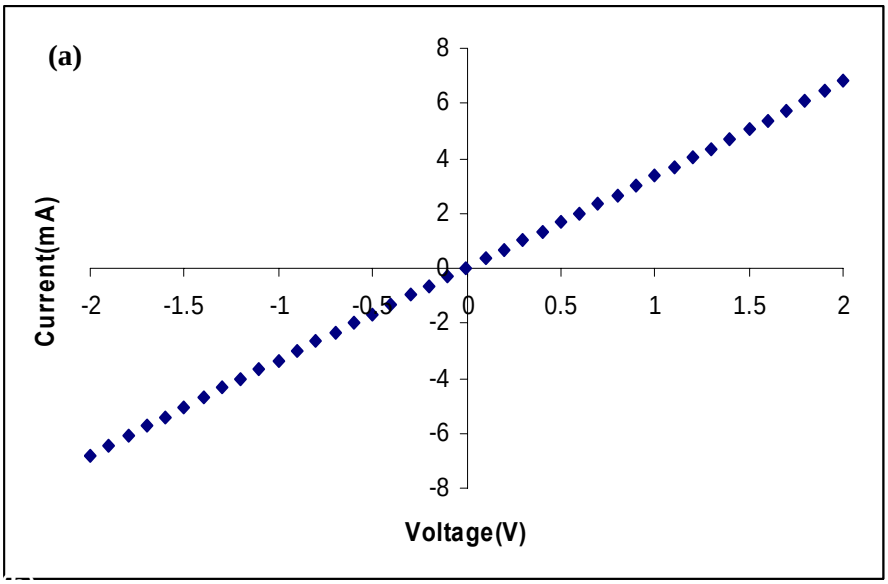

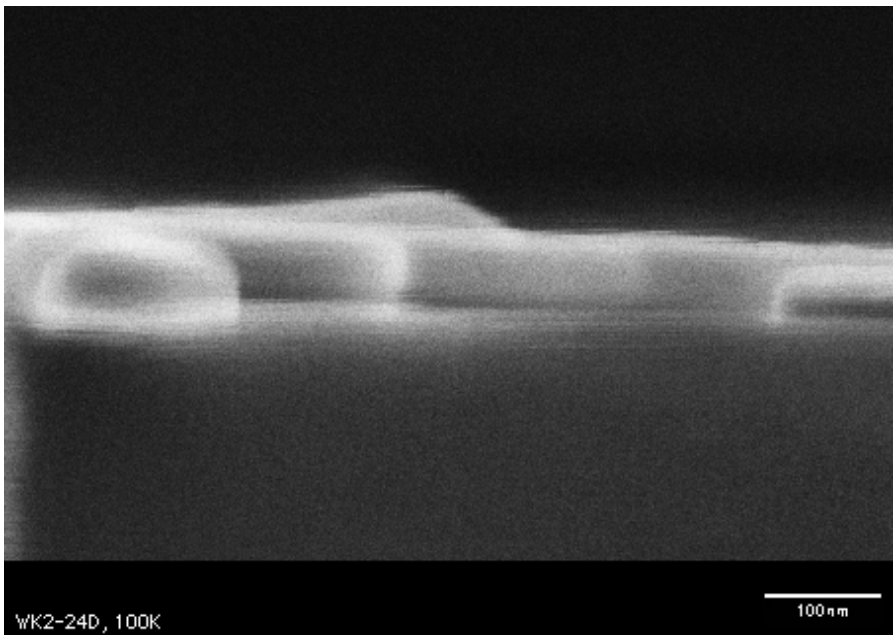

Figure 2.5 (a) Current–voltage curve of the MoS_2 thin film, (b) Cross-sectional SEM image of the MoS_2 thin film by multi-step spin coating(scale bar:100nm)

The conductivity measurements were also carried out using the dc four-point probe method in the temperature range of 25K–300K. The electrical contacts to the film surface were made through a pair of silver paint electrodes. The conductivity of the films was calculated from sheet resistance with the film thickness of ~100nm as shown in Figure 2.5(b).

The electrical conductivity of the film was ~50($\Omega^{-1}\cdot cm^{-1}$), a substantially higher value than the previously reported values.[12] Interestingly, the conductivity of the films increases with an increase in temperature, indicating metallic nature of the film as seen in Figure 2.6. The metallic nature and high conductivity of these films would be attributed to high electron concentration (~2×10^{20} cm^{-3}) which is higher than that of a typical single crystal ($10^{16\sim}10^{17}$ cm^{-3}).[13] Another possible explanation is that the conduction mechanism of polycrystalline film is dominated by the inherent intercrystalline, rather than the intracrystalline characteristics.

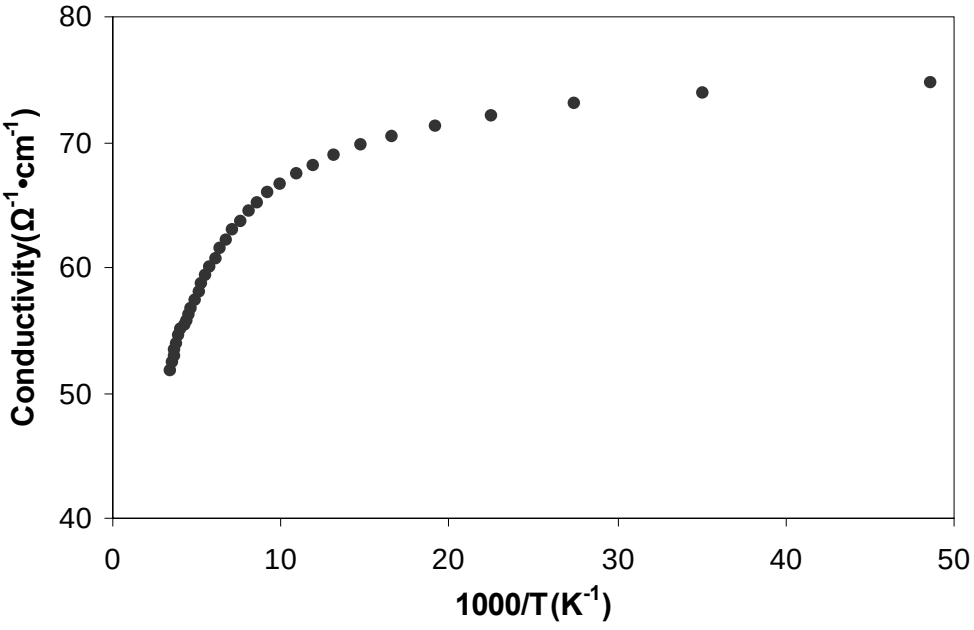

Figure 2.6 The electrical conductivity of the film as a function of temperature.

Grain boundaries provide a potential barrier to the passing of free charges, thus reducing mobility and conductivity as well as the grain size which affects the conduction mechanism.[14] As seen in the surface topology of the films, shown in Figure 2.4(a), single-step spin coating resulted in small grain size and high grain boundaries, and consequently, higher resistivity. On the other hand, the films processed by a multi-step spin coating sequence show much less grain boundaries and are much better connected. As a consequence, their resistivity is significantly lowered.[15]

The Hall mobility was found of be ~2 $cm^2/V{\cdot}s$ which is small value due to impurity scattering from the high electron concentration. Table 2.1 shows transport data on the films from the Hall effect measurement.[8] The uncertainty in the values is about 10%. While the MoS_2 film exhibits a higher conductivity, the carrier mobility is relatively low. Low mobility of the films could be explained by impurity scattering.[16] As shown in Fig. 2.3(a), lattice distortion occurred at every peak position. Based on the lattice expansion equation $\varepsilon=\Delta d/d_o$ (d_o is the d-spacing of the original lattice; Δd is the change in the d-spacing; ε is the lattice expansion),[17] the lattice expansion of the (002) plane of the MoS_2 was calculated to be 1.5% at 600 °C and 3.2% at 450 °C. For the MoS_2 films, this lattice distortion may arise from carbon impurities, as previously reported.[7]

Table 2.1 Transport data measured on MoS_2 and WS_2 thin films

	Mobility(cm^2/Vs)	Carrier concentration(cm^{-3})
WS_2	< 1	n-type
MoS_2	2	n-type 2×10^{20}

2.3.2 WS_2 thin film fabrication

The crystal structure of $(CH_3NH_3)_2WS_4$ is isostructural to that of $(CH_3NH_3)_2MoS_4$ as shown in Figure 2.7

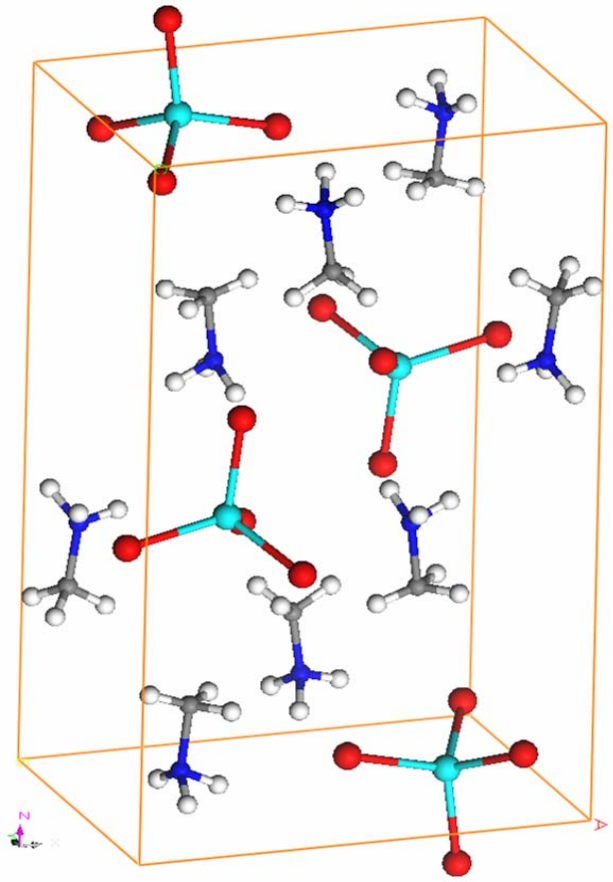

Figure 2.7 Crystal structure of $(CH_3NH_3)_2WS_4$: Orthorhombic (Pnma): a = 9.692Å, b = 7.040Å, c =15.745 Å, V =1074.31Å^3, and Z= 4.

.

Its thermal decomposition properties were also analyzed by TGA under inert nitrogen atmosphere. The final product at 600^{o}C was a mixture of WS_2 and WO_3, because WO_3 is more stable than WS_2 based on their free enthalphy data.[18] To avoid WO_3, the

WS_2 films were formed under a flow of hydrogen/argon at 600 ^oC.

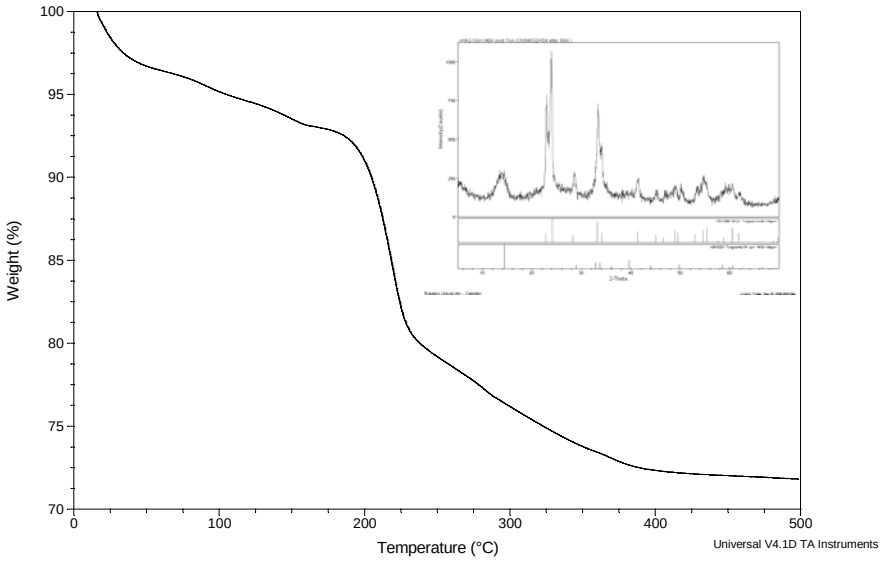

Figure 2.8 Thermogravimetric analysis of $(CH_3NH_3)_2WS_4$ (ramp rate: 5^oC/min). (Inset: The powder X-ray diffraction pattern after thermal decomposition of the precursor at ~600^oC.

The PXRD pattern of a typical WS_2 thin film in comparison with that of 2H-WS_2 bulk (ICDD 08-0237) is shown in Figure 2.9. In general, the peaks are broad, possibly due to the relative poor crystallinity. It has been reported that highly crystalline WS_2 may be achieved by thermal decomposition of ammonium tetrathiotungstate at very high temperatures (over 1000 ^oC).[19] The first diffraction peak is also shifted slightly to a low angle as in the case of MoS_2. Optical band gap of WS_2 film was consistent with the reported value of 1.3 eV, but very low adsorption peak was found.[20]

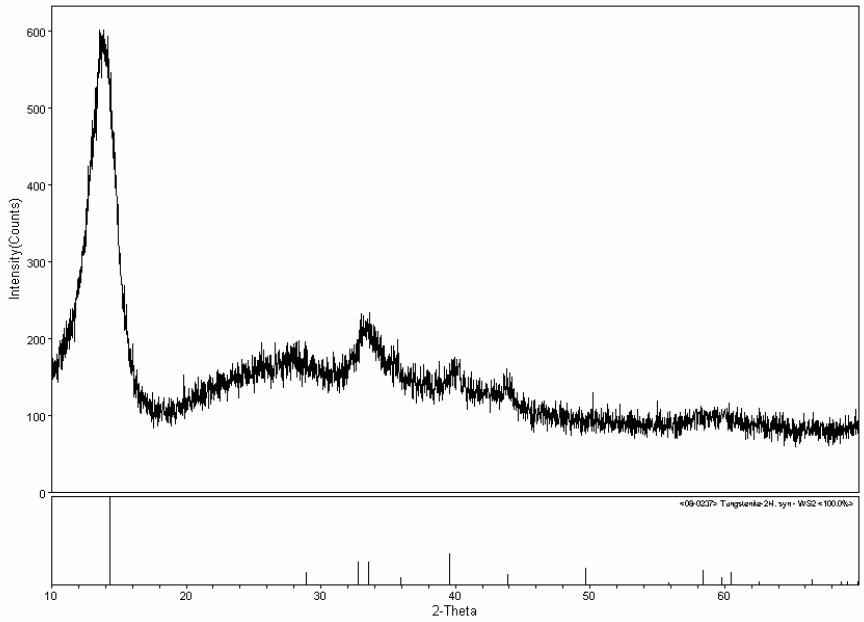

Figure 2.9 Powder X-ray patterns of the WS_2 thin film spun onto a glass after annealing at 600^{o}C under H_2/Ar

The AFM image of a WS_2 thin film is shown in Figure 2.10(a). Uniform and continuous films were obtained by a single step spin coating procedure because multistep spin coating did not lead to uniform surface of WS_2 films as for MoS_2. Thus, surface morphology is again shown to be strongly case dependent. The average thickness of the film was ~50nm as shown in Figure 2.10(b)

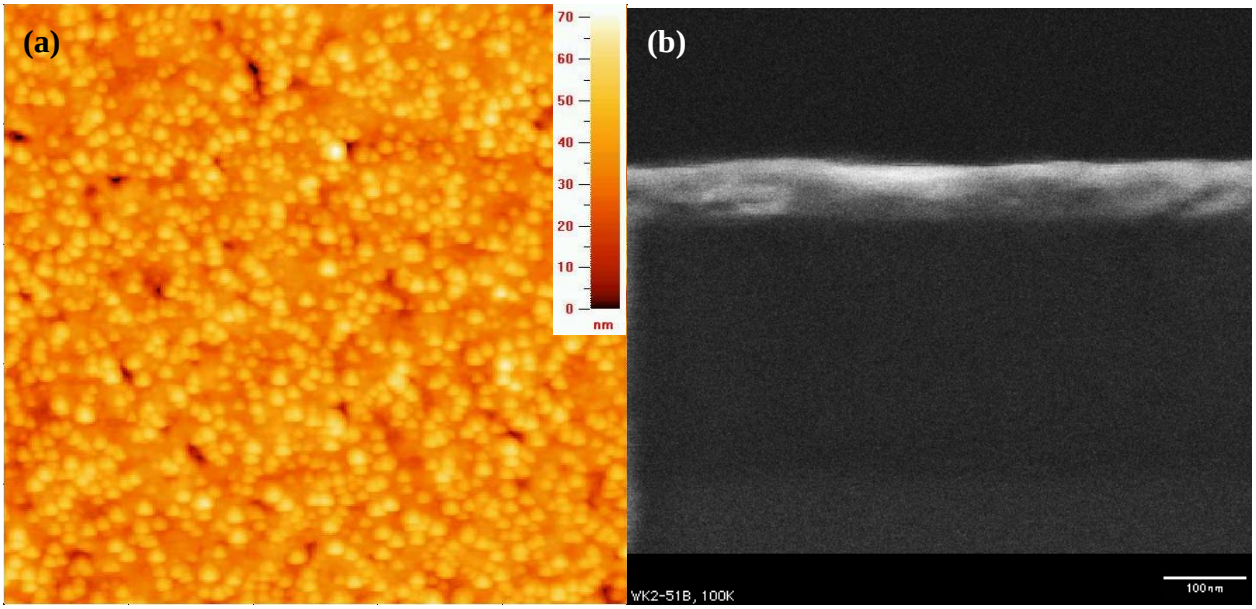

Figure 2.10 (a) AFM image of the WS_2 thin film by single-step spin casting (size of the image: 5μm x 5μm). The average size of the grain is ~ 100nm, (b) the cross sectional SEM image of the WS_2 thin film by single step spin coating (scale bar: 100nm). Thickness of the films is ~50nm.

Temperature dependence of the electrical resistivity was measured and plotted in Figure 2.11. The p-type WS_2 films show a typical semiconductor behavior. The conductivity of this film is found to be ~6 ($\Omega^{-1}\cdot cm^{-1}$) at room temperature, which is higher than that of WS_2 films synthesized by other techniques.[21] AFM image and cross section of the WS_2 film are shown in Figure 2.10(b). From the figure, one sees uniform and continuous films were created by single step spin coating. Because of low carrier mobility, the Hall measurement on WS_2 films has some uncertainty, but the thermal probe does indicate the films are *n*-type.

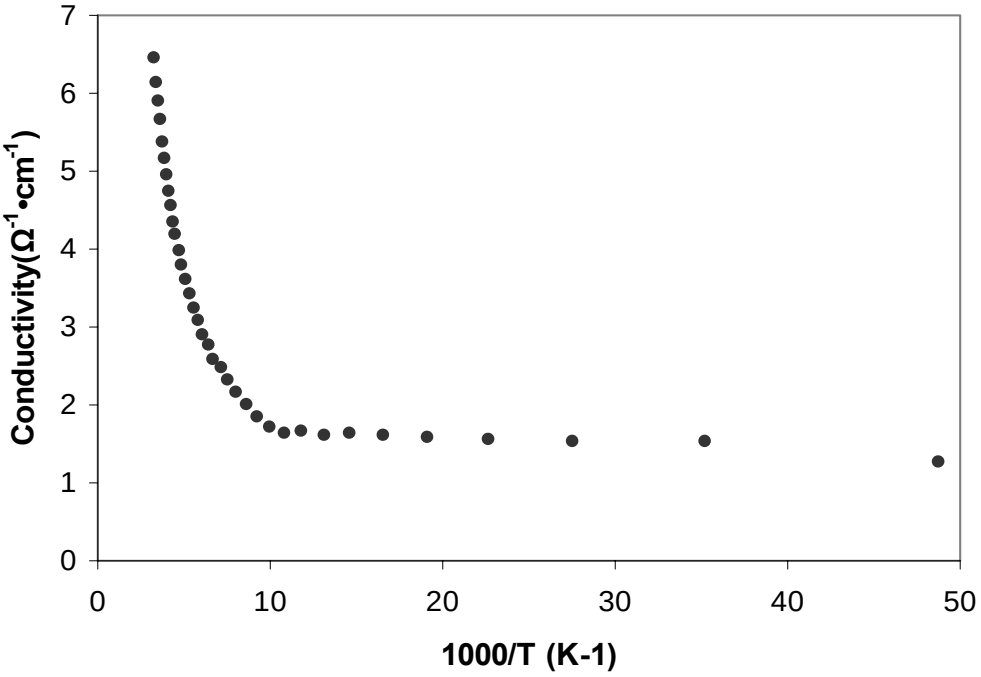

Figure 2.11 Temperature dependence of electrical conductivity of the WS_2 film

2.4. Conclusions

We have developed a simple, efficient, and low-cost solution-based deposition technique to fabricate MoS_2 and WS_2 thin films by using soluble precursors via the spin-coating technique. Surface morphology, in terms of grain size and continuity of the films, was directly influenced by the choice of organic solvents used to dissolve the precursors, as well as spin-coating sequences. Morphological changes affected the conductivity of the films. Highly conductive and textured *n*-type MoS_2 thin films were achieved by multi-step spin casting using ethylene glycol as the solvent. The *n*-type WS_2 thin films were fabricated using soluble precursors via single-step spin coating.

2.5 References

1. (a) Rapoport, L.; Bilik, Y.; Feldman, Y.; Homyonfer, M.; Cohen, S. R.; Tenne, R. *Nature* **1997,** *387*, 791-793. (b) Hinnemann, B.; Moses, P. G.; Bonde, J.; Jørgensen, K. P.; Nielsen, J. H.; Horch, S.; Chorkendorff, I. and Nørskov, J. K. *J. Am. Chem. Soc.* **2005,** *127*, 5308-5309.

2. Moehl, T. and Tributsch, H. Annual Report, Hahn-Meitner-Institut. SE5

3. Srivastava, O.N. and Prasad, G. *J. Phys. D: Appl. Phys*. **1988,** *21*, 1028-1030.

4. Ueno, K.; Shimada, T.; Saiki, K. and Koma, A. *Appl. Phys. Lett.* **1990,** *56*, 327.

5. Frey, G. L.; Reynolds, K. J. and Friend, R. H. *Adv. Mater*. **2002**, *14*, 265

6. (a) Afanasiev, P. and Bezverkhy, I. *Chem. Mater.* **2002,** *14*, 2826, (b) Zelenski, C. M. and Dorhout, P. K. *J. Am. Chem. Soc*. **1998,** *120*, 734. (c) Alonso, G.; Valle, M.; Cruz, J.; Licea-Claverie, A.; Petranovskii, V. and Fuentes, S. *Catal. Lett***. 1998**, *52*, 55-61.

7. Pütz, J. and Aegerter, M. A. *Thin solid Films* **1999**, *351*, 119-124.

8. Ki, W.; Huang, X.; Li, J.; Young, D.L. and Zhang, Y. *J. Mater. Res.* **2007**, *22*, 1390.

9. Alonso, G.; Valle, M.; Cruz, J.; Licea-Claverie, A.; Petranovskii, V. and Fuentes, S. *Catal. Lett***. 1998**, *52*, 55-61.

10. Roy, P. and Srivastava, S. K. *Thin solid Films* **2006,** *496*, 293 – 298.

11. http://rsbweb.nih.gov/ij/

12. (a) Cheon, J.; Gozum, J. E. and Girolami, G. S. *Chem. Mater*. **1997,** *9*, 1847-1853. (b) N. Barreau and J. C. Bernède, *J.Phys.D:Appl.Phys*., **2002,** *35*, 1197. (c) Bernède, J. C.; Pouzet, J.; Gourmelon, E. and Hadouda, H. *Synth. Met***. 1999,** *99*, 45-52. (d) Mandal, K. C. and Mondal, A. *J. Solid State Chem.* **1990**, *85*, 176-179.

13. Wilson, J. A. and Yoffe, A. D. *Adv. Phys.* **1969,** *18*, 193-335.

14. Seto, J. Y. W. *J. Appl. Phys*. **1975,** *46*, 5247-5254.

15. The resistivity of the films by single-step spin coating was found to be ~7Ω·cm by four point probe method at RT. However, the resistivity of the films by multi-step spin coating was found to be ~ 0.02Ω·cm.

16. Sze, S.M. Semiconductor devices: Physics and Technology, 2nd ed.(John Wilely

& Sons, NY,1985)

17. Mergel, D. and Qiao, Z. *J. Appl. Phys*. **2004**, *95*, 5608.

18. Ouerfelli, J.; Bernède, J. C.; Khelil, A. and Pouzet, J. *Appl. Surf. Sci*. **1997**, *120*, 1-8.

19. Walton, R. I. and Hibble, S. J. *J. Mater. Chem.* **1999**, *9*, 1347.

20. Bucher, E. and Aruchamy, A. Photoelectrochemisty and photovoltaics of Layered Semiconducors (Kluwer Academic Phublishers, Dordrecht, NL, 1992) p.36

21. (a) Jäger-Waldau, A.; Lux-Steiner, M. Ch.; Jäger-Waldau, G., and Bucher, E. *Appl. Surf. Sci.* **1993**, *71*, 731. (b) Li, S. J.; Pouzet, P. and Jamali, J. *J. Phys. Condens. Matter* **1996**, *8*, 2291. (c) Elimer, K.; Stock, C.; Diesner, K., and Sieber, I. *J. Cryst. Growth* **1997**, *182*, 389.

CHAPTER THREE

Cadmium Sulfide Thin Film Fabrication by Solution Based Deposition

3.1 Introduction

Heterojunction solar cells with a narrow band-gap base have been studied in an attempt to develop efficient, stable, and low cost solar cells. Both $CuInSe_2$ and CdTe are being intensively studied for photovoltaic applications because both have a direct band gap of ~1.45eV, which is nearly optimum for solar energy conversion, and both possess high absorption coefficient.[1] . At the same time, cadmium sulfide (CdS) has been found to be a good candidate as window material for heterojuction thin films solar cells.[2] CdTe/CdS heterojunction solar cells exhibit the highest conversion efficiency (~16.5%) so far.[3] In addition, due to its high mobility and thermal stability, it has been exploited for applications in thin film field effect transistors (TFTs).[4-7] CdS thin films have been developed by various techniques, such as sputtering,[8] pulsed laser deposition,[9] chemical bath deposition,[10]electrodeposition[11] screen printing,[12]and chemical vapor deposition.[13] .

Solution processed deposition technique, suitable for flexible substrates, and with the advantages of low-cost and capable for large-area fabrication of thin films, have been extensively developed by methods such as printing and chemical bath deposition (CBD). In most case, CdS films were obtained by CBD. This method, however, shows relatively poor electrical properties, such as resistivity and mobility, because of surface scattering from grain boundaries or impurities. Additionally, characteristics of thin films are also strongly dependent on preparation conditions such as temperature, stirring, and concentration of precursors.

Anther interesting application using solution based deposition is dye sensitized solar cells (DSSC). DSSC consists of TiO_2 nanoparticles acting as an electron acceptor layer and a light absorber, such as dye molecules and nanosized semiconductors to

enhance energy conversions. Considerable effort has been made to fabricate DSSCs with enhanced energy conversion efficiency, low cost, and longer time stability.[14-15] Nano-size semiconductors have great advantages over organic dye sensitization to harvest more of the solar flux, because they exhibit quantum confinement effects useful for band-gap adjustment as well as an improved charge separation by inter-particle electron transfer.[16] Recently DSSCs using the CBD method has been reported to create nano-sized CdS and CdSe semiconductor.[17-18]

In this study, we report a new synthetic route for processing CdS thin films that exhibit very high mobility and very low resistivity. This process makes use of spin casting techniques by using a soluble precursor in a conventional solvent. In addition, by manipulating spin coating sequences, surface's microstructures were significantly changed and affected electrical properties.

We also studied the possibilities for photovoltaic application using soluble precursors of CdS into porous TiO_2 cells.

3.2 Experimental

3.2.1 CdS thin film synthesis

Cadmium nitrate ($Cd(NO_3)_2 \cdot 4H_2O$, 99.999%, 1 mmol) and thiourea ($(H_2N)_2CS$, 99%, 1 mmol) were used as cadmium and sulfur sources, respectively. The clear solution was obtained by dissolving the two precursors into 1 mL of dimethyl sulfoxide (DMSO, 99.9%) with stirring in an inert atmosphere. The clear solution was then deposited onto SiO_2/Si by spin coating at 5000rpm for 60s in air. After deposition, films were dried at 40 ^oC for a few seconds on a hot plate in air. This whole procedures were repeated multiple times to produce films with continuous and more complete coverage. The films were dried at 240 ^oC for 2h in a vacuum oven, followed by annealing at 400^oC for 2h and 500^oC for 4h under nitrogen (99.999%) atmosphere.

3.2.2 CdS sensitized porous TiO_2 solar cells using soluble precursors

A clear solution containing Cd and S source was deposited into porous TiO_2 structure with different molar concentrations of the metals ranging from 0.1mmol to 1mmol into 1mL DMSO. The substrates were then annealed in a vacuum oven with different temperatures, 200^oC and 400^oC.

3.3 Results and Discussion

Powder X-ray diffraction patterns and optical absorption spectra are shown in Figure 3.1. Diffraction patterns represent a zinc blend structure of CdS annealed at 400°C (ICDD10-0454) and wurzite structure of CdS annealed at 500°C (ICDD41-1049).

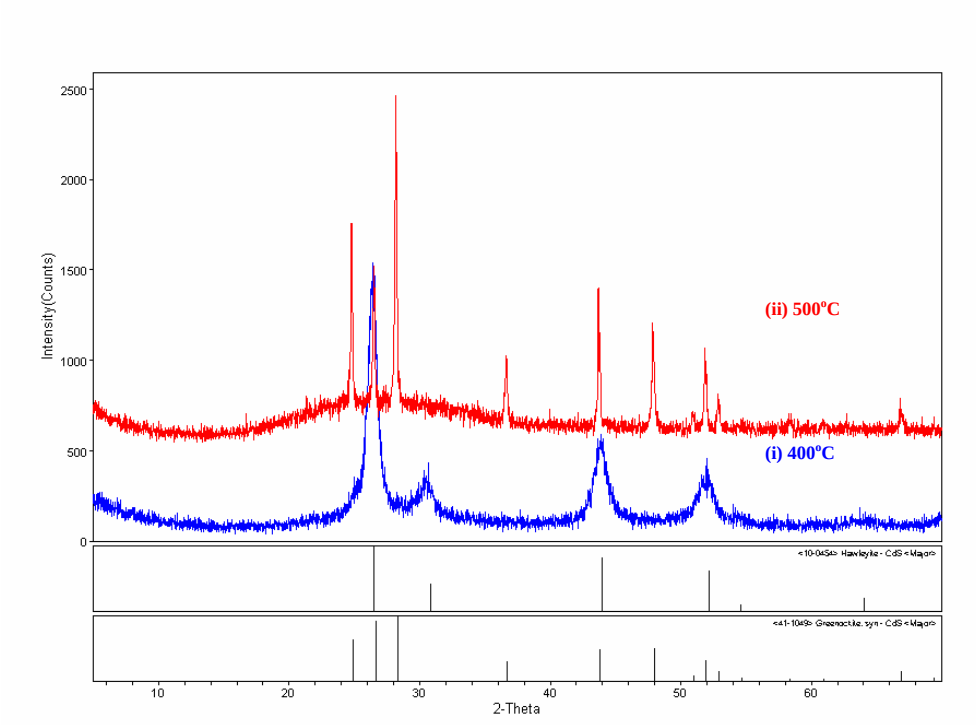

Figure 3.1 Powder X-ray diffraction patterns of the CdS films deposited onto glass slides compared with that of the ICDD database

The structural transition has been reported elsewhere.[19-20] In general, high temperature favors for the formation of the hexagonal phase of the CdS. Estimated energy band gap of both structures is found to be ~2.3 eV, which is consistent with a reported value.[21]

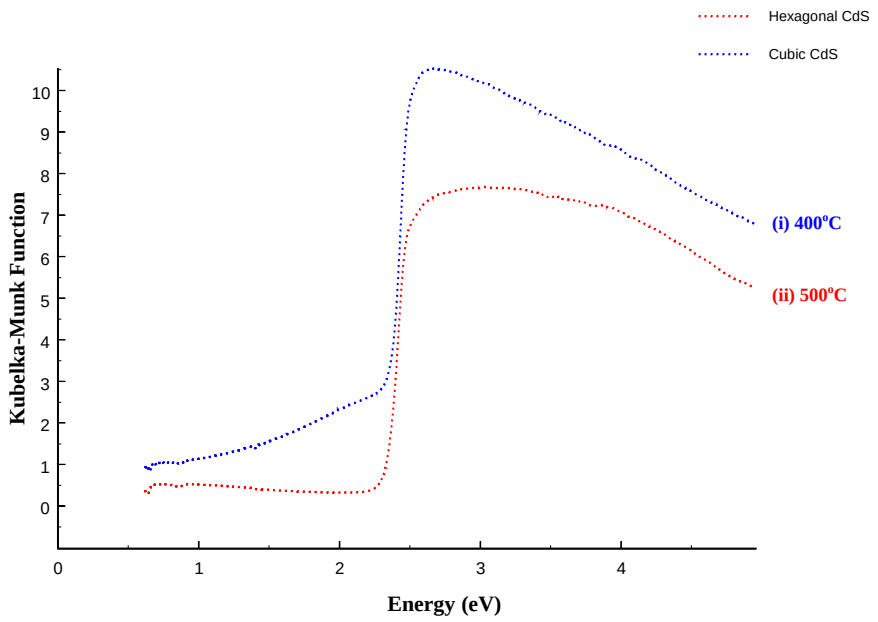

Figure 3.2 Optical absorption spectra of the CdS ((i) 400 ^{o}C and (ii) 500 ^{o}C)

In order to investigate morphologies of the films, AFM with tapping mode was performed onto SiO_2/Si substrates. The surface morphology of the cubic phase CdS (see Fig.3.3(a)) shows rounded grains with an average size of ~1μm. As seen in Figure 3.3, a well connected and continuous surface was also created for both cubic and hexagonal CdS films annealed at 400^{o}C and 500^{o}C, respectively. The average thickness of both films was ~100nm by AFM.

Hall mobility measurements were conducted on both CdS thin films. Results are listed in Table 2.1.[22]

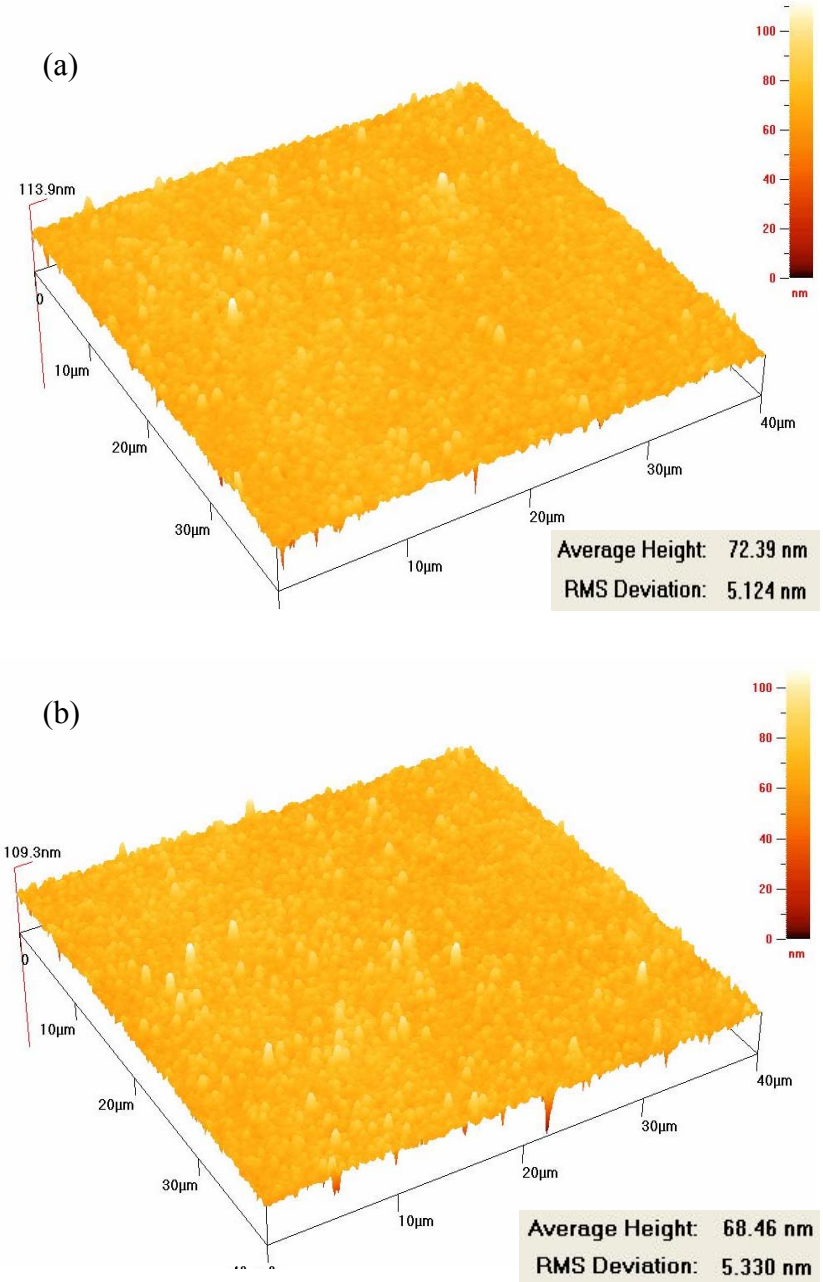

Figure 3.3 Morphologies of CdS films annealed at 400^{o}C (a) and 500^{o}C (b)

Table 3.1 Comparison of electrical properties of CdS

	Annealing Temp. (°C)	Mobility (cm^2/Vs)	Resistivity ($\Omega^{-1}\cdot cm^{-1}$)	Electron concentration (cm^{-3})
Cubic-CdS	400	421	0.44	2.7×10^{16}
Hexagonal-CdS	500	303	0.003	$6.5\ x10^{18}$

The electrical conductivity of the films is substantially higher than those reported earlier by chemical bath deposition techniques.[23-25] These higher values might come from a different growth mechanism. The mechanism of CBD process for CdS films can be explained by an ion-by-ion mechanism, explained in detail in introduction chapter.[26] Such a mechanism generates films with many grains and grain boundaries, which can have an effect on the electrical properties. [27] On the other hand, spin coating deposition, in which solution spreads out onto a substrate, and film growth takes place after drying and annealing, can create continuous films. In particular multi-step spin coating is especially useful to produce more continuous and uniform film compared to CBD method. These procedures might improve electrical properties.[28] The mobility of the films decreases as temperature increases, as shown in Figure 3.4(a).

Photoluminescence (PL) spectra of hexagonal CdS were measured at room temperature and emission was found at 2.16 eV, as shown in Figure 3.4(b). However, no PL was observed for the cubic phase CdS films.[22]

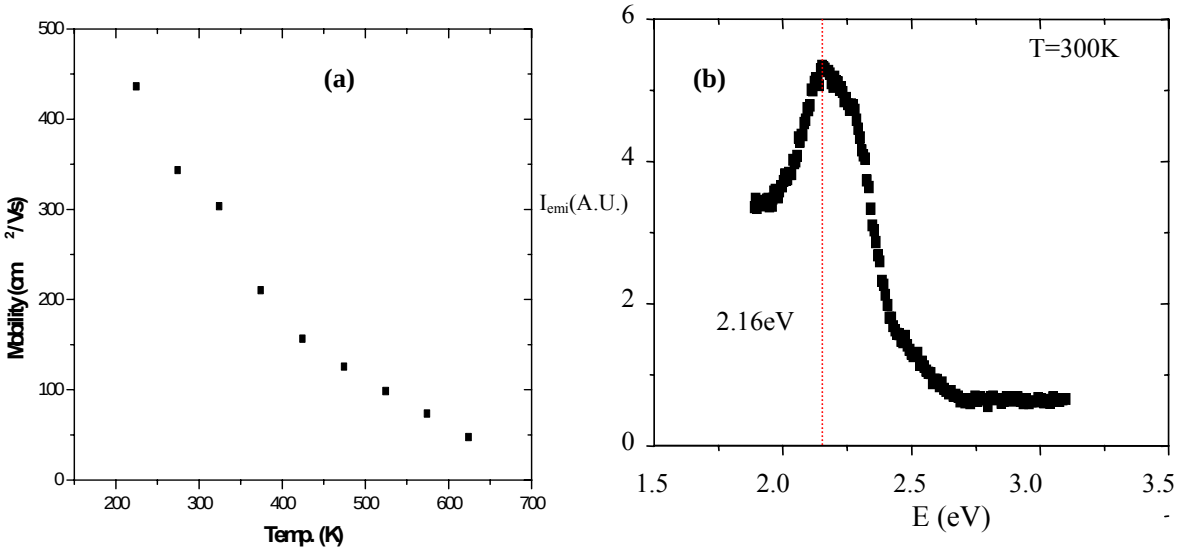

Figure 3.4 (a) Hall mobility of hexagonal CdS films as a function of temperature. (b) Photoluminescence spectra of hexagonal CdS at 300K deposited on glass (contribution from glass is subtracted).

The conversion efficiency of the cells was measured by the current-voltage (*I-V*) curves under illumination as shown in Figure 3.5.[29] It is interesting to note that as concentration of CdS increases, the efficiency increases. On the other hand, the temperature increases, the cell efficiency decreases. The best cell efficiency was found to be 0.12% at 1mM CdS at 150^{o}C for 2hours in vacuum oven.

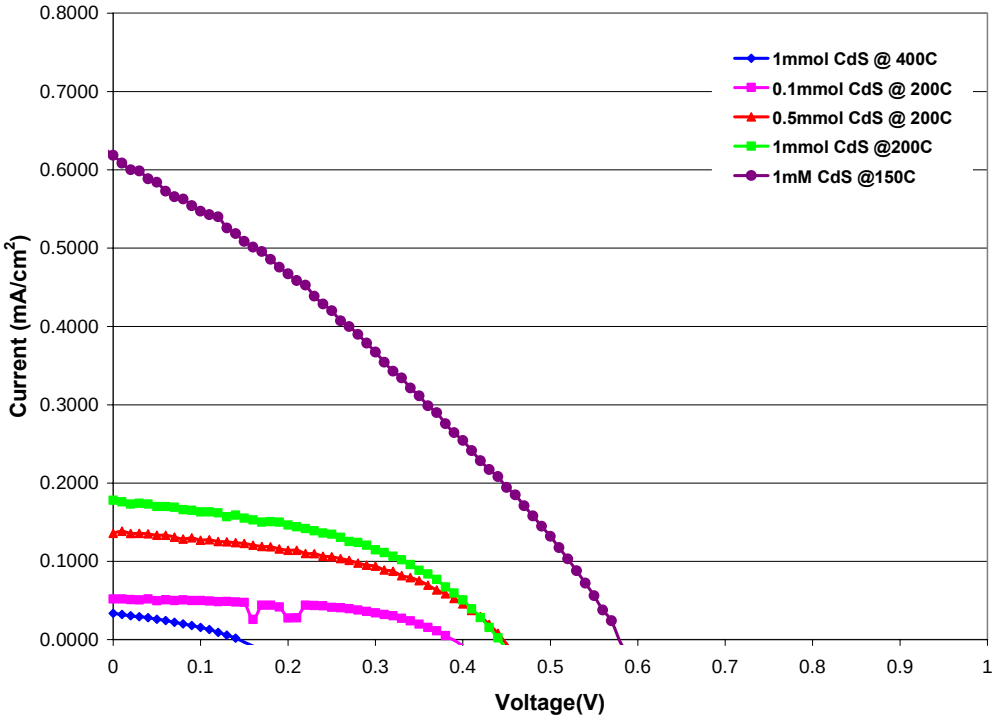

Figure 3.5 Photocurrent–voltage measurements with different conditions CdS-on-TiO_2 electrode

3.4 Conclusion

CdS thin films were successfully fabricated using solution based deposition by spin coating techniques. Cubic CdS thin films with low resistivity were obtained at relatively low temperature below 400^{o}C. At high temperature ~500C, hexagonal CdS structure was found to be favorable. Photoluminescence spectra of hexagonal CdS were measured at room temperature and emission was found at 2.16 eV, while cubic CdS were not found in PL spectrum. Band gap energy of both structures is estimated to be ~2.3eV, which makes it suitable for use as an optical window in photovoltaic cells. Nanostructured photovoltaic devices were fabricated using a porous n-type TiO_2 film with a thin layer of CdS acting as the absorber. The best cell with condition of 1mM CdS in DMSO at 150^{o}C showed conversion efficiency of 0.12% at 1 sun.

3.5 References

1. Contreras, M. A.; Ramanathan, K.; AbuShama, J.; Hasoon, F.; Young, D. L.; Egaas, B. and Noufi, R. *Prog. Photovolt: Res. Appl*. **2005,** *1,*209–216.

2. Morales-Acevedo, A. *Sol. Energy Mater. Sol. Cells* 2006, *90*, 2213.

3. Wu, X.; Keane, J. C.; Dhere, R. G.; DeHart, C.; Duda A.; Gessert, T. A.; Asher, S.; Levi, D. H. and Sheldon, P. Conference Proceedings, 17th European Photovoltaic Solar Energy Conference, Munich, 22–26 October 2001; 995–1000.

4. Voss, C.; Subramanian, S. and Chang, C. H. *J. Appl. Phys*. **2004**, *96*, 5819.

5. Chang, Y.-J.; Munsee, C. L.; Herman, G. S.; Wager, J. F.; Mugdur, P.; Lee, D.-H. and Chang, C.-H. *Surf. Interface Anal.* **2005**, *37*, 398.

6. Meth, J. S.; Zane, S. G.; Sharp, K. G. and Agrawal, S. *Thin Solid Films* **2003**, *444*, 227–234

7. Gana, F. Y. and Shih, I. *J. Vac. Sci. Technol.* **2002,** *20*, 1365

8. Tsai, C.; Chuu, D.; Chen, G. and Yang, S. *J. Appl. Phys.* **1996**, *79***,** 9105

9. (a) Dai, C.; Horng, L.; Hsieh, W.; Shih, Y.; Tsai C. and Chuu, D. *J. Vac. Sci. Technol. A*. **1992,** *10*, 484 (b) Ullrich B. and Schroeder, R. *IEEE J Quantum Electron* **2001**, *37***,**1363. (c) Khanlary, M.; Townsenda, P.; Ullrich, B. and Hole, D.E. *J Appl Phys* **2005**, *97*,023512

10. (a) Kaur, I.; Pandya D. and Chopra, K. *J. Electrochem. Soc.* **1980**, *127*, 943. (b) Voss, C.; Chang, Y.; Subramanian, S.; Ryu, S.; Lee T. and Chang, C. *J. Electrochem. Soc.* **2004**, *151***,** C655 (c) Nair, P.; Campos, J. and Nair, M. *Semicond. Sci. Technol.***1998***, 3*, 134 (d) O'Brien P. and Saeed, T. *J. Cryst. Growth* **1996**,*158*, 497 (e) Gorer S. and Hodes, G. *J. Phys. Chem.* **1994**,*98***,** 5338. (f) Nair, M.; Nair, P.; Zingaro, R. and Meyers, E. *J. Appl. Phys.* **1994**,*75*, 1557

11. Ilieva,M.; Dimova-Malinovska, D.; Ranguelov, B. and Markov, I. *J. Phys., Condens. Matter* **1999**, *11***,** 10025

12. Al Kuhaimi, S. *Vacuum* **1998**, *5* , 349

13. H. Uda, H. Yonezawa, Y. Ohtsubo, M. Kosaka and H. Sonomura, *Sol. Energy Mater. Sol. Cells* **2003**,*75*, 219

14. O'Reagan, B. and Grätzel, M. *Nature* **1991**, *353*, 737

15. Grätzel, M. *J. Photochem. Photobiol., A* **2004,** *164,* 3

16. Serpone, N.; Borgarello, E. and Gratzel, M. *J. Chem. Soc. Chem. Commun.* **1984** 342–343.

17. Larramona, G.; Choné, C.; Jacob, A.; Sakakura, D.; Delatouche, B.; Péré, D.; Cieren, X.; Nagino, M. and Bayón, R. *Chem. Mater.* **2006**, *18*, 1688

18. Niitsoo, O.; Sarkar, S.; Pejoux, C.; Rühle, S.; Cahen, D. and Hodes, G. *J. Photochem. Photobiol., A* **2006**, *181*, 306-313

19. Ramírez-Bon, R.; Sandoval-Ina, N. C.; Espinoza-Beltrán, F. J.; Sotelo-Lerma, M.; Zelaya-Angel, O. and Falcony, C. *J. Phys.: Condens. Matter* **1997,** *9*, 10051.

20. Cha, D.; Kim, S. and Huang, N. K. *Mater. Sci. Eng. B* **2004,** *106*, 63

21. George, P. J.; Sánchez, A.; Nair, P. K. and Nair, M. T. S. *Appl. Phys. Lett.* **1995,** *66*, 3624

22. Electrical and optical properties of CdS films were performed in collaboration with Dr. Hongxing Jiang

23. Chaure, N. B.; Bordas, S.; Samantilleke, A. P.; Chaure, S. N.; Haigh, J. and Dharmadasa, I. M. *Thin Solid Films* **2003**, *437*, 10-17.

24. De Melo, O.; Hernández, L.; Zelaya-Angel, O.; Lozada-Morales, R. and Becerril, M. *Appl. Phys. Lett.* **1994**, *65*, 1278

25. Kokaj, J. and Rakhshani, A. E. *J. Phys. D: Appl. Phys.* **2004**, *37*, 1970

26. Hodes, G. Chemical Solution Deposition of Semiconductor Films, Marcel Dekker, Inc. (**2003**)

27. Yamaguchi, K.; Yoshida, T.; Sugiura, T. and Minoura, H. *J. Phys. Chem. B.* **1988,** *102*, 9677

28. Mitzi, D. B.; Koshbar, L. L.; Murray, C. E.; Copel, M.; Afzall, A. *Nature* **2004**, *428*, 299-302.

29. I-V curves of CdS/TiO_2 cells were performed in collaboration with Dr. Dunbar Birnie.

CHAPTER FOUR

Synthesis and Characterization of New Inorganic-Organic Hybrid Semiconductor Materials

4.1 Introduction

As we have noted in previous chapters, metal chalcogenide bulk semiconductors have been studied over the years for their remarkable advantages in various device applications. In order to enhance performance and functionality of bulk semiconductors, tailored semiconductors, which can be modified by crystal size, morphology, and dimensionality, have attracted considerable attention.[1] In particular, inorganic colloidal quantum dots (QDs) are an example of these semiconducting nanostructures in the emerging field of optoelectronic nano-devices. They are of great interest due to their optical tunability by a change in the size of QDs.[1(a)] Furthermore, strong efforts have been made towards fabricating QDs from one dimensional (1D) to three dimensional (3D) structures with quantum confinement by various methods, such as molecular beam epitaxy and self assembly, to enhance functionality and performance.[2] However, it is a great challenge to achieve uniform arrays and periodically ordered lattices of these nanostructures, a requirement for device applications, due to the non-uniform size and weak correlation of the dots.

Recently, a unique class of inorganic-organic hybrid nanostructure semiconductors based on II-VI semiconductors that exhibit uniform and periodic arrangement has been extensively developed via solvothermal reactions.[3] These hybrid nanostructures are composed of single atomic layer of II-VI semiconductors and organic spacers as a link/spacer to inorganic motifs with strong coordinative bonds. Additionally, the structures of these materials can be systematically tuned by using different inorganic and organic components, thus resulting in drastic changes of electronic and optical properties over their parent II-VI semiconductor bulk materials. These inorganic-organic

hybrid materials exhibit broad band-gap tunability by strong quantum confinement on the same large scale as QDs, high absorption coefficients, and large exciton binding energies.

Numerous functional hybrid materials have been synthesized by simple solvothermal reactions that have been commonly used to create tailored semiconductors due to the versatility in creating a variety of nanostructures from 1D to 3D structures for various applications.[4,5]

Tungsten oxide based semiconductor materials have attracted increasing interest because of their unique properties for various applications such as, optics, catalysis, and electronics via solvo (hydro) thermal reactions.[6] For instance, $ZnWO_4$ has demonstrated photocatalytic activity, potential as a scintillator, and showed promise in humidity detectors.[7] $CdWO_4$, a distant relative of $ZnWO_4$, has been proclaimed highly useful in analytic instrumentation because of its unique luminescence.[8] Even $MnWO_4$ has generated remarkable possibilities as a material used in humidity sensors, as its magnetic properties are affected by temperature.[9]

Here, our attempt has been to synthesize MWO_4 (M=Zn, Cd) and metal chalcogenide based inorganic-organic hybrid semiconductors by incorporating conjugate organic ligands, *meta*-xylylenediamine (*m-xda*) and aniline respectively, to study their optical, thermal, and emission properties via one-pot hydrothermal reactions.

Solvothermal routes, however, rely highly on several conditions, such as temperature, solvents, volume (or molar) ratio to tailoring semiconductors, which means it can be challengeable to fabricate new hybrid materials with one-pot reaction. Since reactions are performed as one pot in autoclaves, it is difficult to understand growth mechanism of the hybrid semiconductors and predict final products.

We have also investigated a modified synthetic method towards developing new hybrid materials with controlled structural dimensions. This method is based on switching organic spacers, which are connected by covalent bonds, with inorganic motifs through breaking and forming lattices. This method allows for high-throughput, high purity, and uniformity of hybrid materials as well as provides valuable information towards a better understanding of the crystal growth mechanism in these hybrid structures.

4.2 Experimental

4.1.1 $MWO_4(m\text{-}xda)_{1/2}$ (M=Zn,Cd)

Both $ZnWO_4(m\text{-}xda)_{1/2}$ and $CdWO_4(m\text{-}xda)_{1/2}$ hybrid semiconductors were synthesized using the solvothermal method. $Na_2WO_4{\cdot}H_2O$ (1.0 mmol) and $ZnCl_2$ (0.2 mmol) were dissolved in a 10 mL mixture of *meta*-xylylenediamine (*m-xda*) and H_2O (volume ratio 3:2), producing $ZnWO_4(xda)_{1/2}$. Similarly, to synthesize $CdWO_4(m\text{-}xda)_{1/2}$, $Na_2WO_4{\cdot}H_2O$ (1.0 mmol) and $CdCl_2$ (1.0 mmol) were dissolved in a 10 mL of the same mixture used to generate $ZnWO_4(m\text{-}xda)_{1/2}$. Complete dissolution of all solids was facilitated by sonication for 10min. The reaction mixtures were loaded in a 23mL Teflon-lined autoclave and heated to 150 ^oC for 4 days. All reactions produced a flaky, white precipitates that were washed with water and ethanol, and subsequently vacuum dried for several minutes at 50 ^oC.

4.2.2 ZnS/Aniline

The solvothermal reaction of $Zn(CH_3COO)_2{\cdot}2H_2O$(1mmol), S(1mmol), and aniline(6mL) in a 23mL acid-digestion bomb at 100^oC for 16 hours afforded peach powder.

4.2.3 2D-ZnSe(N_2H_4) and 3D-ZnSe(N_2H_4)$_{1/2}$

To prepare 2D-ZnSe(N_2H_4), 0.110g of pure 2D-$[ZnSe(ba)]^2$ (*ba* = *n*-butylamine), as a starting material, was placed into a 23mL Teflon-lined autoclave with a stainless steel shell and was filled with 4mL of $N_2H_4{\cdot}H_2O$ and 2mL of H_2O, then heated at 70 ^oC for 5 days in an oven. 3D-ZnSe$(N_2H_4)_{1/2}$ was prepared from same procedures above,

except temperature and time. The reaction was performed at 120 ^{o}C for 7 days. The color of the final products was changed from light pink to pink-orange.

4.3. Results and Discussion

4.3.1 Metal tungstate inorganic-organic hybrid semiconductors via solvothermal reaction

Figure 4.1 shows the similarity between the PXRD patterns of $ZnWO_4(m\text{-}xda)_{1/2}$ and $CdWO_4(m\text{-}xda)_{1/2}$, suggesting that they are isostructural. The first peak is strong and at a very low angle ($2\theta = 6.02^o$), indicating a relatively large unit cell. The $CdWO_4(m\text{-}xda)_{1/2}$ exhibits higher crystallinity than its $ZnWO4(m\text{-}xda)_{1/2}$ based on intensity. .

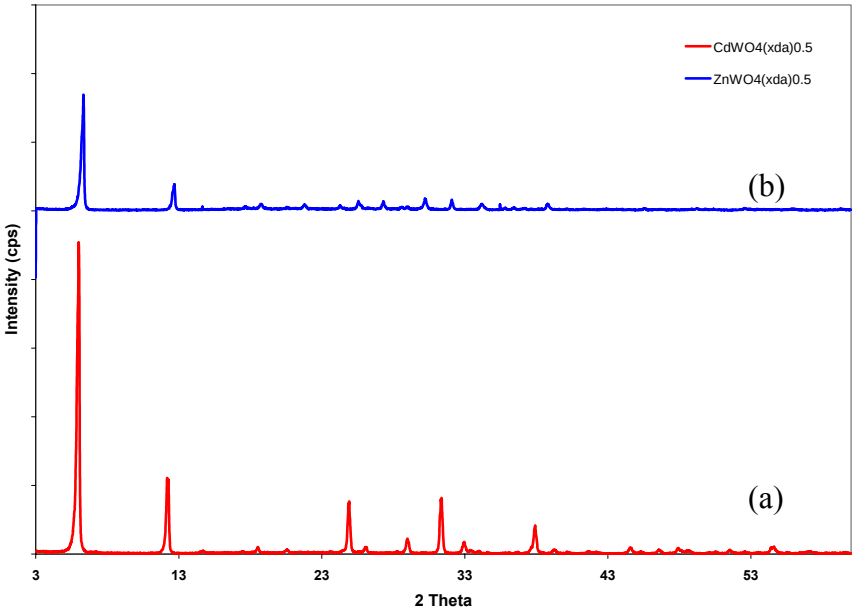

Figure 4.1 PXRD patterns of $CdWO_4(xda)_{1/2}$ (a) and $ZnWO_4(xda)_{1/2}$ (b)

The thermal stabilities of the hybrids were also examined TGA. Both $ZnWO_4(m\text{-}xda)_{1/2}$ and $CdWO_4(m\text{-}xda)_{1/2}$ were heated from ambient temperature (~27 ^oC) to approximately 600 ^oC at a linear rate. From Figure 4.2, a substantial weight loss begins as the sample of $ZnWO_4(m\text{-}xda)_{1/2}$ temperature reaches 375 ^oC and levels off when the

sample is further heated to 425 ^{o}C. The observed percent weight loss here is 16.75 %. This weight loss is attributed to the decomposition of *m-xda* from the hybrid structure, and agrees reasonably well with the calculated weight loss of 17.86 % from $ZnWO_4$(*m-xda*)$_{1/2}$ to $ZnWO_4$. Similarly for $CdWO_4$(*m-xda*)$_{1/2}$, the observed percent weight is 15.40 %, which is in agreement with the calculated weight loss of 15.9 %. The post-TGA residuals were identified to be $ZnWO_4$ and $CdWO_4$ by PXRD as shown in Figure 4.3.

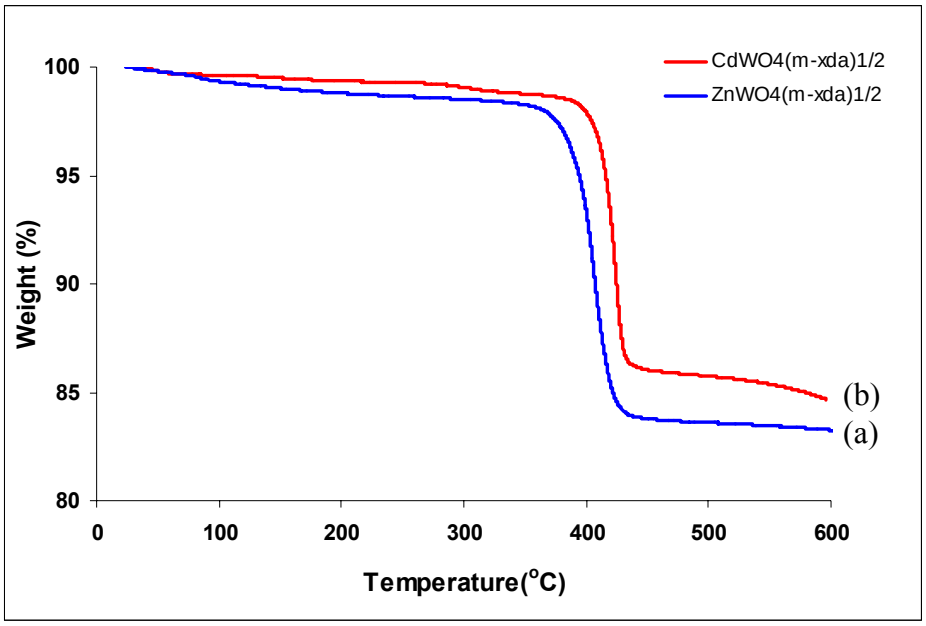

Figure 4.2 The TGA curves of $ZnWO_4$(*m-xda*)$_{1/2}$ (a) and $CdWO_4$(*m-xda*)$_{1/2}$ (b)

The samples were subsequently analyzed using Fourier transform infrared spectroscopy (FTIR) to confirm whether coordination between the ligand and metal tungstate had indeed occurred

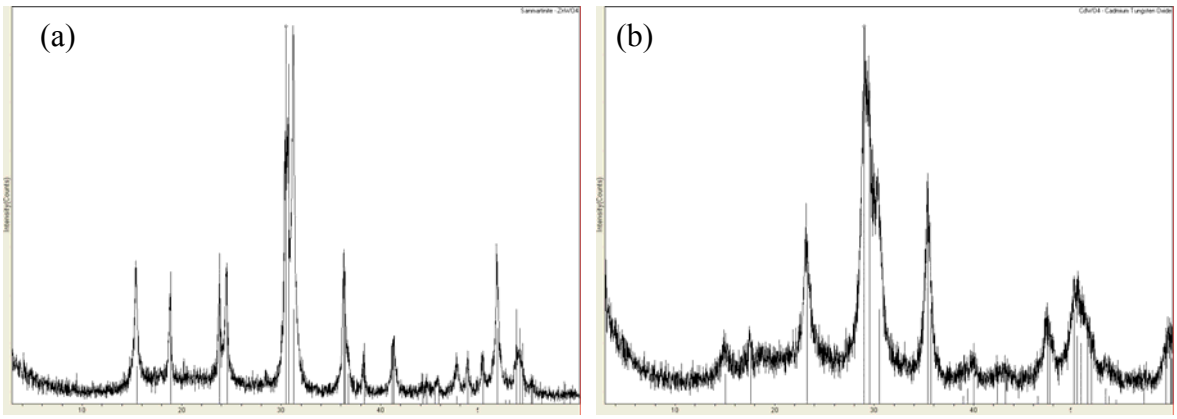

Figure 4.3 PXRD patterns for post-TGA residual of $ZnWO_4$(*m-xda*)$_{1/2}$(a) and $CdWO_4$(*m-xda*)$_{1/2}$(b)

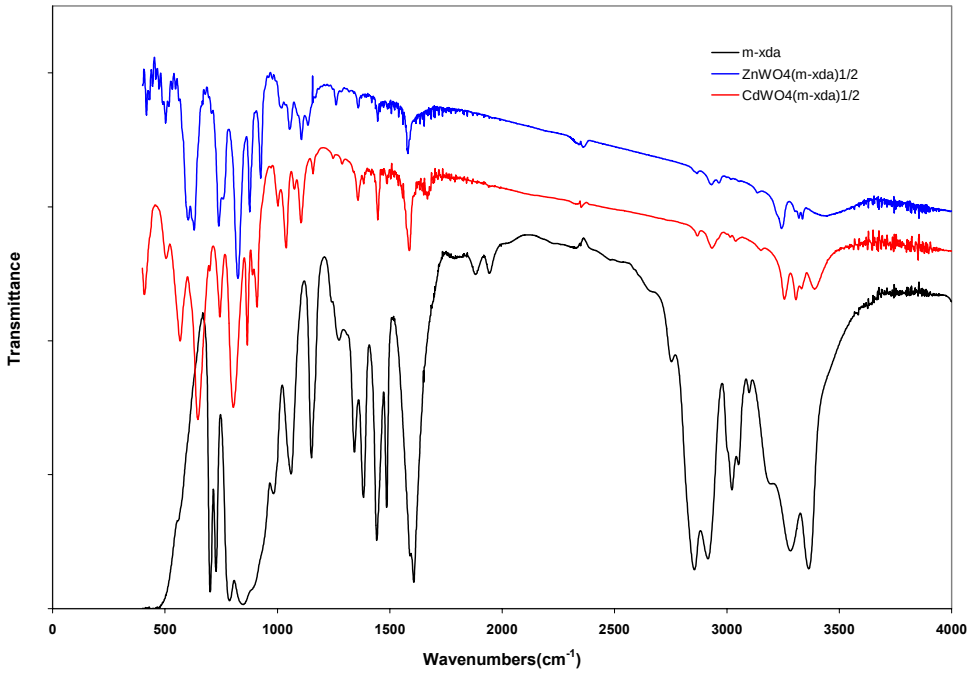

Figure 4.4 FTIR spectrum of $ZnWO_4$(*m-xda*)$_{1/2}$ (blue) and $CdWO_4$(*m-xda*)$_{1/2}$ (red) in comparison with *meta*-xylxylenediamine (*m-xda*).

An infrared spectrum of reagent-grade *m-xda* was taken, in addition to the spectra of both hybrid materials for the sake of comparison as shown in Figure 4.4. As apparent in the FTIR spectrums, there is a noticeable difference in the location of characteristic peaks in the spectrums of the pure ligand and those found in the spectra of the hybrids. For example, the peaks associated with the stretching of the N-H bond found at 3302cm^{-1} and 3373 cm^{-1} in the spectrum of *m-xda* are present in the spectra of both $ZnWO_4$(*m-xda*)$_{1/2}$ and $CdWO_4$(*m-xda*)$_{1/2}$ at 3254, and 3345 cm^{-1}. This peak shift indicates that the chemical environment surrounding the amino functionality in the ligand has changed. This shift is attributed to the interaction of *m-xda* to metal through bonding.

Optical diffuse reflectance spectra were measured at room temperature. Figure 4.5 shows that the absorption edges of both $ZnWO_4$(*m-xda*)$_{1/2}$ is found to be 4.0eV. It has been reported that band energy gap of $ZnWO_4$ was found to be 3.3eV.[10,11] This result indicates a blue shift of 0.7eV. A similar result, using the same organic linker, but ZnSe inorganic component, was found in a recent paper.[12] Their studies indicated that the insulating *m-xda* organic spacer imposes a strong quantum confinement effect on the ZnSe semiconducting layers.

The morphology of the as-prepared samples were investigated with SEM. Figure 4.6 shows an image of $ZnWO_4$(*m-xda*)$_{1/2}$ hybrid material exhibiting long rod like shapes with ~1μm size. Interestingly, morphological changes were reported on $ZnWO_4$ depending on the temperature and time.[13] It was found that the rod-like crystals of $ZnWO_4$ grew larger and became longer with prolonging hydrothermal reaction time and increasing temperature.

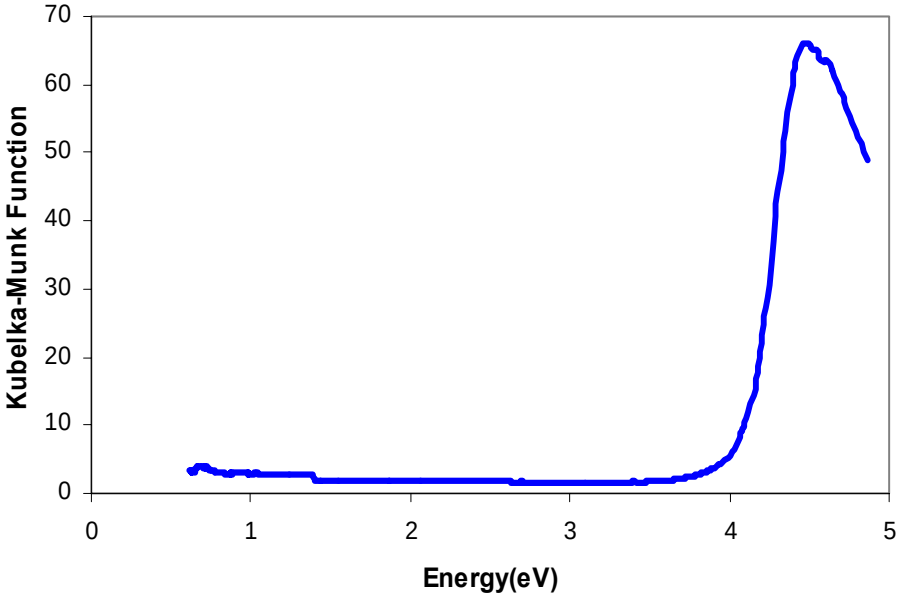

Figure 4.5 Optical absorption spectra of $ZnWO_4(m\text{-}xda)_{1/2}$

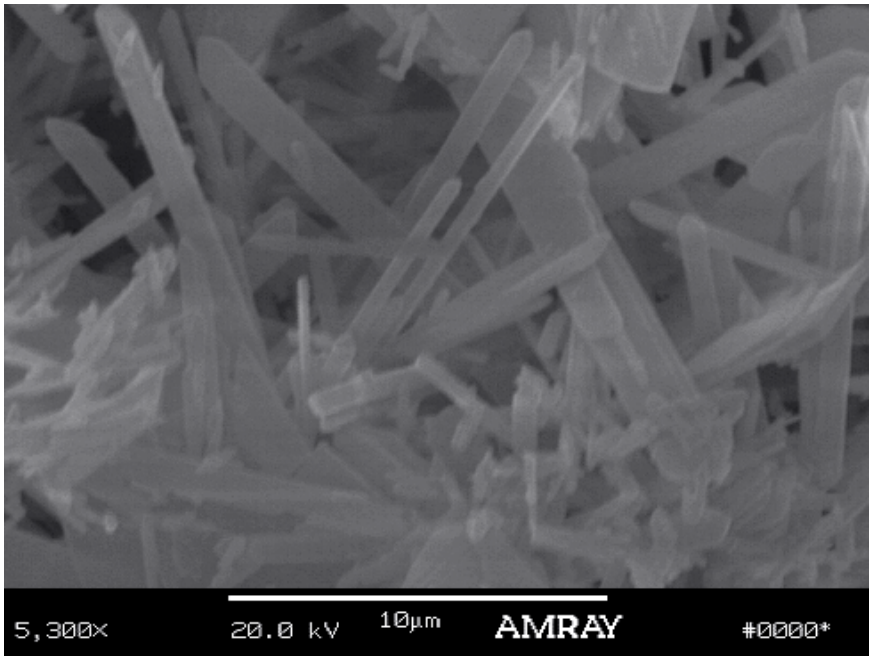

Figure 4.6 A SEM image of $ZnWO_4(m\text{-}xda)_{1/2}$

The room temperature UV-Visible absorption and PL emission spectra of the $CdWO_4(m\text{-}xda)_{1/2}$ hybrid material are plotted in Figure 4.7. $CdWO_4$ powder purchased from Aldrich showed a green-blue PL emission, and the band peaked at 480nm (2.58 eV) which is in well agreement with reported data.[14] $CdWO_4(m\text{-}xda)_{1/2}$ hybrid material shows large band shift to higher energy and the peak of band is present at 386nm(3.2eV). Figure 4.8 shows the CIE (International Commission on Illumination) (*x, y*) coordinates calculated using the software GoCIE.[15] The CIE characterizes colors by a luminance parameter Z and two color coordinates x and y which specify the point on the chromaticity diagram.[16]

The PL of $CdWO_4$ and $CdWO_4(m\text{-}xda)_{1/2}$ chromaticity coordinates of (0.18, 0.24) corresponding to the green-blue region, and (0.17, 0.12) corresponding to the blue region, respectively. The emission of $ZnWO_4(m\text{-}xda)_{1/2}$ has identical band emission with $CdWO_4(m\text{-}xda)_{1/2}$.

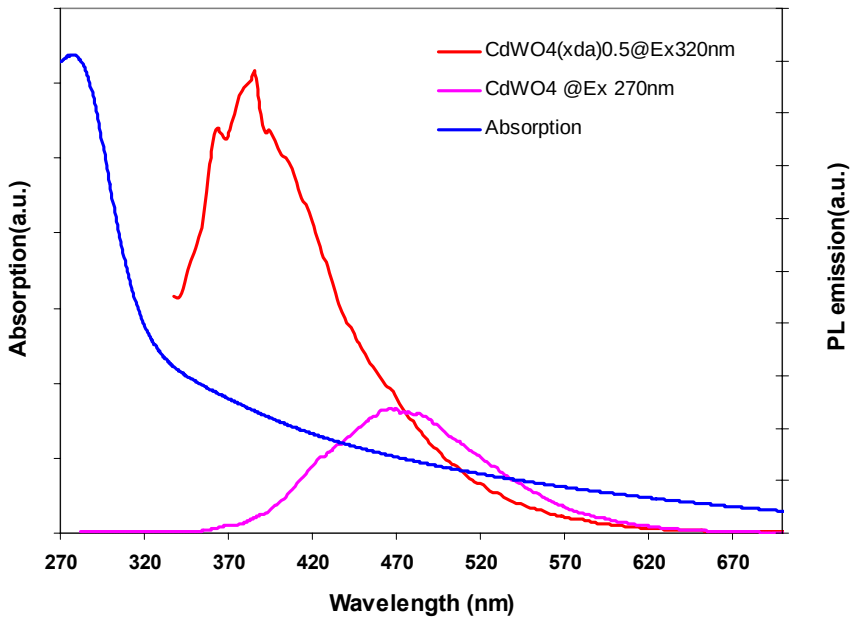

Figure 4.7 The absorption (blue curve) and emission spectra (red curve) of the hybrid and emission spectra of $CdWO_4$ powder for comparison (pink curve).

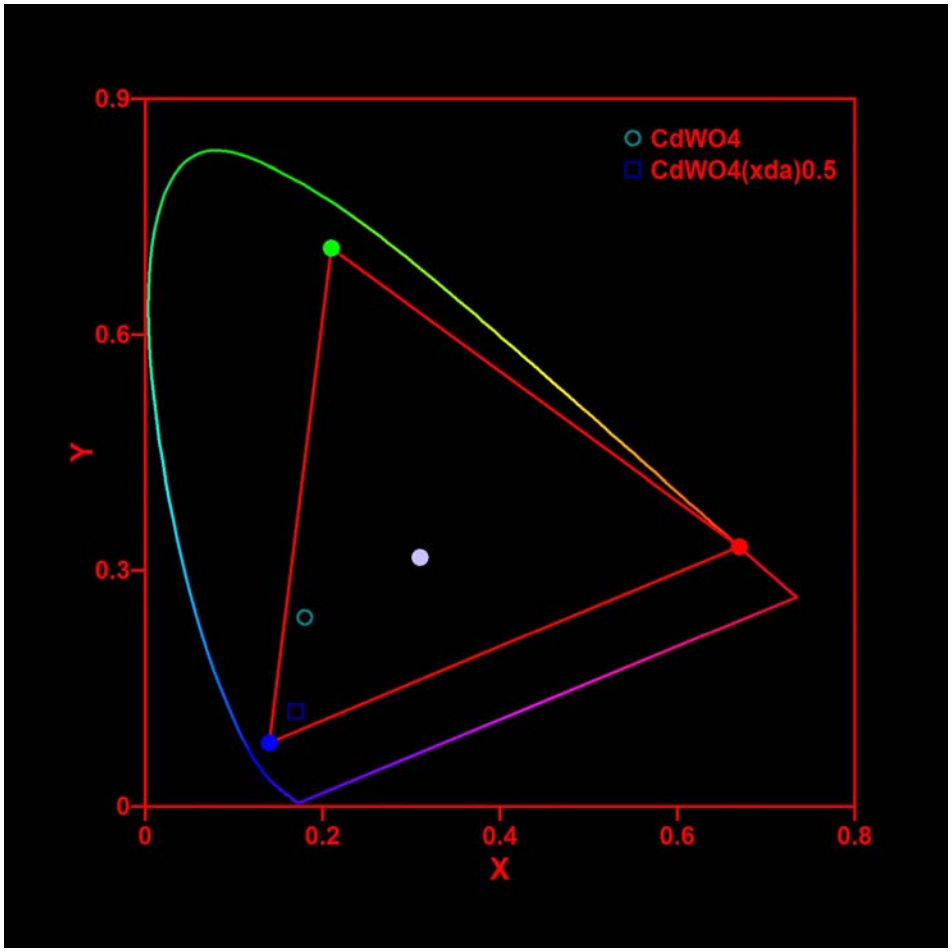

Figure 4.8 CIE diagram showing the chromaticity coordinates of the hybrid and the bulk semiconductors (The white dot indicates the equi-energy white point (0.33, 0.33)).

4.3.2 ZnS/aniline inorganic-organic hybrid materials

A highly crystalline inorganic-organic hybrid semiconductor was obtained as shown in PXRD pattern (Figure 4.9) by reactions of $Zn(CH_3COO)_2 \cdot 2H_2O$(1mmol), S(1mmol), and aniline(6mL) in a 23mL acid-digestion bomb at 100 ^oC for 16 hours.

It is interesting to note that the powder X-ray diffraction pattern of this hybrid material is well matched with the reported diffraction patterns of ZnS/cyclohexylamine, indicating it is most likely an isostructural phase(see the inset of Figure 4.9). [17] This is not surprising, since the two ligands have very similar shape and size, except for the conjugated π-π bond of aniline. ZnS began to form at slightly higher temperature (120 ^oC).

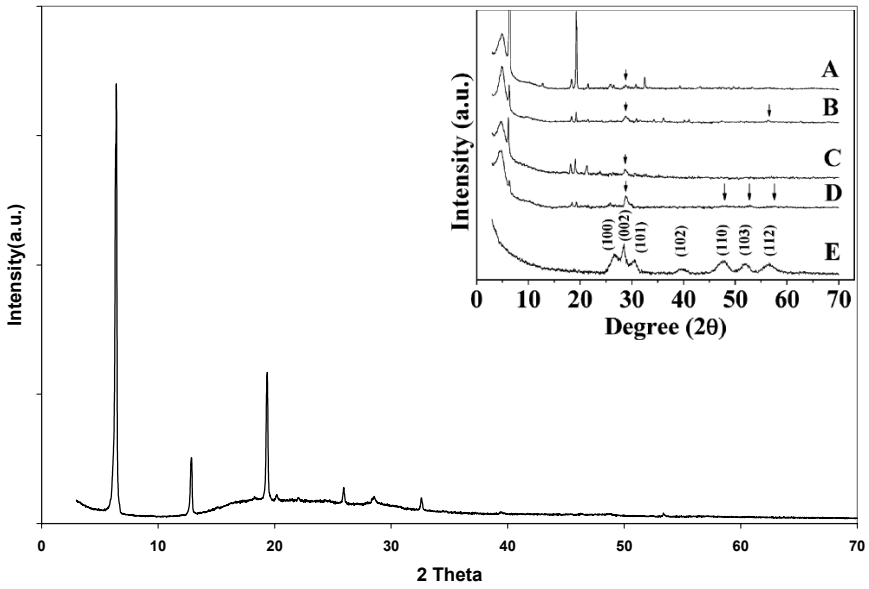

Figure 4.9 A PXRD pattern of ZnS/aniline hybrid materials (An inset shows PXRD patterns of ZnS/cyclohexylamine with depending on reaction conditions)

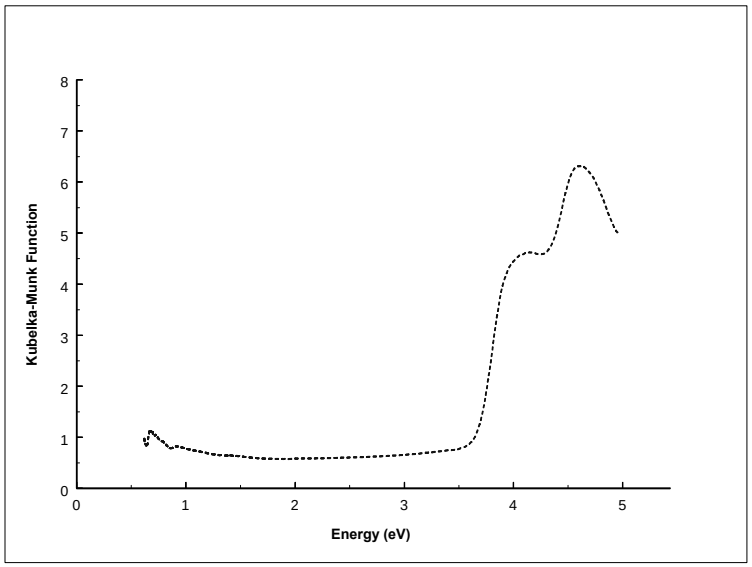

Figure 4.10 optical absorption spectra of ZnS/aniline

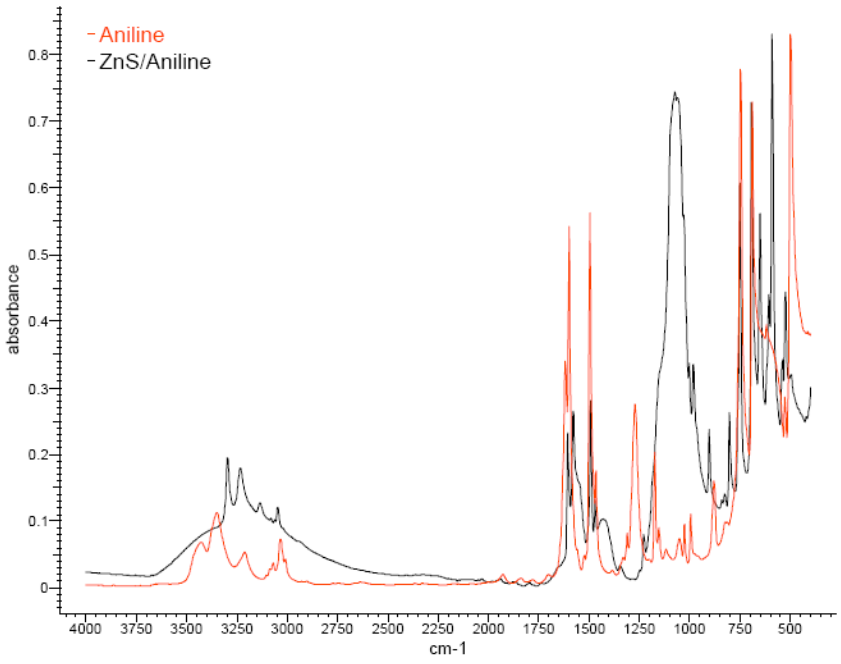

Figure 4.11 Attenuated total reflectance absorption data for ZnS/aniline with a reference of pure aniline

Figure 4.10 shows that the estimated absorption edge from optical absorption spectrum is ~3.6eV, indicating a blue shift (0.4 eV) compared to that of the bulk ZnS (Zinc blende, 3.2 eV). The blue shift is quite small in comparison with the absorption edges of ZnS(*ba*) of 4.5eV and ZnS/cyclohexylamine of 4.3~4.7eV. This small blue shift could come from conjugated π-π bonding interaction with ZnS.

The spectrum of pure aniline (red curve in Fig. 4.11) gives the typical absorbance due to the aromatic ring stretching at 1465, 1496 cm^{-1} and NH_2 scissoring at 1598 and 1617 cm^{-1}. These vibrations also appear in the ZnS/aniline materials. In the case of NH_2 stretching of aromatic ring, which was found at 3349 and 3426cm^{-1}, these vibrations are shifted to 3225 and 3300cm^{-1} in the hybrid system. These shifts are caused by the chemical interactions between ZnS and aniline.

Thermal stability was conducted on a powder sample of ZnS/aniline by TGA, as shown in Figure 4.12. The Post-TGA product was determined by PXRD to be zinc blend ZnS (see inset of Fig.4.17) ~30% weight loss was obtained after 500 ^{o}C. The estimated chemical formula of the ZnS/aniline was ZnS(*aniline*)$_{0.5}$.

To estimate the ZnS/aniline structure, elemental analysis was performed. Data are shown in Table 4.1. Our analysis shows that there is no close correlation between the expected molecular formula, ZnS(aniline)$_{0.5}$ and the experimental values obtained.

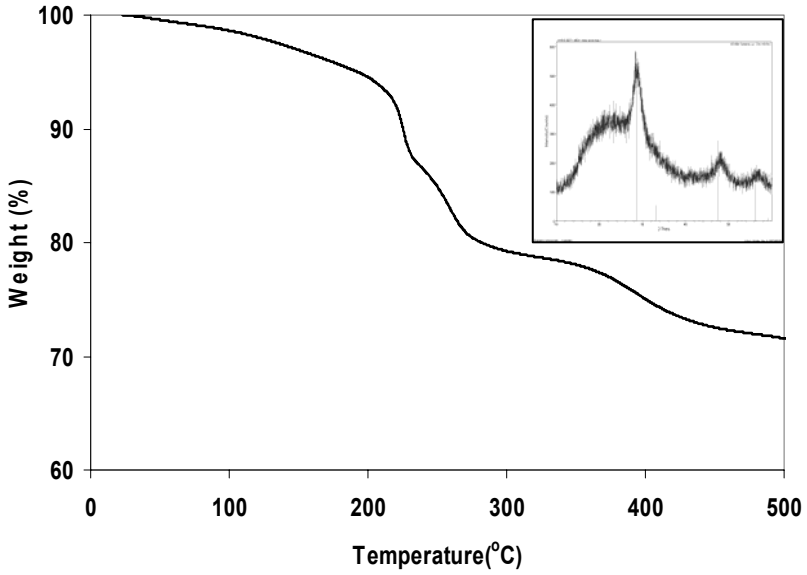

Figure 4.12 TGA data of ZnS/aniline. Inset shows a PXRD pattern of ZnS/aniline after 500°C

Table 4.1 Elemental analysis of ZnS/aniline

Element	% C	% H	%N	% Zn	% S	% O
	23.90	2.85	4.51	44.73	13.28	10.75

The PL measurement of the ZnS/aniline was carried out at room temperature with 280 nm excitation. Figure 4.13 shows very strong band edge emission with a peak at 340nm (3.6eV). This feature is quite different from nanostructured ZnS. The PL spectra of ZnS showed a blue emission band at about 460 nm which could be assigned to the radiative recombination involving defect states in the ZnS nanocrystals.[18]

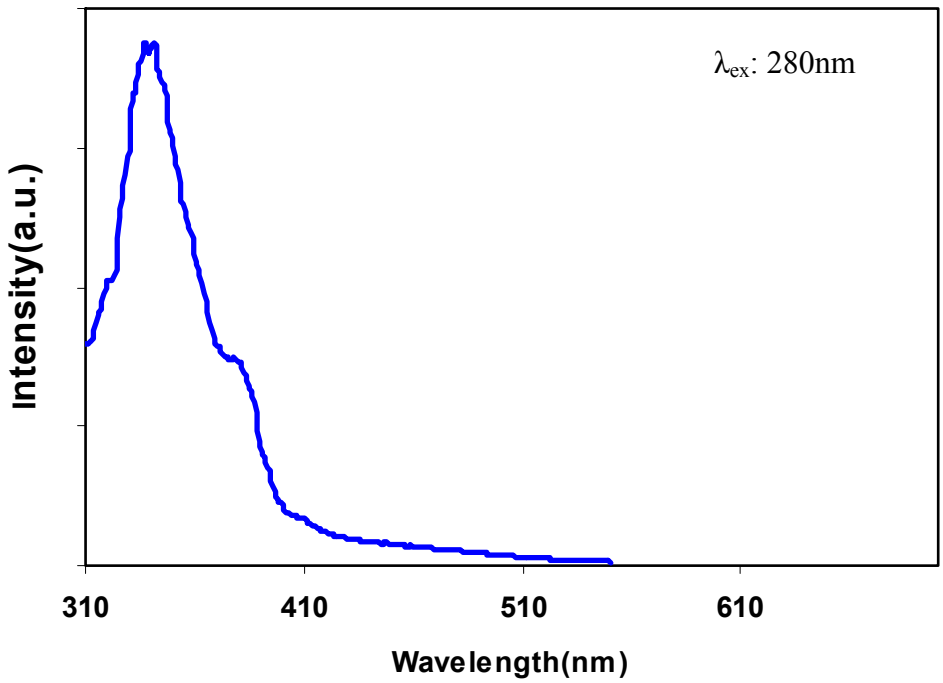

Figure 4.13 The photoluminescence spectrum taken from the ZnS/aniline at room temperature (λ_{ex}: 280 nm)

4.3.3 Organic exchange method via breaking and forming crystal lattices

Powder X-ray diffraction patterns of the final products from the reactions of 2D-[ZnSe(*ba*)] in N_2H_4/H_2O indicate that the structure of 2D-[ZnSe(*ba*)] (Fig.4.14(a)) was completely converted to a new compound as shown in Figure 4.14(b). Comparing the PXRD patterns of this new compound with that of 3D-[ZnTe(N_2H_4)$_{1/2}$] [19] clearly indicates that it is isostructural to 3D-[ZnTe(N_2H_4)$_{1/2}$]. Optical absorption spectra were measured by diffuse reflectance experiments. Figure 4.15 shows that the absorption edge of the new compound was found to be 3.7eV, which is in good agreement with that of 2D-[ZnSe(N_2H_4)]. Based on these data, we assign it as 3D-[ZnSe(N_2H_4)$_{1/2}$]. This implies that the N_2H_4 was replaced by *ba*. Attempts in obtaining a pure phase of 3D-[ZnSe(N_2H_4)$_{1/2}$] via one-pot solvothermal reactions were not successful. Therefore, the ligand replacement reaction was crucial in obtaining a pure phase of this compound.

Figure 4.16 shows the crystal structure of 3D-[ZnTe(N_2H_4)$_{1/2}$]. The structure is composed of [ZnTe] layers interconnected by hydrazine molecules. The [ZnTe] layers in the structure can be regarded as slices cutting along the (110) crystal faces of the würtzite ZnTe binary phase.

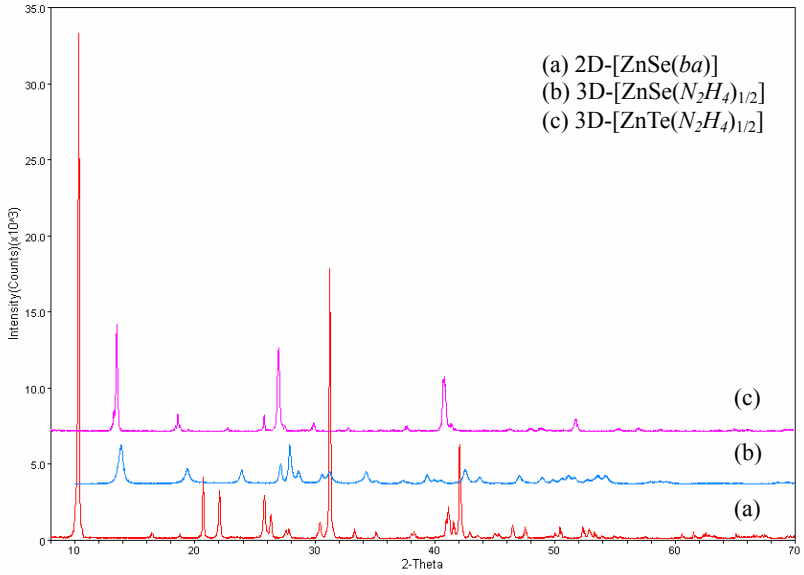

Figure 4.14 PXRD patterns of the starting material (a), final product (b) and reference hybrid material (c).

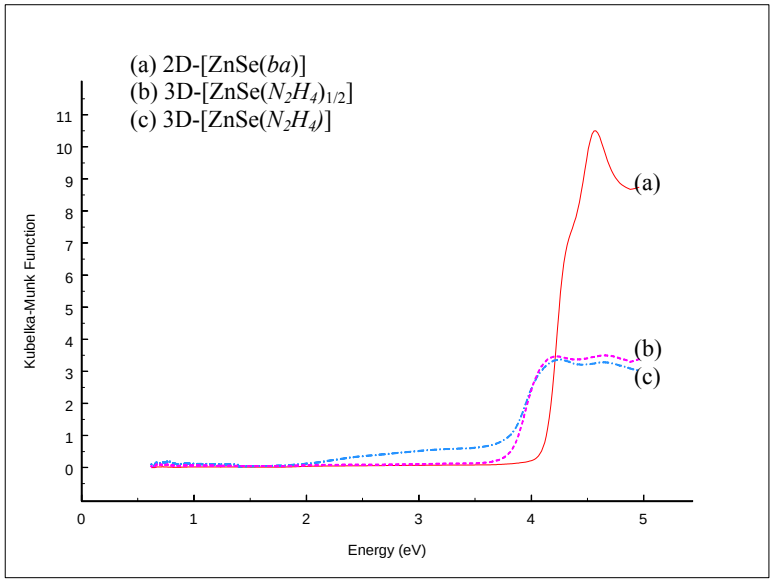

Figure 4.15 Optical absorption spectra of the starting materials (a), final product (b), and reference (c)

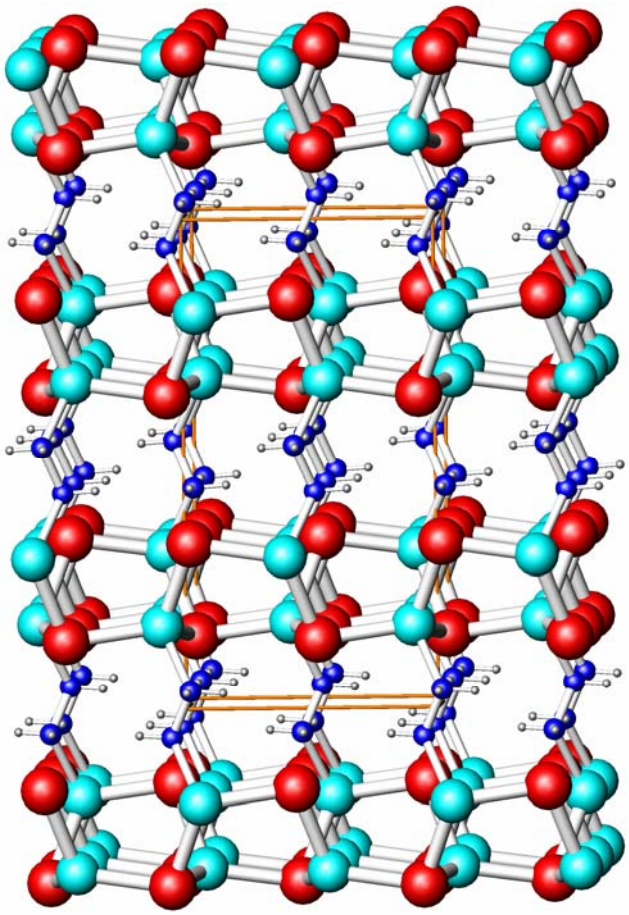

Figure 4.16 View of 3D-[ZnTe(N_2H_4)$_{1/2}$] structure. The light-blue spheres are Zn, the red spheres represent Te, and the blue and gray sphere are N and C, respectively.

Using JADE software, we have refined the unit cell parameters of 3D-[ZnSe(N_2H_4)$_{1/2}$] (a = 6.5612(7)Å b = 6.3933(6) Å c = 12.7455(7) Å, V = 534.64 Å^3). From this study, we can conclude that the monodendate *ba* molecules that are connected to ZnSe motifs were completely exchanged by bidendate hydrazine molecules to form a 3D structure via a process of breaking and reforming crystal lattice at given conditions. This is a rare example where a 3D structure is formed via bonding of hydrazine molecules, because most hydrazine based semiconductors reported thus far exhibit 1D or 2D structures.[20]

It is interesting to note that 2D-[ZnSe(N_2H_4)] was obtained from 2D-[ZnSe(*ba*)] under lower temperature at 70 ^oC for 5 days, while keeping other experimental parameters unchanged (Figure 4.17). This result indicated that the synthesis temperature plays an important role in tuning the dimensionality of hybrid materials in this approach. The mode of hydrazine molecules, either monodendate or bidendate, is temperature dependent, and can therefore be exploited in controlling the dimensionality of the desired structures. Interestingly, conversion of this hybrid material is reversible from 3D-[ZnSe(N_2H_4)$_{1/2}$] to 2D-[ZnSe(*ba*)] under a similar condition using *ba* as solvent.

Table 4.3 summarizes additional studies of hybrid materials via this approach. (PXRD and optical absorption spectra were shown in Appendix I)

As seen in Scheme 1, the dimensionality of the hybrid materials, produced by combining ZnSe and amines, depends on the nature of organic molecules, and their coordination mode (e.g. monodendate or bidendate).

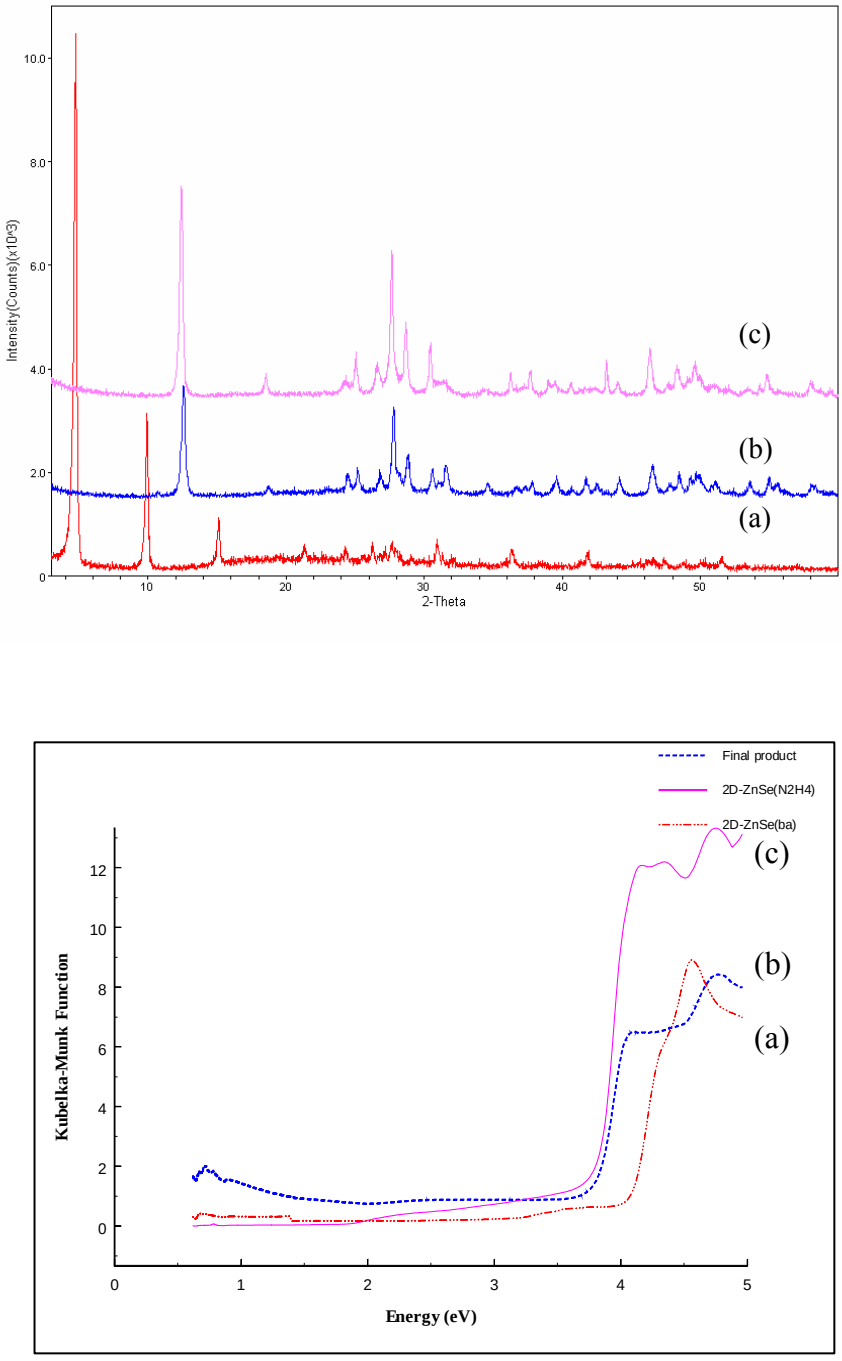

Figure 4.17 Top: PXRD patterns for each hybrid material. Bottom: optical absorption spectra for each hybrid material. (a) 2D-[ZnSe(*ba*)] as starting material, (b) 2D-[ZnSe(N_2H_4)] as final product, and (c) 2D-[ZnSe(N_2H_4)] as reference.

Table 4.3 More studies on hybrid nanostructure by organic exchange methods: ethylenediamine (*en*); 1,3-propanediamine (*pda*); 1,4-butanediamine (*bda*); 1,6-hexanediamine (*hda*); Hydrazine (N_2H_4); n-propaneamine (*pa*); n-butylamine (*ba*), n-hexylamine (*ha*)

Starting materials	Conditions			Final products
	Solvent	Temperature (^oC)	Time (days)	
1D-ZnTe(*pda*)	2mL $N_2H_4{\cdot}H_2O$ +4mL H_2O	145	6	3D- α-ZnTe$(N_2H_4)_{1/2}$
2D-ZnSe(*ba*)	10mL *pa*	150	4	2D-ZnSe(*pa*)
	10mL *ha*	150	4	2D-ZnSe(*ha*)
	6mL *pda*	150	10	3D-ZnSe$(pda)_{1/2}$
	6mL *bda*	150	10	3D-ZnSe$(bda)_{1/2}$
3D- β-ZnTe$(en)_{1/2}$	6mL *pda*	175	4	3D-α-ZnTe$(pda)_{1/2}$
	2mL $N_2H_4{\cdot}H_2O$ +4mL H_2O	150	5	3D-α-ZnTe$(N_2H_4)_{1/2}$

As shown in Table 4.3, the starting material, the 3D-β-ZnTe$(en)_{1/2}$, shows a phase conversion from the β phase (or the one with the II-VI slabs resembling the (110) of the zinc blende structure), to the α phase (or the one with the II-VI slabs resembling the (110) of the würtzite structure), during the solvent exchange reactions. This phase transition is observed when the ligand *en* is replaced with both *pda* and N_2H_4 which lead α-ZnTe$(pda)_{1/2}$ and α-ZnTe$(N_2H_4)_{1/2}$, respectively.

When longer diamines, such as *bda* and *hda,* have been employed to replace *en* in 3D-ZnTe(*en*)$_{1/2}$, a mixture of products containing both the original and target spacers were obtained. This is an indication that the reaction has not reached completion under the given conditions.

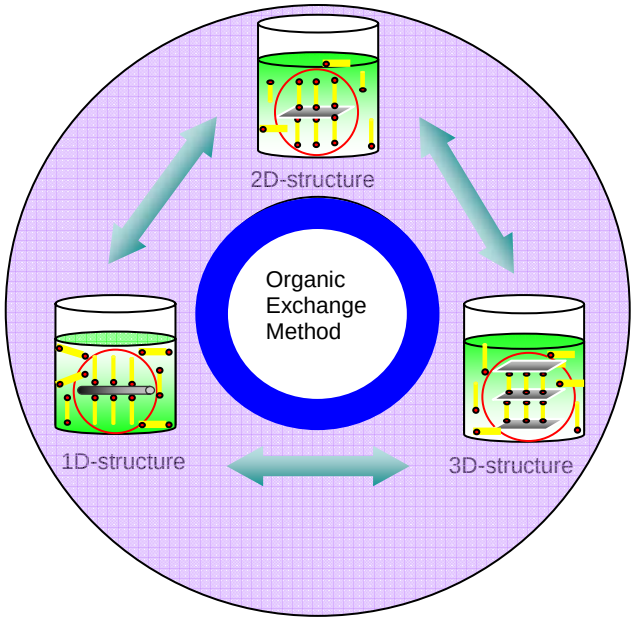

Scheme 4 Schematic illustration of organic exchange method towards new inorganic-organic hybrid semiconductor materials

4.4 Conclusion

New type of metal chalcogenide and oxide based inorganic-organic hybrid materials were successfully synthesized by simple and efficient solvothermal route. The optical properties of the hybrid materials were tuned by changing organic ligands and inorganic elements. Conjugated organic ligands were incorporated in the structure and showed very different behavior from the parent structures in terms of optical absorption spectra and emission properties.

We have also investigated a new synthetic approach via organic spacer exchange to synthesize new II-VI hybrid semiconductors. This new synthetic approach draws on the benefit of rational synthesis and improves the purity of samples without any loss of final products. In addition, this can be useful for designing the dimensionality of hybrid materials. The process may also help to understand the growth mechanism of hybrid materials. This method could lead the potential applications by taking advantage of numerous organic ligands that connecting inorganic slab, thus modifying optical and electrical properties.

4.5 References

1. (a) Alivisatos, A. P. *Science* **1996**, *271*, 933. b) Wang, D.; Luo, H.; Kou, R.; Gil, M. P.; Xiao, S.; Golub, V. O.; Yang, Z.; Brinker, C. J. and Lu, Y. *Angew. Chem. Int. Ed*. **2004**, *43*, 6169. c) Coe, S.; Woo, W.-K.; Bawendi, M. and Bulovic, V. *Nature* **2002,** *420*, 800.

2. (a) Gruetzmacher, D.; Fromherz, T.; Dais, C.; Stangl, J.; Mueller, E.; Ekinci, Y.; Solak, H. H.; Sigg, H.; Lechner, R. T.; Wintersberger, E.; Birner, S.; Holy, V. and Bauer, G. *Nano Lett.* **2007**, *7*, 3150-3156. (b) Wang, Z. M.; Liang, B.; Sablon, K. A.; Lee, J.; Mazur, Y. I.; Strom, N. W.; Salamo, G. J. *Small* **2007**, *3*, 235 – 238. (c) Yang, C. S.; Wang, J. S.; Lai, Y. J.; Luo, C. W.; Chen, D. S.; Shih, Y. T.; Jian, S. R. and Chou, W. C. *Nanotechnology* **2007**, *18***,** 385602.

3. (a)Huang, X.-Y.; Li, J.; Fu, H. *J. Am. Chem. Soc.* **2000**, *122*, 8789. (b) Huang,X.; Li, J.; Zhang, Y.; Mascarenhas, A. *J. Am. Chem. Soc*. **2003,** *125*, 7049-7055. (c) Huang, X.Y.; Heulings IV, H. R.; Le, V.; Li, J. *Chem. Mater*. **2001**, *13*, 3754. (d) Heulings IV, H. R.; Huang, X.-Y.; Li, J.; Yuen, T.; Lin, C. L. *Nano Lett.*, **2001**, *10*, 521. (e) Huang, X.-Y.; Li, J. Mater. Res. Soc. Symp. Proc., **2002**, *728*, 17-22. (f) Fluegel, B.; Zhang, Y.; Mascarenhas, A.; Huang, X.-Y.; Li, J. *Phys*. *Rev*. *B,* **2004**, *70(20)*, 205308/1-205308/5. (g) Zhang, Y.; Dalpian, G. M.; Fluegel, B., Wei, S.-H.; Mascarenhas, A.; Huang, X.-Y.; Li, J.; Wang, L.-W. *Phys. Rev. Lett*., **2006**, *96*, 026405. (h) Moon, C.-Y.; Dalpian, G. M.; Zhang, Y.; Wei, S. -H.; Huang, X. -Y.; Li, J. *Chem. Mater.*, **2006**, *18*, 2805. (i)Huang, X. and Li, J. *J. Am. Chem. Soc.* **2007**, *129*, 3157-3162.

4. (a)Fan, L.; Song,H.; Zhao, H.; Pan,G.;Yu, H.; Bai, H.; Li, S.; Lei, Y.; Dai, Q.; Qin, R.; Wang, T.; Dong, B.; Zheng, Z. and Ren. X. *J. Phys. Chem. B* **2006,** *110,* 12948-12953. (b) Gándara, F.; Medina, M. E.; Snejko, N.; Gómez-Lor, B.; Iglesias, M.; Gutiérrez-Puebla, E. and Monge, M. A. *Inorg. Chem.,***2008***, 47*, 6791–6795. (c) Zhou, J.; Zhang, Y.; Bian, G. O.; Li, C. Y.; Chen, X. X. and Dai, J. *Cryst. Growth Des.,* **2008**, *8,* 2235–2240. (d) Li, G.; Xing, Y. and Song, S. *J. Solid State Chem.***2008***,181,* 943-949 (e) Huang, X.-Y.; Heulings IV, H. R.; Li, J.; Yuen, T.; Lin, C. L., *J. Nanosci. & Nanotech*., **2005**, *5*, 1487.

5. (a)Li, Y.; Wang, Z.; Duan, X.; Zhang, G.; Wang, C. *Adv. Mater*. **2001**, *13*, 145. (b) Li, B.; Xie, Y.; Huang, J.; Qian, Y. *Adv. Mater*. **1999**, *11*, 1456. (c) Das, K.; Panda, S. K. and Chaudhuri, S. *J. Crystal Growth* **2008**, *310*, 3792-3799. (d) Wen, B.; Huang, Y. and Boland, J. J. *J. Mater. Chem***. 2008**, *18*, 2011-2015.

6. (a)Ayyappan, S.; Subbanna, G. N. and Rao, C. N. R. *Chem.Eur. J.* **1995**, *1*, 165. (b) Yan, B.; Xu, Y.; Goh, N. K. and Chia, L. S. *Chem. Commun.* **2000**, 2169. (c) Xu, Y.; Lu, J.; and Goh, N. *J. Mater. Chem.* **1999**, *9*, 1599. (d) Hagrman, D.; Warren, C.J.; Haushalter, R.C.; Seip, C.; Johnson, K. M.; LaDuca, R. L. and Zubieta, Jon. *Chem. Mater.* **1998**, *10*, 3294-3297

7. (a)Lin, J.; Lin, J. and Zhu, Y. Inorg. *Inorg. Chem.* **2007**, *46*, 8372-8378. (b) Fu, H.; Lin, J.; Zhang, L. and Zhu, Y. *Appl. Cat. A: Gen.* **2006**, *306*, 58–67

8. Liao, H.-W.; Wang, Y.-F.; Liu, X.-M.; Li, Y.-D. and Qian, Y.-T. *Chem. Mater.,* **2000***, 12,* 2819.

9. Edwin Suresh Raj, A. M.; Mallika, C.; Sreedharan, O. M. and Nagaraja, K. S. *Materials Letters* **2002**, *53*, 316-320.

10. Huang, G.; Zhang, C. and Zhu, Y. *J. Alloys Compd.* **2007**, *432*, 269–276.

11. Fu, H.; Pan, C.; Zhang, L. and Zhu,Y. *Mater. Res. Bull* 2007, 42, 696

12. Gaweł,B.; Łasocha,W. and Zieba, M. *J. Alloys Compd.* **2007***, 442* , 77–79.

13. Fu, H.; Lin, J.; Zhang, L. and Zhu, Y. *Appl. Cat. A: Gen.* **2006**, *306*, 58–67

14. (a) Robertson, D. S.; Ypung, I. M. and Telfer, J. R. *J. Mater. Sci.* **1979**, *14*, 2967. (b) Tanaka, K. *J. Appl. Phys*. **2001**, *89*, 5449.

15. The software was obtained from http://www.geocities.com/krjustin/gocie.html.

16. http://hyperphysics.phy-astr.gsu.edu/hbase/vision/cie.html#c2

17. Fan, L.; Song, H.; Zhao, H.; Pan, G.;Yu, H.; Bai, H.; Li, S.; Lei, Y.; Dai, Q.; Qin, R.; Wang, T.; Dong, B.; Zheng, Z. and Ren. X. *J. Phys. Chem. B* **2006,** *110,* 12948- 12953.

18. Khosravi, A. A.; Kundu, M.; Jatwa, L.; Deshpande, S. K.; Bhagwat, U.A.; Sastry, M. and Kulkarni, S. K. *Appl. Phys. Lett*. **1995**, 672702.

19. Crystal data of 3D-[$ZnTe(N_2H_4)_{1/2}$]1: H_2NTeZn, M = 208.99, Orthorhombic, space group *Pbca* , *a* = 6.9167(5), *b* = 6.8033(5), *c* = 13.2853(10) Å, *V* = 625.16(8) $Å^3$, *Dc* = 4.441 gcm^{-3}, *T* = 100(2) K, $\mu(MoK_\alpha)$ = 16.688 mm^{-1}. 5679 reflections measured, 946 unique (*Rint* = 0.0358), *R* = 0.0273, *wR* = 0.0675 for 903 observed reflections ($I > 2\sigma(I)$).

20. (a)Yao, W.; Yu, S.-H.; Huang, X.; Jiang, J.; Zhao, L. Q.; Pan, L. and Li, J. *Adv. Mater.* **2005**, *17*, 2799. (b) Mitzi, D. B. *Inorg. Chem.* **2005**, *44*, 7078. (c) Li, Y.; Ding, Y. and Wang, Z. *Adv. Mater.* **1999**, *11*, 847.

CHAPTER FIVE

Photoluminescence Studies on Inorganic-organic Hybrid Semiconductor Materials

5.1 Introduction

It has been reported that a reduction of approximately 29% of U.S. energy consumption for lighting could be obtained by 2020 as a result of the mainstream use of solid-state lighting (SSL).[1] Research in SSL technology is an umbrella term containing light-emitting diodes (LEDs) and organic light-emitting diodes (OLEDs) is rapidly growing.[2] By utilizing semiconductor materials, SSL devices convert electricity to light with much higher efficiency than conventional lighting sources and also offer co-friendly environment.[3] Solar-powered LEDs can be a new direction as a renewable energy source.[4]

White-light SSL has great potential to replace conventional lighting sources as a much more efficient device. Currently used approaches are to combine blue, green, and red emitters to achieve a broad spectrum of white light, or by phosphor conversion.[3(a)] Each approach has certain advantages and disadvantages. For example, the RGB method offers potentially high efficiency and color tunability, but poor color control. On the other hand, phosphor conversion approach using blue or UV-LED to pump a mixture of phosphors provides better color control and lower cost, but lower efficiency and less color tunability.[5] Both procedures, however, lead to significant energy loss such as self absorption associated with light capture by the phosphor or nonradiative carrier losses.[6]

Recently, semiconductor nanocrystals (NCs) provide a new technology platform for developing white light phosphors. “Magic sized” CdSe NCs exhibit a broad (white-light) emission covering the entire visible spetrum,[7] as a direct result of very high surface-to-volume ratio and, thus, a significantly larger number of midgap surface sites. These ultrasmall NCs are promising for use as a direct white-light phosphor without

involving complicated doping/mixing procedures. However, since broad emission is achieved from surface states of NCs, it is very difficult to control and tune the emission spectra. Additionally, arranging the quantum dots periodically and uniformly is quite challengeable because of the weak correlations among the NCs, thus leading to low conductivity and carrier mobility. This is the main limitation in their use as active emitting layer in a LED. Therefore, it will be more desirable to develop bulk semiconductor materials that retain excellent transport properties for applications in optoelectronic devices.

To tackle this specific problem we have recently developed a very unique class of II-VI inorganic-organic hybrid semiconductor materials.[8] They exhibit the same or higher degree of strong quantum confinement as that of the smallest quantum dots,[9] more importantly, they have perfectly ordered periodic structures which allow the same level of strong correlations as in pure inorganic lattices required to achieve high conductivity and carrier mobility. These hybrid materials are promising for applications in optoelectronics including solid state lightings and solar cells, due to their broad band gap tunability and high adsorption coefficients. More significantly, these hybrid semiconductor materials posses several advantages over NC semiconductors, such as feasible synthesis, optical tunability, stability, and desirable conduction transport within continuous inorganic layers.

In this chapter, a unique approach to generate direct white light from a single semiconductor bulk material, 2D-Cd_2S_2(*ba*) based double layer structure, is described in detail. We show that their luminescence properties can be tuned systematically by changing composition and doping level.[10] Furthermore, preliminary studies have been carried out on their electrical and transport properties.

5.2 Experimental

5.2.1 2D-[Cd_2S_2(*ba*)] based double layered structures

Double layered 2D-[Cd_2S_2(*ba*)] samples were prepared from reactions of $CdCl_2$ (2mmol), S (1mmol), and *n*-butylamine (*ba,* 6mL) in a 25mL acid digestion bomb at 100^oC for 2 days. A yield of 82.6% based on S was achieved. Mn doped samples, [$Cd_{2-x}Mn_xS_2$(*ba*)], were synthesized by reactions of $CdCl_2$, S, and $Mn(CH_3COO)_2 \cdot 4H_2O$ at various molar concentration (x = 0~5%) under the same conditions as for the parent structure. Selenium substituted samples, [$Cd_2S_{2-x}Se_x$ (*ba*)], were synthesized by reactions of $CdCl_2$, S, and Se at various molar concentration x = 0~50%) at the same conditions.

The "gel-like" sample used to coat a UV-LED was prepared by centrifugation of the sample synthesized as described above in 95% ethanol/distilled water (2:8 v/v) followed by 2nd centrifugation in DMSO (99.9%) to remove excess *ba*. A small amount of the "gel-like" hybrid materials was applied onto a commercial 360nm UV-LED (Le Group Fox Inc.) for white light demonstration used for coating a UV-LED.

For absorption and PL study, the "gel-like "sample of 10mg was then suspended in 10mL DMSO and treated by an ultrasonic processor (Model VCX-750, Sonics & Materials, Inc.) for 30sec with ~30W at room temperature followed by centrifugation Suspended resultant solution was used to measure absorption and PL spectra.

For band gap measurement, filtered powder samples were used to measure optical diffuse reflectance spectra, from which estimated band gap values were obtained by converting to Kubelka-Munk function. Room temperature absorption and photoluminescence measurements were made using a Shimadzu UV-3101PC double beam, double monochromated spectrophotometer and a Varian Cary Eclipse fluorometer,

respectively. Powder X-ray diffraction experiments were carried out on a Rigaku D/M-2200T automated diffractometer (Ultima+) using Cu Kα radiation (λ = 1.5406 Å).

5.2.2 2D- [Cd_2Se_2(*ba*)] based double layered structures

Double layered 2D-[Cd_2Se_2(*ba*)] was synthesized from a reaction of $Cd(NO_3)_2 \cdot 4H_2O$ (2mmol), Se(1mmol), and *ba* (6mL) in a 25mL acid digestion bomb at 120^oC for 5 days. Tellurium substituted samples, [$Cd_2Se_{2-x}Te_x$(*ba*)], were prepared by reactions of $Cd(NO_3)_2 \cdot 4H_2O$, Se, and Te at various molar concentration x = 0~25%) at the same conditions. All procedures for PL measurements were the same as described above.

5.3 Results and Discussion

5.3.1 2D-[Cd_2S_2(*ba*)] based double layered structures

Figure 5.1(a) shows a double layered 2D-[Cd_2S_2(*ba*)] (*ba* = *n*-butylamine) structure. A view of the double layer is depicted in Figure 5.1(b). The double layer [Cd_2S_2] slab can be regarded as a slice from the (110) crystal phase of the hexagonal structure of CdS. The room temperature absorption and emission spectra of the compound are plotted in Figure 5.1(c). The emission spectrum covers the entire visible spectrum with a sharp and strong band edge emission at 408nm which is in good agreement with the band gap energy (~3eV) of the compound. A similar observation was reported for very small CdSe NCs. Rothanthal *et al*.[7,11] explained that the broad emission comes from deep trap emission of NC-CdSe, because the selenium atoms on the surface give rise to dangling bonds which create midgap states, or surface sites. Because of the very small particle size of CdSe NCs, the surface-to-volume ratio is very large, giving rise to dominating surface states, diminished band edge emission features, and a very broad emission.

As shown in Figure 5.2, it is interesting to note that the 2D-double layered [Cd_2S_2(*ba*)] has a large number of surface sites within each crystal, due to the nature of its layered structure, while a single-layer structure made of the same inorganic elements 3D-[CdS(bda)$_{1/2}$] (*bda*=butyldiamine) possess no surface sites within the crystals. Therefore, the 3D structured materials exhibit a significantly narrower emission band width as seen in Figure 5.3.

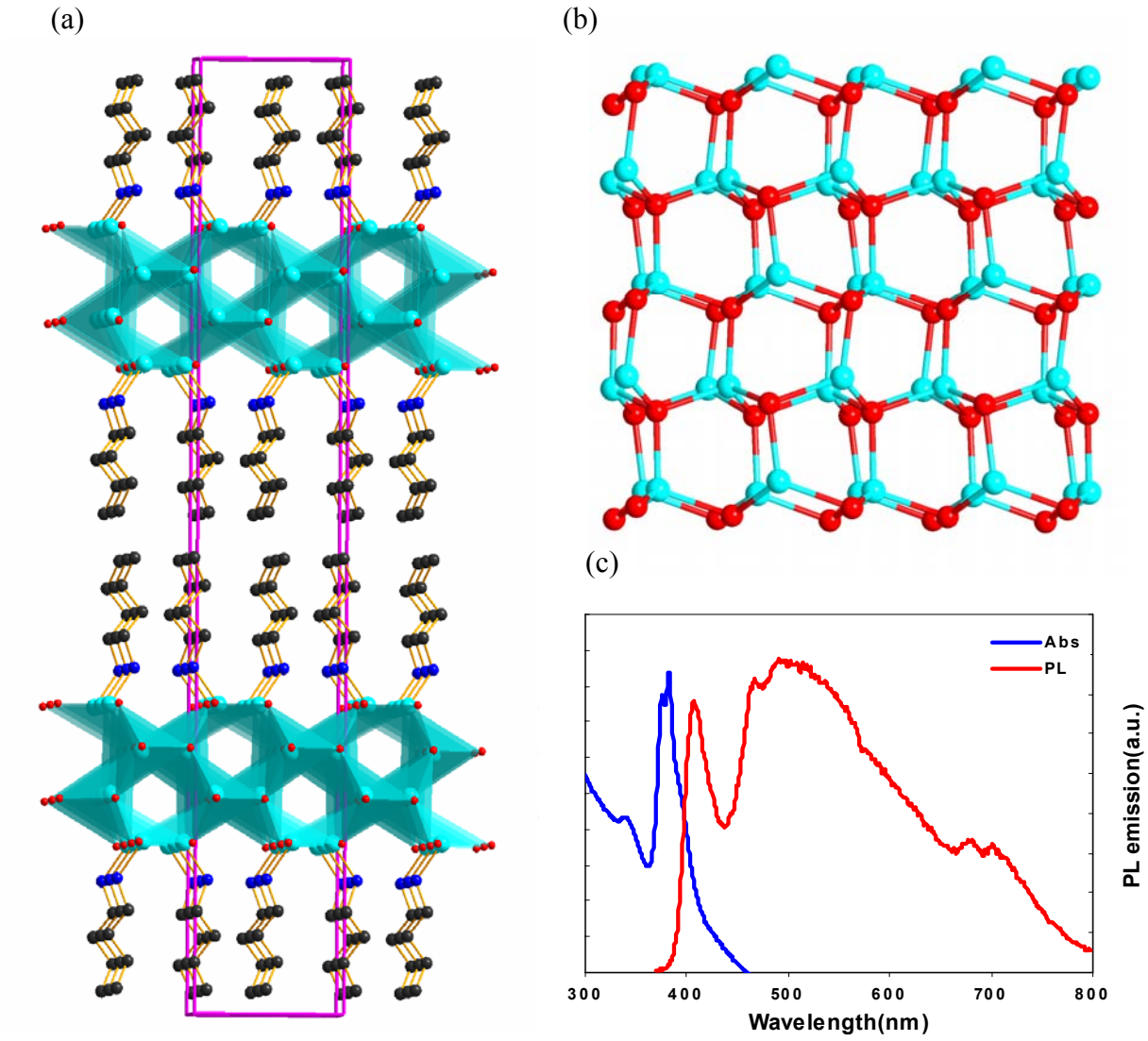

Figure 5.1 The crystal structure, absorption and emission spectra. (a) Side view of the double layered 2D-[Cd_2S_2(*ba*)] crystal structure. Cd: light blue; S: red; N: dark blue; and C: black solid spheres. (b) The double layer of CdS**.** (c) Absorption and emission spectra (λ_{ex} = 360 nm), respectively.[10]

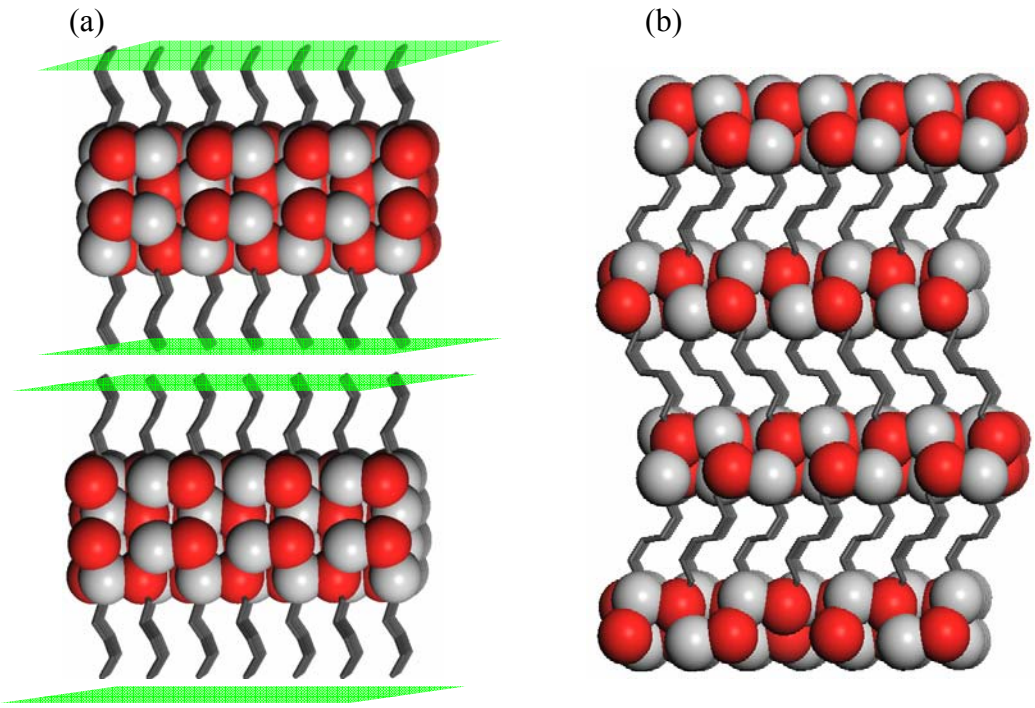

Figure 5.2 **(a)** The double-layer 2D-[Cd_2S_2(*ba*)] structure. The planes in light green color indicate the surfaces of each layer within a unit cell. (b) A single-layer 3D-[CdS(*bda*)$_{1/2}$] structure.[10]

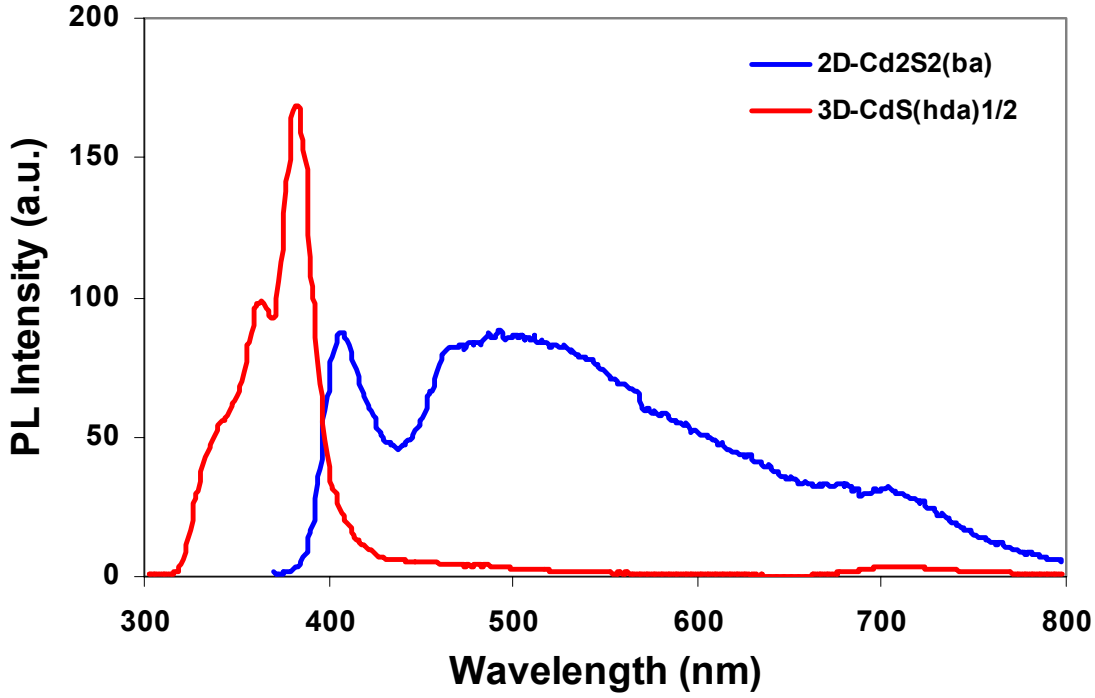

Figure 5.3 Room temperature photoluminescence of the double-layer 2D-[Cd_2S_2(*ba*)] (blue, λ_{ex} = 360 nm) and a single-layer 3D-[Cd_2S_2(*L*)] (red, λ_{ex} = 280 nm) structure.

It is worth to mention that the band edge emission is significantly reduced compared to the parent structure, 2D-[Cd_2S_2(*ba*)], leading to a well-balanced white-light spectrum by substituting Se as shown in Figure 5.4. Substitution of selenium atoms into sulfur sites could create mid gap states, thus decreasing band gap, quenching band gap emission and enhancing the green color regions. The band gap of the 25 mol% Se-[Cd_2S_2(*ba*)],**1**, clearly shows a decrease compared to the material without Se substitution (see Figure 5.5). Addition of Se led to a decrease in the E_g values as well as a tuning of the emission spectra.

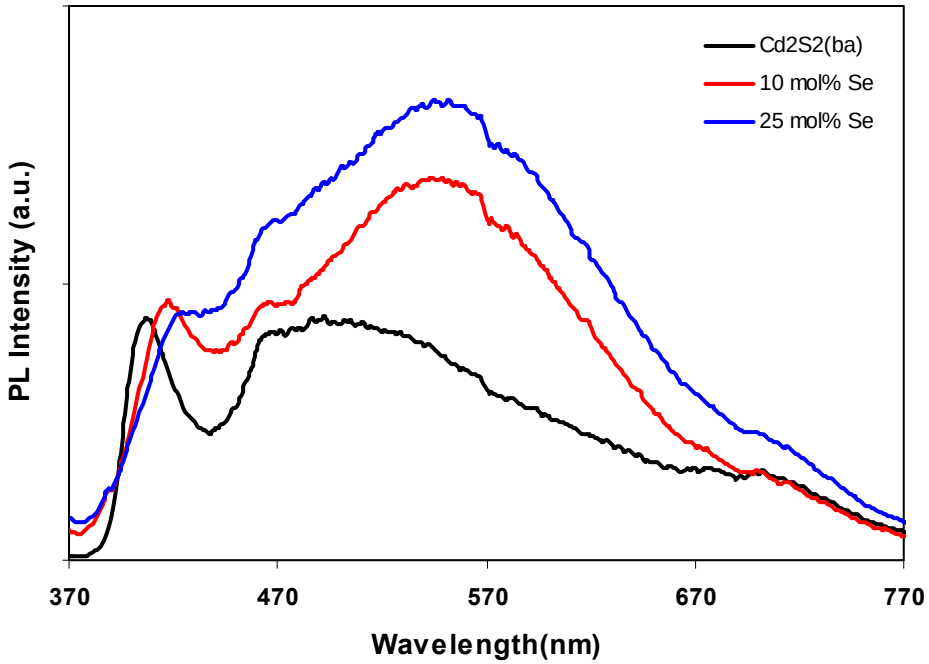

Figure 5.4 Photoluminescence of double layered 2D-[Cd_2S_2(*ba*)] based structures with various substitution of selenium

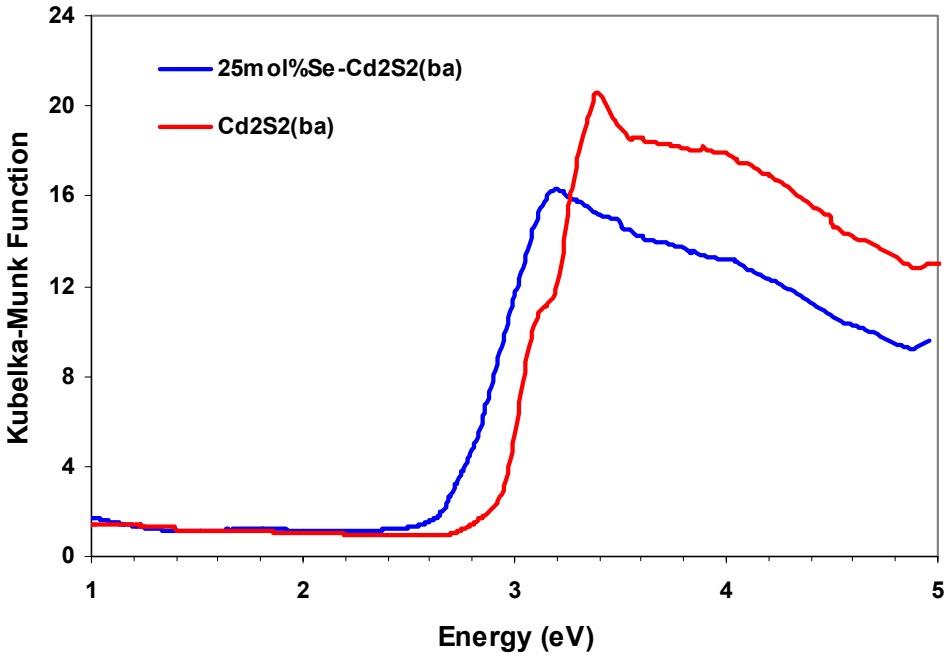

Figure 5.5 Optical absorption spectra of of **1,** 25 mol% Se-[Cd_2S_2(*ba*)], and [Cd_2S_2(*ba*)].

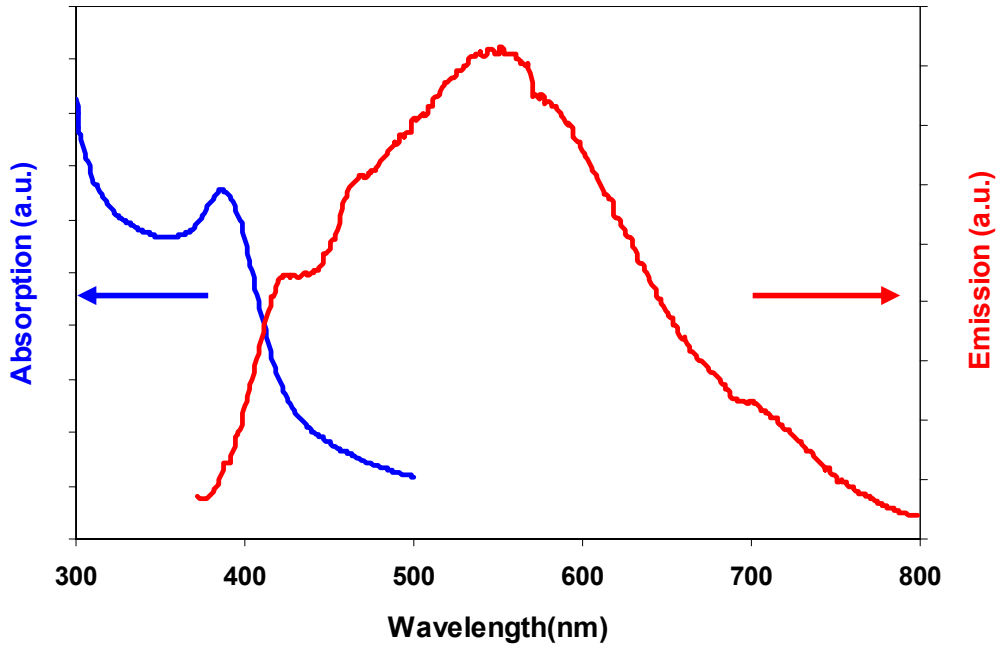

Figure 5.6 The absorption and emission spectra of **1** at room temperature

The absorption and emission spectra of **1** was obtained at room temperature. A absorption peak was found at ~380nm where that of Cd_2S_2(*ba*) was also found. Emission spectrum shows broad emission that covers the entire visible range with an excitation wavelength of 360nm.

Manganese is well known to enhance photoluminescence (PL) in numerous II-VI binary as well as II-VI hybrid materials.[12] As shown in Figure 5.7, a small amount of Mn doping results in changes in the PL intensity. The highest PL intensity was achieved at a dopant level of 0.5mol% Mn. The luminescence enhanced effect of Mn^{2+} doping was explained by Lu *et al.*[12(d)] Mn^{2+} luminescence spectroscopy was used to explain Mn^{2+} luminescence lifetime using luminescence decay dynamics. It showed that the Mn^{2+} doped luminescence lifetime increases significantly at certain regime compared to undoped [CdSe(*hda*)$_{0.5}$]. This means that higher Mn concentration creates electron spin-

spin interaction, thus quenching luminescence. In our experiment, a small amount of Mn doping resulted in changes in the PL intensity. The highest PL intensity was achieved at a dopant level of 0.5 mol % of Mn and drops rapidly by adding more Mn, as shown in Figure 5.7. Figure 5.8 clearly illustrates the trends between integrated fluorescence intensity as a function of Mn dopant level.

Figure 5.9 demonstrates white light emission from **1** and Mn doped **1**. A commercial LED (360 nm) illuminates blue light (see Figure 5.9(a). A thin layer of yellowish-colored parent structure prepared from a DMSO solution was coated onto the LED (Figure 5.9(b)). Upon illumination, it produced white light as shown in Figure 5.9(c) and Figure 5.9(d).

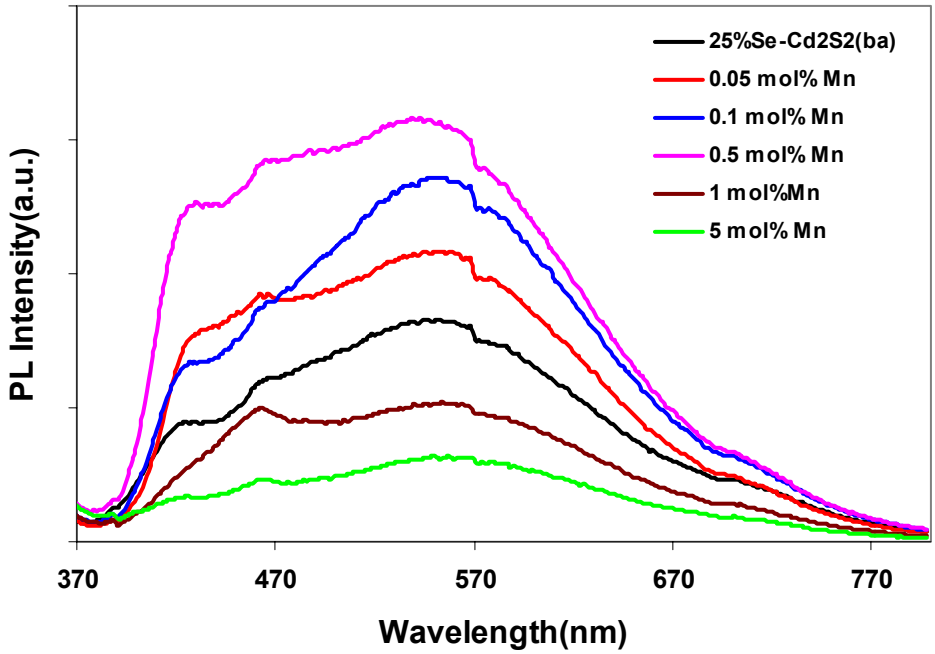

Figure 5.7 Room temperature photoluminescence of **1** and Mn doped samples (λ_{ex} = 360 nm).

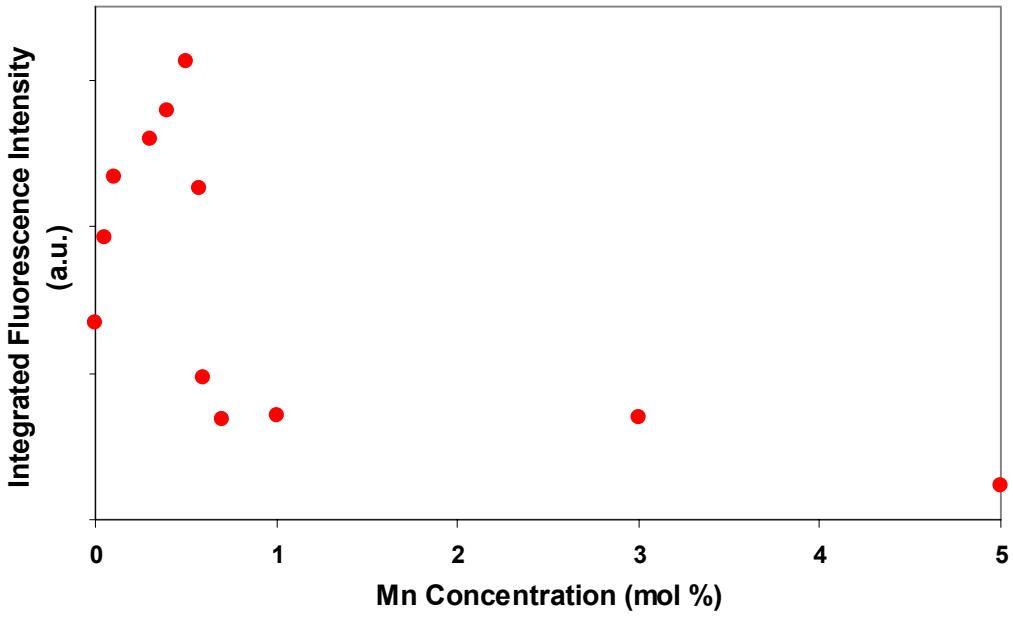

Figure 5.8 The integrated PL intensity as a function of the Mn dopant amount (0 - 5 mol %).

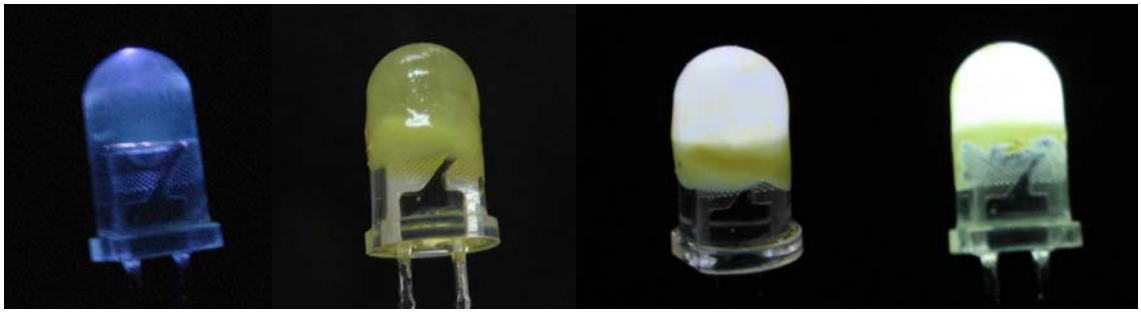

(a) (b) (c) (d)

Figure 5.9 Demonstration of white light emission from the double layered 2D-[Cd_2S_2(*ba*)] based structures. (a) A 5 mm reference UV LED (360 nm) illuminating blue light; (b) The same LED coated with a thin layer of sample **1**, 25mol%Se-[Cd_2S_2(*ba*)], (before illumination); (c) The same LED illuminating a coated thin layer of sample **1**; and (d) The same LED illuminating a coated thin layer of 0.1 mol % Mn doped **1.**[10]

The chromaticity coordinates range from 0.31 to 0.34 (x) and 0.35 to 0.40 (y) for 2D-[Cd_2S_2(*ba*)] based structures and Mn doped samples, which are within the white region of the International Commission on Illumination (CIE) 1931 color space chromaticity diagram as shown in Figure 5.10.

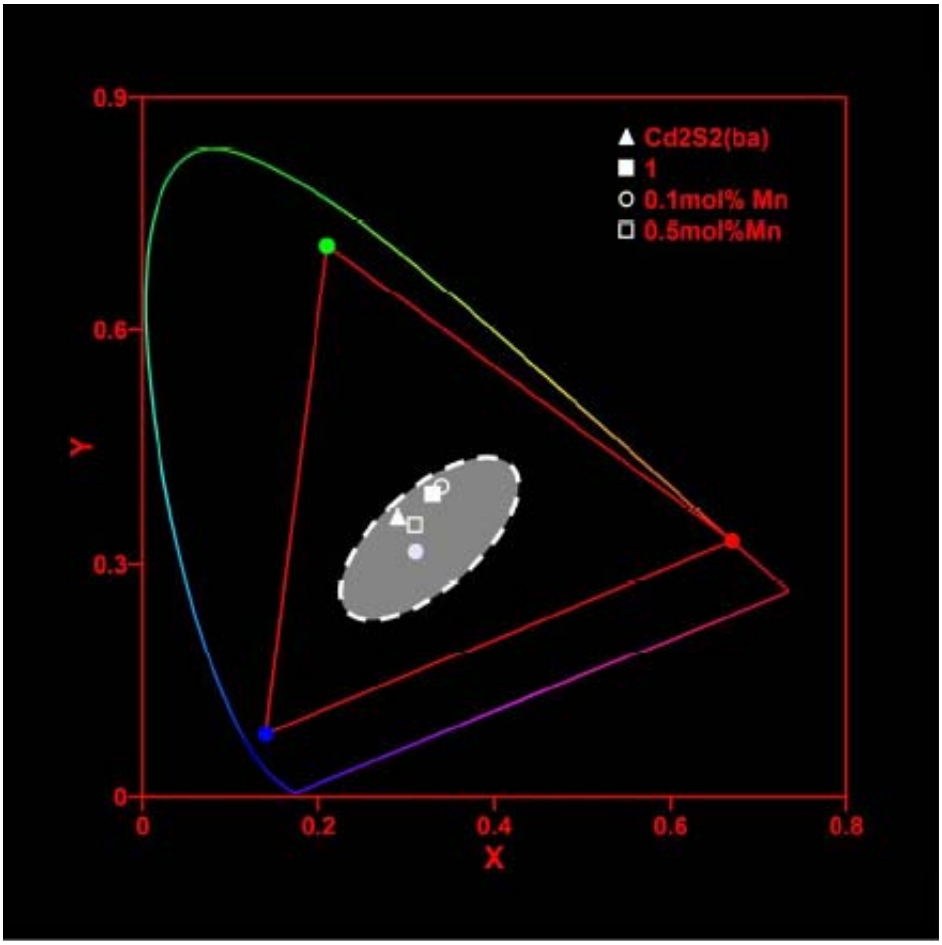

Figure 5.10 CIE coordinates calculated using the software GoCIE obtained from http://www.geocities.com/krjustin/gocie.html. **1**: (0.33, 0.39); 0.1 mol% Mn @ **1**: (0.34, 0.40); 0.5 mol% Mn @ **1**: (0.31,0.35). The white dot indicates CIE coordinate (0.33, 0.33), and the grey area, white light region.

Figure 5.11 represents the integrated intensity of PL emission varies as a function of the length of organic monoamines in the double-layer 2D-[$Cd_2S_2(L)$] series. The PL emission intensity is enhanced with an increase in L (*L* = propylamine (*pa*), butylmaine (*ba*), pentylamine (*pta)*, and haxylamine (*ha*))

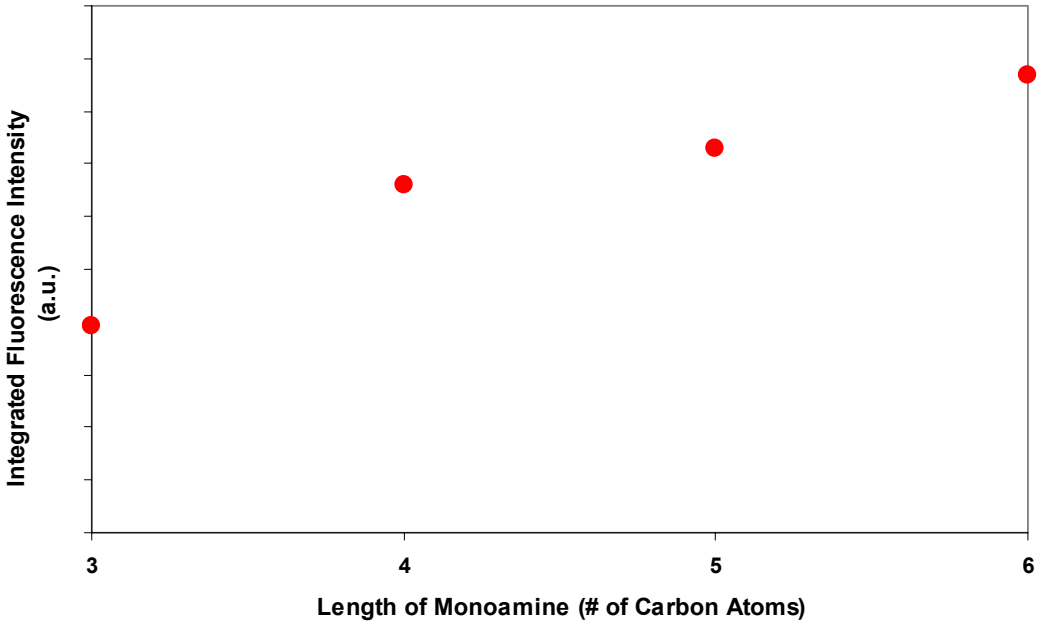

Figure 5.11 The integrated PL intensity as a function of the amine length *L* (*L* = *pa*, *ba*, *pta* and *ha*, λ_{ex} = 360 nm).

The Quantum yield of these hybrid materials dispersed in DMSO was measured using trans-stilbene as a reference dye dissolved in hexane following a similar procedure reported previously for CdSe. The quantum yield was calculated using a comparative method by following the formula.[13]

$$\Phi_x = \Phi_{ST} \times (Grad_x \times \eta_x^2 / Grad_{ST} \times \eta_{ST}^2)$$

where subscripts "*X*" and "ST" refer sample and standard, respectively. Grad is the slope of integrated fluorescence intensity *vs* absorbance; and η is the refractive indices of the solvents used (see Appendix II).

It turns out 4~5% quantum yield was obtained from the hybrid materials compared to 2-3 % and 1-5% for the CdSe[7] and ZnSe[14] nanocrystals, respectively.

In order to estimate the particle size of our hybrid materials, suspended resultant solution from centrifugation as described in experimental section was spin coated with 2500 rpm for 30 sec onto silicon substrate. Figure 5.12 shows a particle image of hybrid materials by SEM. Particle size was roughly 200nm based on the SEM image.

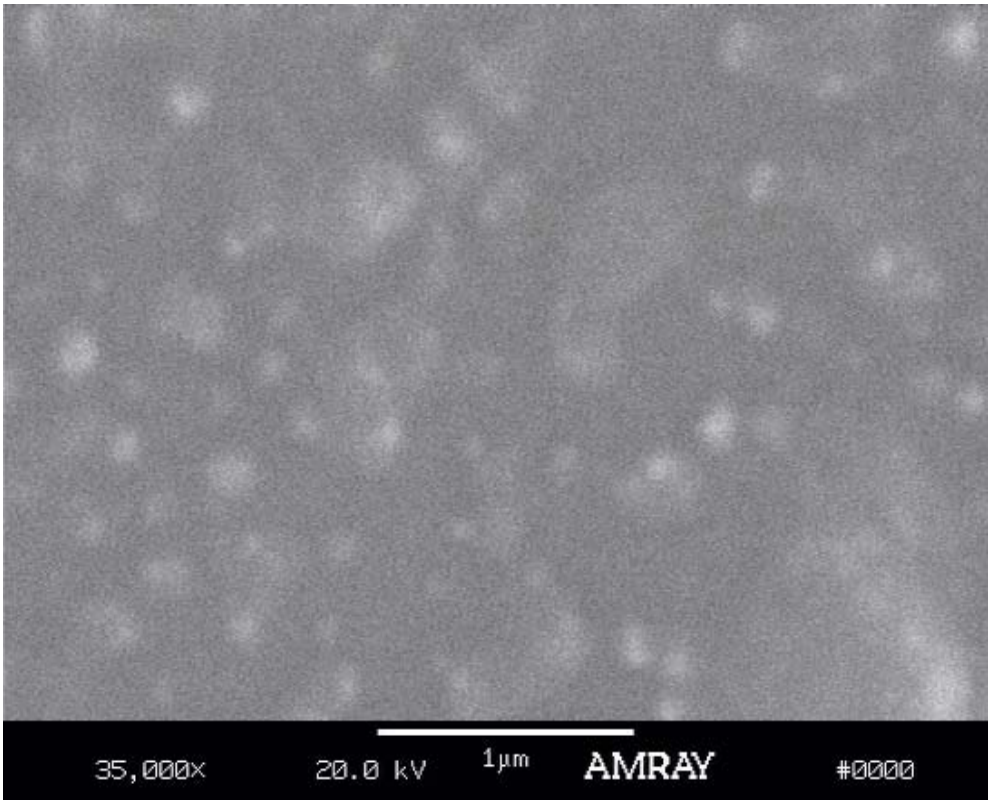

Figure 5.12 SEM image of spin coated hybrid materials onto Si substrate.

Dynamic light scattering (DLS) theory is a well established technique for measuring particle size over the size range from a few nanometers to a few microns. Our

hybrid sample was prepared by diluting suspended resultant solution from centrifugation. 1 drop of the suspended hybrid solution was added into 2mL DMSO in fluorescence cell. Figure 5.13 shows size distribution of diluted hybrid materials. The effective diameter of hybrid particles was ~178nm, confirming well matched with SEM image analysis.

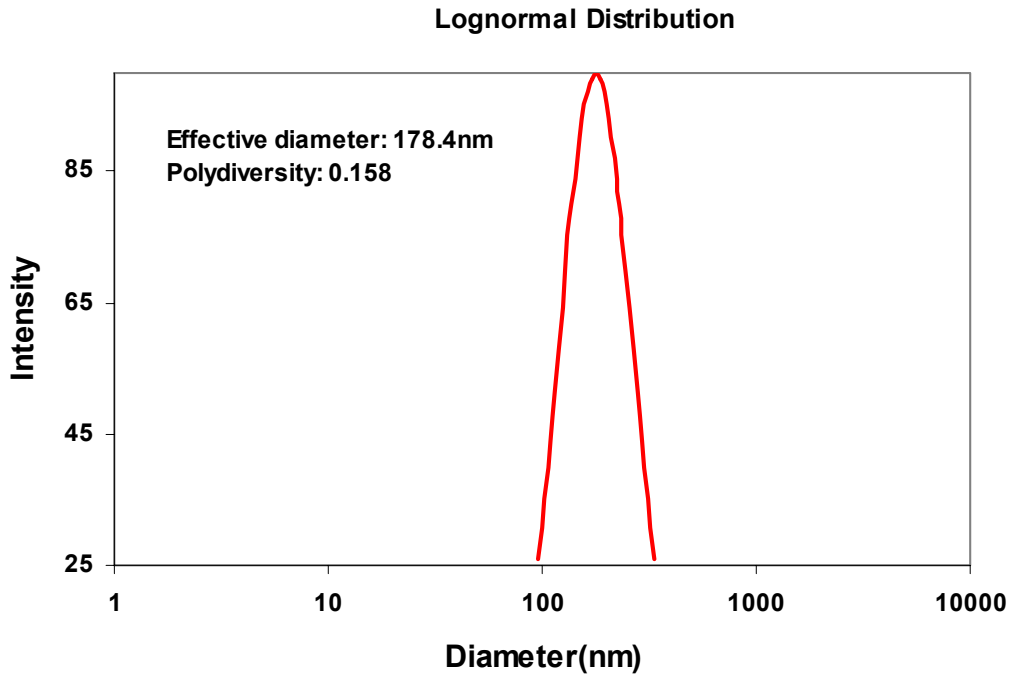

Figure 5.13 The size distribution of hybrid materials by DLS(Model: ZetaPALS 90 Plus Particle Size Analyzer from Brookhaven Instruments)

5.2.2 2D- [Cd_2Se_2(*ba*)] based double layer structures

Since the double layered 2D-[Cd_2S_2(*ba*)] based structure exhibits relatively high energy band gap (E_g, ~2.9eV) (Figure 5.14), it is important to modify the compound in order to decrease E_g so that higher conductivity may be achieved. As a step toward such an improvement, we further studied the Cd_2Se_2(*ba*) based hybrid semiconductors that not only emit white light with lower E_g than that of 2D-Cd_2S_2(*ba*), but also attain electrical conductivity that is necessary for efficient light-emitting diodes.

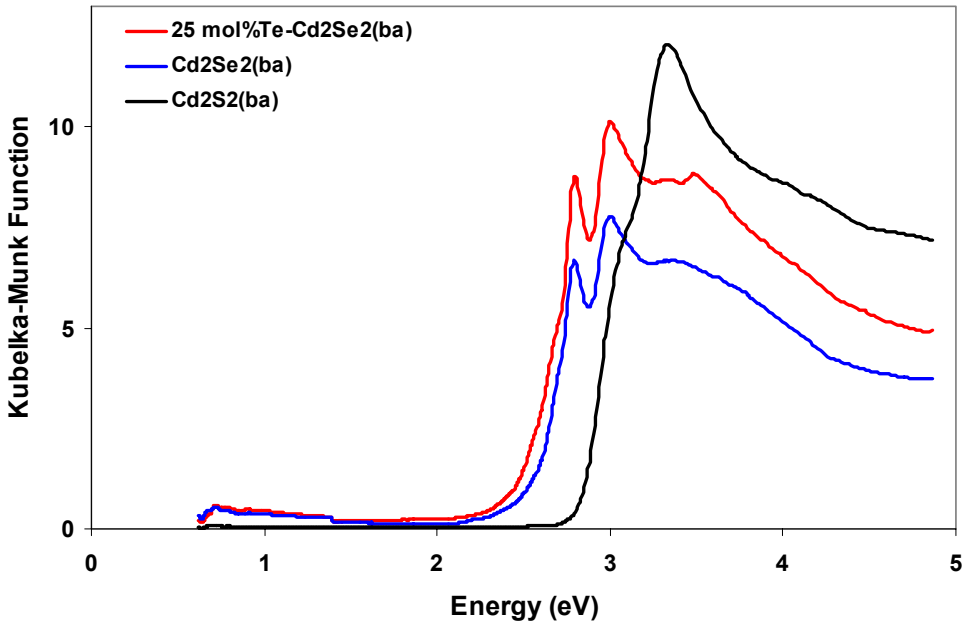

Figure 5.14 Room temperature optical absorption spectra of double-layer 2D-[Cd_2S_2(*ba*)], double-layer 2D-[Cd2Se2(*ba*)], and 2D-[Cd_2Se_2(*ba*)] with substitution of 25mol%Te (*ba* = butylamine) structure. The latter two show a red shift of ~0.3 eV and 0.5 eV compared to Cd_2S_2(*ba*), respectively.

A conventional method for tuning the physical properties of semiconductor is to change their compositions by doping or substituting elements. For example, Nag and Sarma described a way to tune the emission spectra of white light emitting CdS NCs by doping Mn^{2+} at certain concentrations, with increasing orange/red emissions stemming from Mn^{2+} 3d states, thus producing balanced white regions.[15] Substituting Te into CdSe NCs produced photoluminescence spectra with asymmetrically broadened and red shifted peaks compared to CdSe NCs.[16] It is also well known that the E_g can be tuned by doping elements, for example, doping of Te in CdSe and doping of Se in ZnS to decrease band gaps.[17]

As we described earlier, the same phenomena were observed in inorganic-organic hybrid semiconductor materials with Se substitution in Cd_2S_2(*ba*). Figure 5.14 clearly shows that the E_g of [Cd_2Se_2(*ba*)] decreases with substitution of 25 mol% Te, by about 0.2eV from the parent structure.

The Powder X-ray diffraction (PXRD) patterns in Figure 5.15 indicate the peak shifting of a 25 mol% Te substituted sample with respect to that of the CdSe based host lattice, as seen in inset. The lower angle of the (200) peak position is consistent with the increase in the Te concentration and, consequently, the increase in the unit cell dimensions since Te is larger then Se.

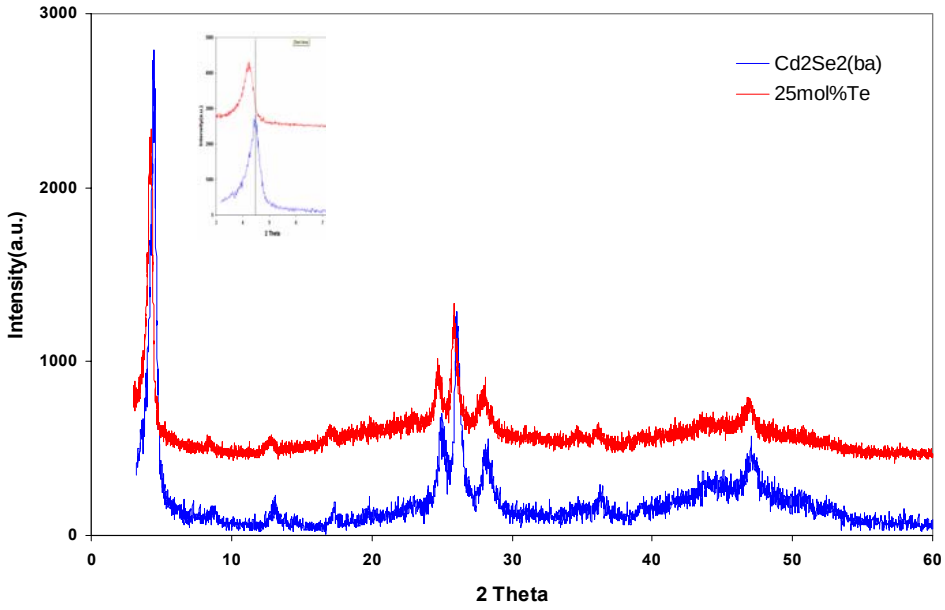

Figure 5.15 PXRD patterns of [Cd_2Se_2(*ba*)] and 25mol%Te- [Cd_2Se_2(*ba*)]. Inset shows enlargement of first peaks

The emission properties of the parent structure have been tuned to target white light emission by substituting Te. As seen in Figure 5.16, broad band edge emission was observed at 463nm (2.67eV) covering the blue/green color region. This broadened spectrum could be attributed to the similar reasons described for the Se@Cd_2S_2(*ba*) system as a result of very high surface-to-volume ratio.[10]

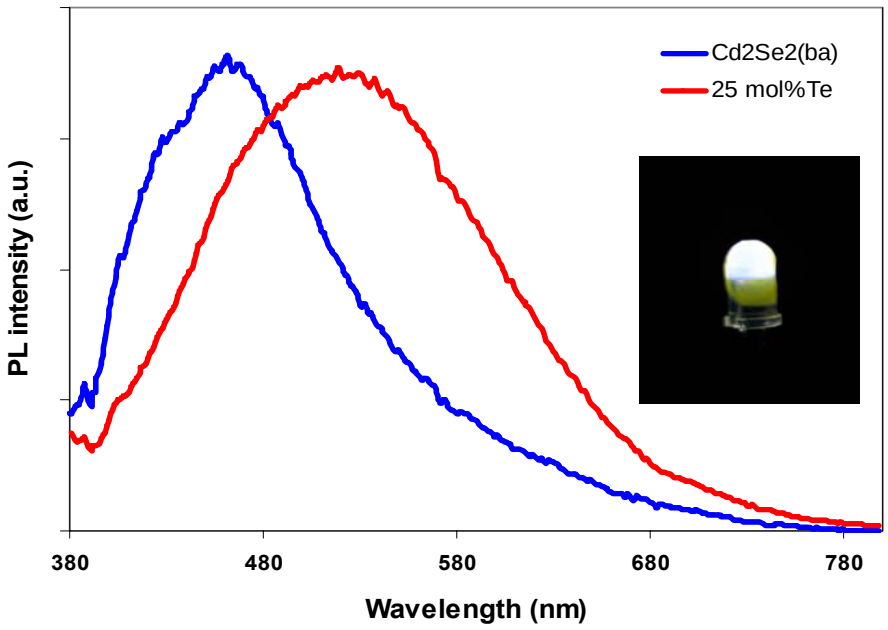

Figure 5.16 Room temperature photoluminescence of the double-layer 2D-[Cd_2Se_2(*ba*)] (blue, λ_{ex} = 360 nm) and 25 mol%Te- [Cd_2Se_2(*ba*)] structure (red, λ_{ex} = 360 nm) (Inset: demonstration on white light emission of thin coated 25 mol%Te-[Cd_2Se_2(*ba*)] onto a commercial UV-LED)

By adding 25 mol% Te, a broader emission spectrum was produced that spanned over visible range. A similar phenomenon was observed for CdSe:Te NCs.[15] The long wavelength present can be attributed to the radiative recombination from trap states created by Te atoms in a CdSe lattice. A decrease of the decay rates for the increasing Te content is observed based on time resolved photoluminescence decays. This indicates that the recombination of charge carriers trapped by Te impurities occurs at a slower time scale than that without Te doping. The inset of Figure 5.16 shows the white light emission from a thin coating of 25mol%Te-[Cd_2Se_2(*ba*)] on a commercial UV-LED.

Another interesting feature is that the hybrid semiconductors can be excited over a wide range of excitation wavelength, from 300nm to 380nm without compromising the chromaticity, as shown in Figure 5.17. Figure 5.18 shows the excitation and emission spectra of a 25mol%Te-[Cd_2Se_2(*ba*)] sample.

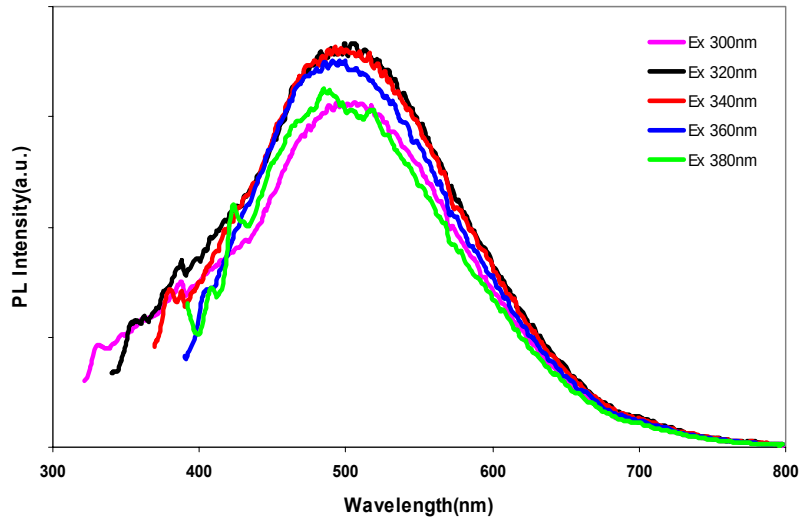

Figure 5.17 PL emission spectra of [Cd_2Se_2(*ba*)]:25mol%Te with various excitation wavelengths from 300nm to 380nm.

.

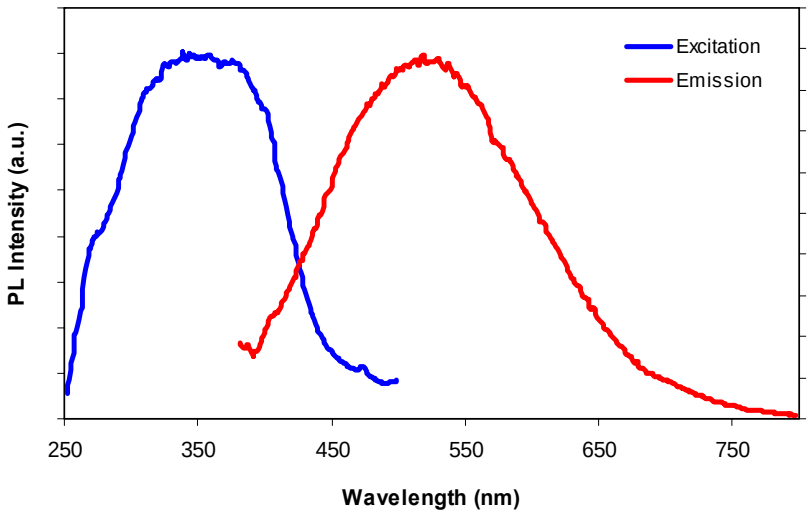

Figure 5.18 Blue: Excitation spectrum of [Cd_2Se_2(*ba*)]:25mol%Te Red: Emission spectrum of [Cd_2Se_2(*ba*)]:25mol%Te

Room temperature PL spectra of [Cd_2Se_2(*ba*)] and [Cd_2Se_2(*ba*)]:25%Te have chromaticity coordinates of (0.21,0.24) corresponding to the blue color region and (0.29,0.35) falling well within the white region, respectively, based on the International Commission on Illumination (CIE) 1931 color space chromaticity diagram as shown in Figure 5.19.

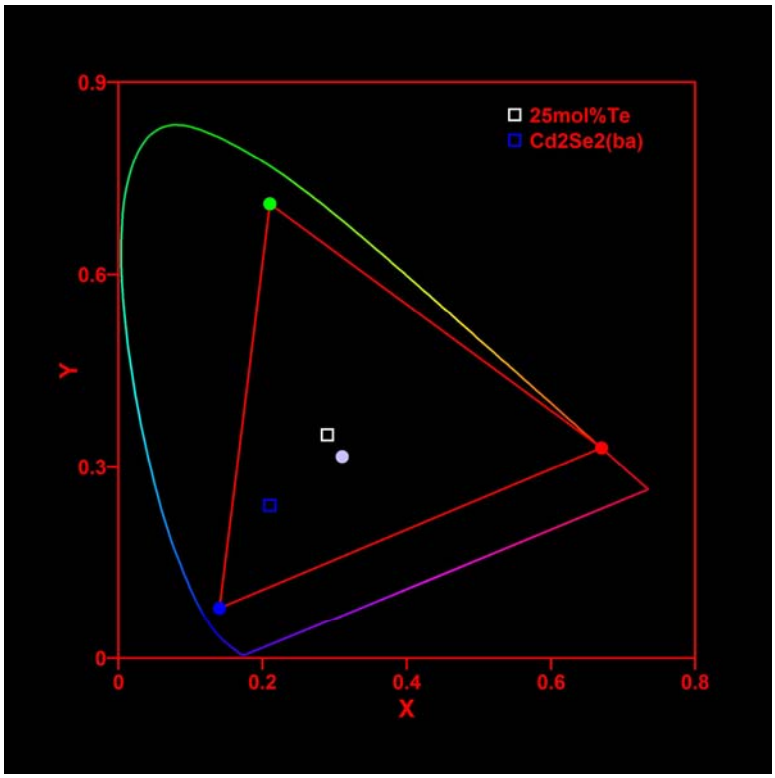

Figure 5.19 CIE coordinates calculated using the software GoCIE obtained from http://www.geocities.com/krjustin/gocie.html. Cd_2Se_2(*ba*): (0.21, 0.24) and 25 mol%Te-[Cd_2Se_2(*ba*)]: (0.29, 0.35). The CIE coordinates for the equi-energy white point (0.33, 0.33) are indicated by a white solid dot.

The fluorescence quantum yield was obtained by using comparative method similar to the procedure reported previously as well as absolute quantum yield method and is on the order of 3-4%. Absolute quantum yield was achieved by following formula using an integrating sphere that collects all the emission (2π steradians) from a sample.[18]

$\Phi_{PL} = [E_{in}(\lambda) – (1-\alpha)\ E_{out}(\lambda)]/\ X_{empty}(\lambda)\alpha$

with $\alpha = [X_{out}(\lambda)-X_{in}(\lambda)]/\ X_{out}(\lambda)$

where $E_{in}(\lambda)$ and $E_{out}(\lambda)$ are integrated emission and $X_{empty}(\lambda)$ is the integrated excitation profile with empty sphere and α is the absorbance. $X_{in}(\lambda)$ is the integrated excitation when the sample lies directly in the excitation path and $X_{out}(\lambda)$ is the integrated excitation when the excitation light first hits the sphere wall.

This method allows the determination of the photoluminescence quantum yield by an absolute measurement.

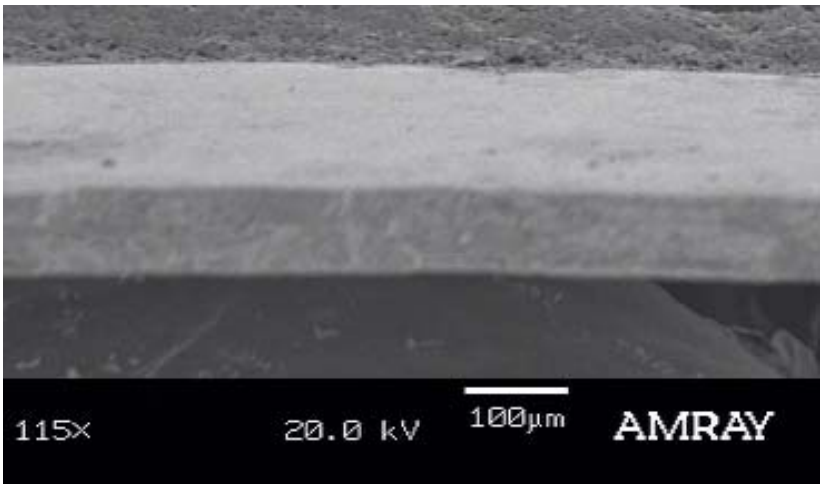

Figure 5.20 A SEM image of the thin pellet 25 mol% Te-[Cd_2Se_2(*ba*)]

Electrical transport measurements have been conducted on free standing thin pellet (~4mm x 5mm in size) of 25mol%-[Cd_2Se_2(*ba*)]. The thickness of the hybrid pellet was found to be ~85μm as shown in Figure 5.20. The I-V curve shown in Figure 5.21 represents the current-voltage characteristic of the thin pellet showing a linear ohmic behavior. The resistance is estimated to be about 10 GΩ, which is comparable to the values of a nanosystem of CdSe where the measured current is typically of the order of nA or pA.[19,20] The room-temperature resistivity of the hybrid material is about 30 GΩ•cm using a thickness of ~85μm taken from SEM cross sectional imaging. Since the conductivity of the pellet of the hybrid material highly depends on the surface properties of the particles and inter-particle contact resistance, the thin pellet of bulk hybrid semiconductor exhibits much higher resistivity than that of a single NC.

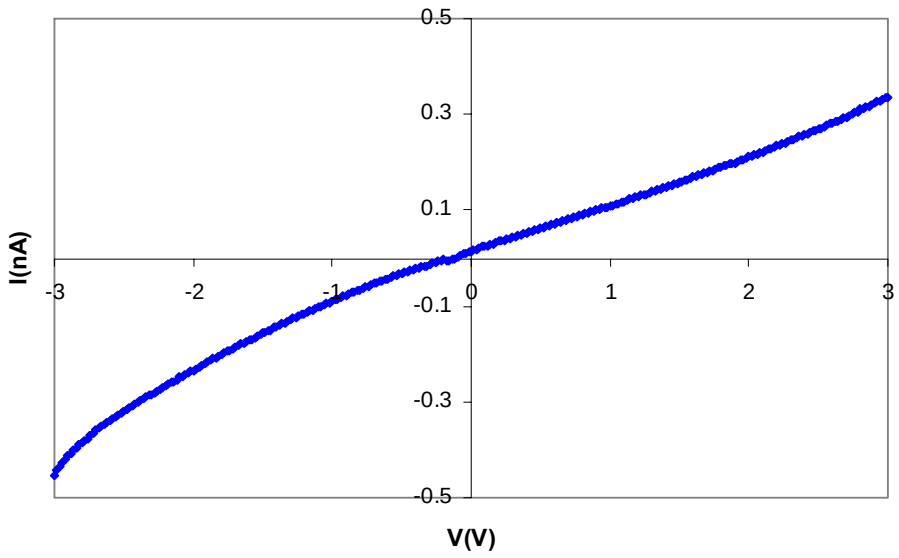

Figure 5.21 *I-V* curve of the thin pellet 25mol%Te-[Cd_2Se_2(*ba*)] at room temperature (inset: SEM image of the pellet)

5.4 Conclusion

We have developed the first semiconductor bulk materials that are capable of generating direct white light. We have shown that the structures and light-emitting properties of these hybrid materials can be systematically tuned. Additionally, they possess distinctive advantages of having extended structures in comparing with NCs, which are necessary for high carrier conductivity and mobility required in light emitting diodes. More importantly, the bulk semiconductor material in thin pellet form showed measurable electrical conductivity. While the conductivity is low, it was obtained on a pellet sample without any modification. Significant improvement can be anticipated with modification of the composition and structures, and improvement in sample preparation .

5.5 References

1. (a) *Energy Sa*V*ings Potential of Solid State Lighting in General Illumination Applications*; Navigant Consulting Inc.: Washington, DC, 2003, http:// lighting.sandia.gov/. (b) Bergh, A.; Craford, G.; Duggal, A.; Haitz, R. *Phys. Today* **2001**, *54*, 42

2. (a)*The Promise of Solid State Lighting for General Illumination*; Optoelectronics Industry Development Association: Washington, DC, 2001. (b) http://www.netl.doe.gov/ssl/

3. (a) Uchida, Y.; Taguchi, T. *Opt. Energy* **2005**, *44*, 124003-1.(b) Taguchi, T. *Proc. SPIE* **2004**, *5530*, 7. (c) Taguchi, T. *J. Light Visual En*V*iron.* **2003**, *27*, 131.

4. Xiao, J. P.; Xie, Y.; Tang, R.; Luo, W. *Inorg. Chem.* **2003**, *42*, 107

5. http://www.netl.doe.gov/ssl/usingLeds/general_illumination_color_white.htm

6. (a) Mueller, A. H.; Petruska, M. A.; Achermann, M.; Werder, D. J.; Akhadov, E. A.; Koleske, D. D.; Hoffbauer, M. A.; Klimov, V. I. *Nano Lett.* **2005**, *5*, 1039. (b) Yang, W.-J.; Luo, L.; Chen, T.-M.; Wang, N.-S. *Chem. Mater.* **2005**, *17*, 3883.

7. Bowers, M. J.; McBride, J. R.; Rosenthal, S. J. *J. Am. Chem. Soc.* **2005**, *127*, 15378.

8. (a) Huang, X.-Y.; Li, J.; Fu, H. *J. Am. Chem. Soc.* **2000**, *122*, 8789. (b) Huang, X.; Li, J.; Zhang, Y.; Mascarenhas, A. *J. Am. Chem. Soc*. **2003,** *125*, 7049-7055. (c) Huang, X.Y.; Heulings IV, H. R.; Le, V.; Li, J. *Chem. Mater*. **2001**, *13*, 3754. (d) Heulings IV, H. R.; Huang, X.-Y.; Li, J.; Yuen, T.; Lin, C. L. *Nano Lett.*, **2001**, *10*, 521. (e) Huang, X.-Y.; Li, J. Mater. Res. Soc. Symp. Proc., **2002**, *728*, 17-22. (f) Fluegel, B.; Zhang, Y.; Mascarenhas, A.; Huang, X.-Y.; Li, J. *Phys*. *Rev*. *B,* **2004**, *70(20)*, 205308/1-205308/5. (g) Zhang, Y.; Dalpian, G. M.; Fluegel, B., Wei, S.-H.; Mascarenhas, A.; Huang, X.-Y.; Li, J.; Wang, L.-W. *Phys. Rev. Lett.*, **2006**, *96*, 026405. (h) Moon, C.-Y.; Dalpian, G. M.; Zhang, Y.; Wei, S. -H.; Huang, X. -Y.; Li, J. *Chem. Mater.*, **2006**, *18*, 2805. (i)Huang, X. and Li, J. *J. Am. Chem. Soc.* **2007**, *129*, 3157-3162.

9. (a) Murray, C. B.; Kagan, C. R.; Bawendi, M. G. *Science* **1995**, *270*, 1335. (b) Nozik, A. J.; Micic, O. I. *Mater. Res. Soc. Bull.* **1998**, *23*, 24.

10. Ki, W. and Li, J. *J. Am. Chem. Soc.* **2008**, *130*, 8114-8115

11. Underwood, D. F.; Kippeny, T. C.; Rosenthal, S. J. *J. Phys. Chem. B* **2001**, *105*, 436.

12. (a) Norris, D. J.; Yao, N.; Charnock, F. T.; Kennedy, T. A. *Nano Lett.* **2001**, *1*, 3. (b) Yang, H.; Santra, S.; Holloway, P. H. *J. Nanosci. Nanotechnol.* **2005**, *5*,1364. (c) Nag, A.; Sarma, D. D. *J. Phy. Chem. C* **2007**, *111*, 13641. (d) Lu, J.; Wei, S.; Peng, Y.-Y.; Yu, W.-C.; Qian, Y.-T. *J. Phys. Chem. B* **2003**, *107*, 3427. (e) Lu, J.; Wei, S.; Yu, W.-C.; Zhang, H.-B.; Qian, Y.-T. *Chem. Mater.* **2005**, *17*, 1698.

13. Jose, R.; Zhelev, Z.; Bakalova, R.; Baba, Y. and Ishikawa, M. *Appl. Phys. Lett.* **2006,** *89*, 013115.

14. Hines, M. A.; Guyot-Sionnest, P. *J. Phys. Chem. B* **1998**, *102*, 3655.

15 Nag, A. and Sarma, D. D. *J. Phy. Chem. C* **2007**, *111*, 13641

16. Franzl, T.; Muller, J.; Klar, T.; Rogach, A. L.; Feldmann, J.; Talapin, D. V. and Weller. H. *J. Phys. Chem. C* **2007,** *111,* 2974

17. (a) More, P. D.; Shahane, G. S.; Deshmukh, L. P. and Bhosale P. N. *Materials Chemistry and Physics* **2003,** *80,* 48 (b) Wang, M. ;Fei, G. T. ; Zhang, Y. G. ; Kong, M. G. and Zhang L. D. *Adv. Mater.* **2007**, *19*, 4491

18. (a)Porr`es, L.;Holland, A.; P°alsson,L.O.; Monkman, A. P.; Kemp,C.; and Beeby, A. *J. Fluoresc.,***2006***, 16,*267. *(b)* Demas J. N. and Crosby, G. A. *J. Phys. Chem.* **1971**,*75*, 991.

19. Zhang, Z. Y.; Jin, C. H.; Liang, X. L.; Chen, Q. and Peng. L. M. *Appl. Phys. Lett.* **2006,** *88,* 073102.

20. Hegg, M. C. and Lin, L. Y. *IEEE/LEOS International Optical MEMS & Nanophotonics Conference*, Hualien, Taiwan, Aug. 12-16, 2007.

CHAPTER SIX

Film Fabrication of Inorganic-organic Hybrid Semiconductor Materials

6.1 Introduction

Inorganic-organic hybrid materials exhibit very interesting physical and chemical phenomena, and offer a great opportunity for potential applications. Thin film deposition of hybrids, however, has been challenging because of their complex compositions of the inorganic and organic components with very different properties.

Recently, solution based deposition has been employed to obtain continuous and uniform films. For example, perovskite type inorganic-organic hybrid thin films based on metal halide were developed by solution based techniques.[1,2] One of the advantages of these hybrid materials is their high solubility in common solvents which make them promising for applications in electronic devices at ambient temperature. For example, thin films of several phenethylammonium-based tin (II) iodide compounds have been fabricated by spin coating techniques, and yielded saturation-regime mobilities as high as 1.4 cm^2 /Vs.[2]

Another interesting area of hybrid film fabrications is to form composite materials using polymers for electrical and optical applications. Inorganic semiconductors are incorporated into a polymer matrix to fabricate functional hybrid materials, such as photovoltaic solar cells and light emitting diodes.[3-8] For example, Zinc oxide (ZnO) was incorporated into a yellow light emitting polymer, poly(fluoresceinyl terephthalate-*co*-bisphenol A terephthalate, FTBT) to generate white light.[9] It showed higher efficiency compared to the hybrid LED fabricated from the same blue LED and FTBT. An optimum amount of ZnO in FTBT gives rise to the enhancement of quantum yield. The high PL intensity of the hybrid materials was attributed to the "caging effect" of the ZnO shell, which can reduce the self quenching of the FTBT molecules in the core. Zhang and

Heeger[10] also demonstrated pure white light emission was achieved from an InGaN and a single conjugate polymer, such as poly (2,5-bis(cholestanoxy)-1,4-phenylene vinylene) and poly(MEH-PPV-*co*-BuEH-PPV). When the polymers were properly encapsulated, the operating lifetimes of the hybrid LED were comparable to those of commercial blue GaN lamps.

Although our inorganic-organic hybrid semiconductors exhibit very interesting properties, including extremely strong quantum confinement effect and systematic tunability by changing the structure and dimensionality of the inorganic motifs, it has been quite challenging to make hybrid thin films for opto-electronic applications because most hybrid materials synthesized by solvothermal reactions are insoluble in conventional solvents.

Ultrasonication has been widely used in chemical synthesis. The chemical effects of ultrasound arise from acoustic cavitation by creating, enlarging, and collapsing micro-bubbles in a very short time. When the bubble collapse, it creates intense local heating (~5000K), high pressures(~1000atm),very short lifetimes, and heating and cooling rates above 10^{10} K/s. A diverse set of applications of ultrasound to enhance chemical reactivity has been explored with important uses in synthetic materials chemistry.[11]

Our strategy is to employ ultrasonic irradiation on the final products to break large pieces into micro- or submicro-sized particles. These hybrid particles then were imbedded into a conducting polymer, such as polyaniline. Polyaniline, a conjugated polymer, is one of attractive candidates for electronic device applications, because of the tunable electrical properties, chemical stability, and PL enhancement effect.[12]

This composite was spin coated onto SiO_2/Si substrate and the mixture was gently annealed at low temperature. Schematic synthetic procedures are depicted in Scheme 6.1. Blending polyaniline with hybrid particles could generate uniform films via simple solution based film process to study electroluminescence.

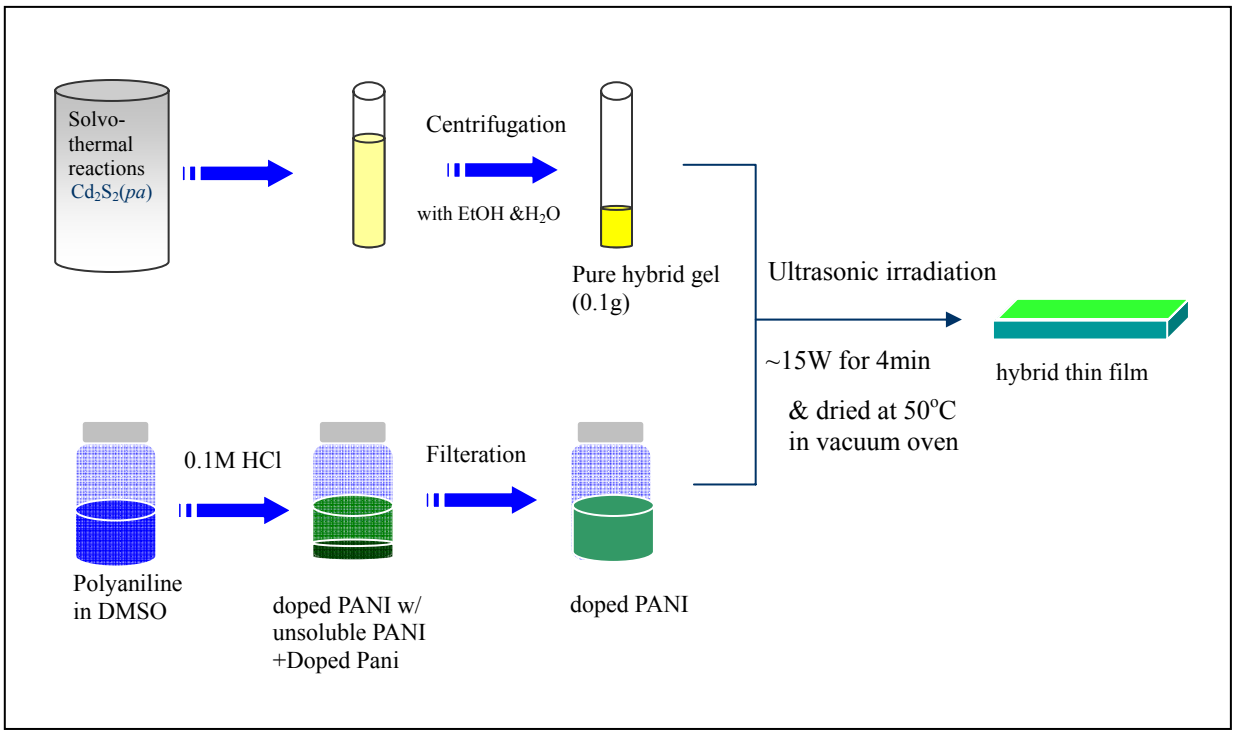

Scheme 6.1 Schematic diagram showing preparation of composite hybrid thin films using polymer.

6.2 Experimental

6.2.1 Fabrication of 1D- ZnTe(*pda*) thin films

Colorless plate-like crystals of 1D-ZnTe(*pda*) were obtained by solvothermal reactions of $ZnCl_2$ and Te in a solvent mixture composed of hydrazine and diaminoprophene (*pda*).[13] . In order to prepare films, 0.1g of 1D-ZnTe(pda) crystals were dissolved in 5mL N_2H_4 and stirred for 7min. Then 1mL pda was added with constant stirring for 15h. Color change was observed from dark violet to light pink. This solution was then deposited onto a clean glass by drop casting and dired at 50 ^oC for 3h in a vacuum oven.

6.2.2 Fabrication of Double layered 2D-[Cd_2S_2(*pa*)] thin films by ultrasonications

Double layered 2D-[Cd_2S_2(*pa*)] (*pa* = prophylamine) was prepared from a solvothermal reaction of $CdCl_2$ (0.366g, 2mmol), S (0.032g, 1mmol), and *pa* (10mL) in an acid digestion bomb at 80 ^oC for 3 days.[14] 140.6mg of [Cd_2S_2(*pa*)] was added into 20mL vial with 10mL dichloromethane (CH_2Cl_2). After the solution was sonicated with ~20W for ~20min under controlling temperature around 30 ^oC, suspended particles were then deposited onto indium tin oxide (ITO) and silicon substrates by spin casting with 2000 rpm for 30 sec with a multi-step procedure to make a thick film, followed by drying at 45 ^oC for 30min.

6.2.3 Composite films of 2D-[Cd_2S_2(*pa*)] with a conducting polymer

To prepare "gel-like" 2D-[Cd_2S_2(*pa*)] hybrid materials, the compound was washed with distilled water and 95% ethanol using centrifugation for 5 times and centrifuged with DMSO to remove excess *pa*. Doped polyaniline was prepared from 13.5 mg of polyaniline (emeraldine base form, M_w=100,000), 9mL of DMSO, and 2mL of 0.1M HCl. The solution was stirred for 40min and filtered by using a 0.2μm syringe filter to remove excess polyaniline.

6.3 Results and discussion

6.3.1 1D- ZnTe(*pda*) thin films by soluble precursors using organic solvents

Most of the hybrid materials we have developed via solvothermal reactions are not soluble in conventional organic solvents. There are very few examples of soluble hybrid materials. Mitzi reported two $ZnTe(N_2H_4)_2$ hybrid structures that were soluble in hydrazine (N_2H_4) and were used to fabricate ZnTe thin films via thermal decomposition.[15] We have found that 1D-ZnTe(*pda*) can also be dissolved in N_2H_4.

Our first trial was to dissolve 1D-ZnTe(*pda*) in hydrazine and propyldiamine (*pda*). Upon dissolving in hydrazine, the original structure can't be recovered without adding *pda* (see 6.2.1). After dissolving the hybrid, it was deposited onto a silicon wafer by drop casting. After deposition, the structure of the hybrid was restored to the original structure. This was confirmed by both PXRD analysis and optical absorption data as shown in Figure 6.1.

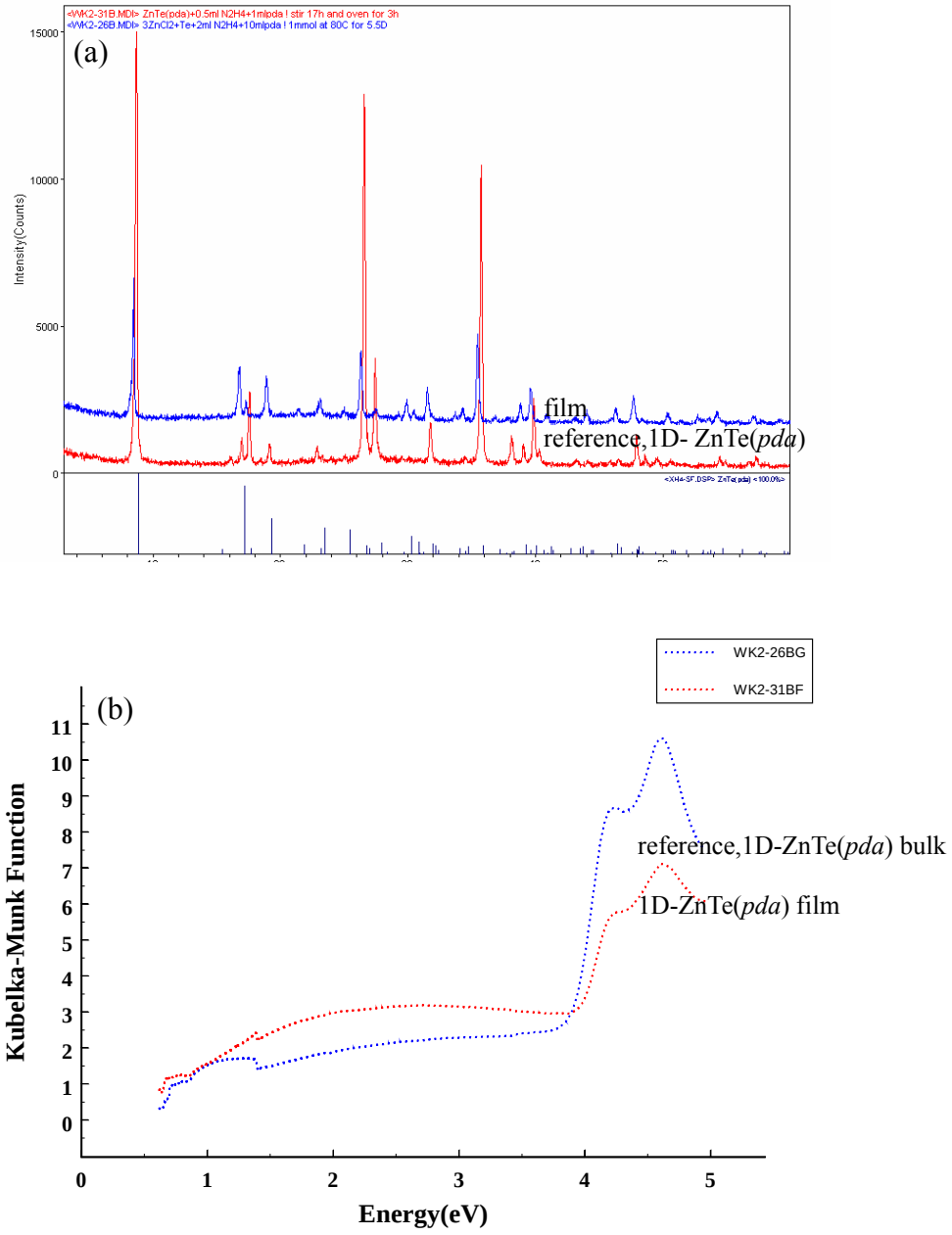

Figure 6.1 PXRD patterns (a) and diffuse reflectance data (b) after film depositions compared to original structure

Figure 6.2 shows a SEM image of drop casted film on a Si substrate. The grain size was found to be around 10μm and be elliptical in shape.

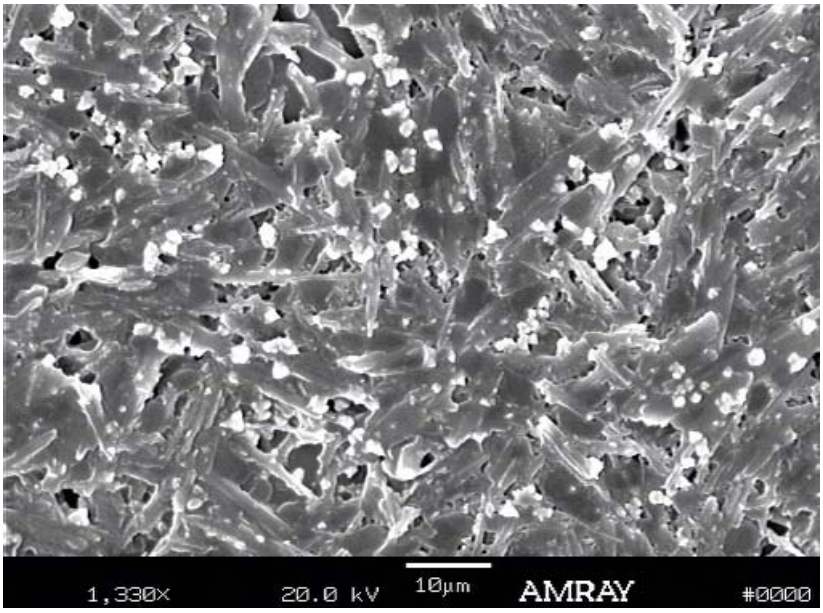

Figure 6.2 A surface image of 1D-ZnTe(*pda*) film by SEM

6.3.2 2D-[Cd_2S_2(*pa*)] thin film fabrications by employing ultrasonications

The large pieces of the hybrid sample were broken into micro- and nano sized particles in a volatile solvent, CH_2Cl_2 by ultrasonic radiation treatment. This solution was then spin coated onto SiO_2/Si substrate, and the solvent was evaporated during spin coating to generate films.

X-ray diffraction and optical absorption were carried out before and after ultrasonic irradiations. As seen in Figure 6.3 ultrasonic irradiation did not affect the

structure of the hybrid films, since no major changes were observed in the PXRD patterns and their adsorption edge. SEM images of the hybrid films show that the surface is mainly covered with micron particles, as shown in Figure 6.4(a). Figure 6.4(b) represents the PL spectrum of the powder 2D-Cd_2S_2(*p*a) sample, which shows broad emission that covers the entire visible region and also weak band gap emission at 410nm (~3eV). The current-voltage curve of the Cd_2S_2(*pa*) film were performed. However, because of the non-uniform film surface, inconsistent I-V curve were obtained. Therefore, the surface of the film remains to be improved.

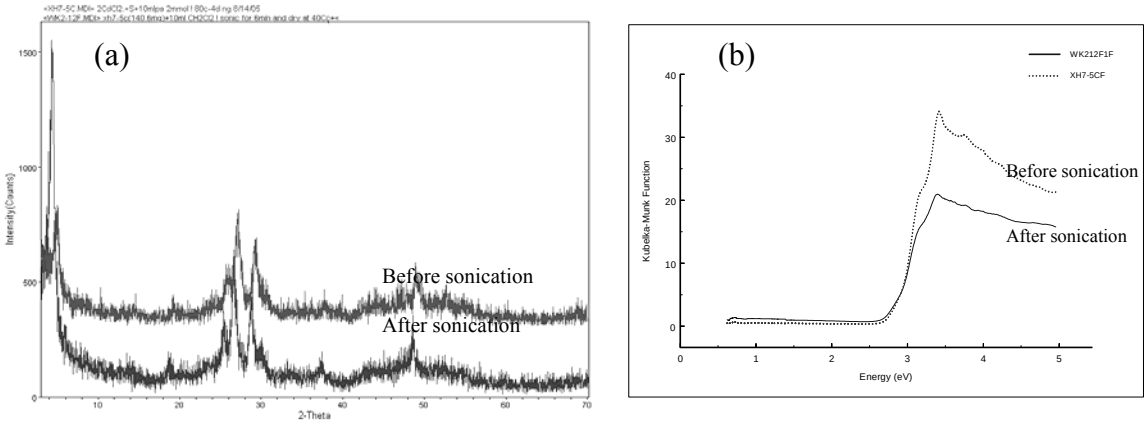

Figure 6.3 PXRD patterns (a) and optical absorption spectra (b) of samples before and after ultrasonic irradiation.

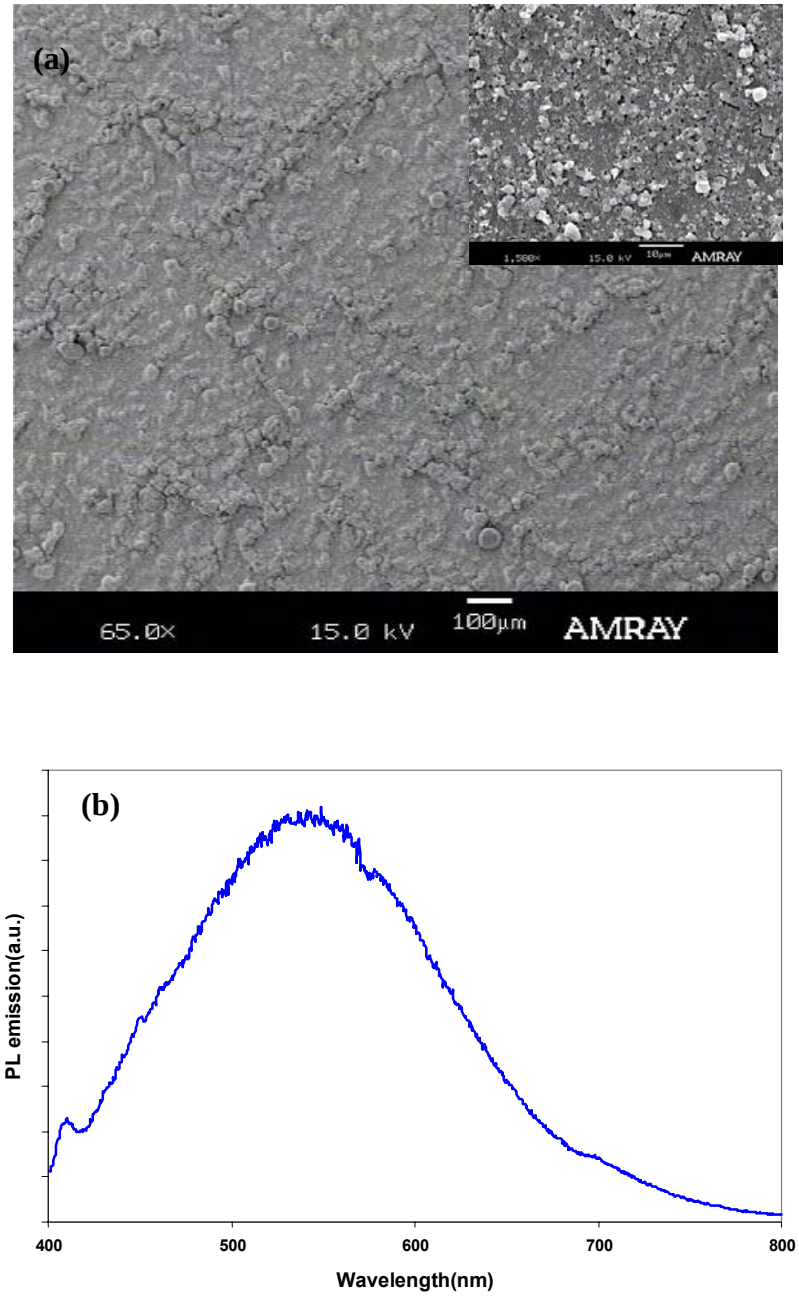

Figure 6.4 (a) The film morphology of [Cd_2S_2(*pa*)] by SEM; (b) PL spectrum of 2D-[Cd_2S_2(*pa*)] taken from powder sample at room temperature.

6.3.2 2D-Cd_2S_2(*pa*) film fabrication with using a conjugate polymer, polyaniline

The emeraldine form of polyaniline, often referred to as emeraldine base (EB), is either neutral or only partially reduced or oxidized.[16] The conducting state of PANI, emeraldine salt, can be achieved by the protonation of an acid, such as HCl from 50% oxidized emeraldine base.[16]

Figure 6.5 shows the UV-Vis absorption spectra of undoped polyaniline and doped polyaniline (PANI) with 0.1M HCl in DMSO solvent. The characteristic peaks of doped polyaniline appear at ~325~360nm, ~400~430, and ~780~826nm, which were attributed to π-π*, polaron- π*, and π-polaron transitions, respectively.[17,18] This result shows that PANI is in the doped state. In our study, 0.1M HCl was used to dope polyaniline because higher concentration of HCl dissolved the Cd_2S_2(*pa*) hybrid structure, thus destroying the original structures.

Recently, polyaniline was synthesized by an ultrasonic irradiation synthesis method and showed that the crystalinity of polyaniline is much higher than that synthesized by the traditional stirring method, thus conductivity is much improved by introducing sonications.[18] Using ultrasonic irradiation on polyaniline could improve conductivity as well as facilitate the dispersion of inorganic-organic semiconductor materials into the polymer matrix.

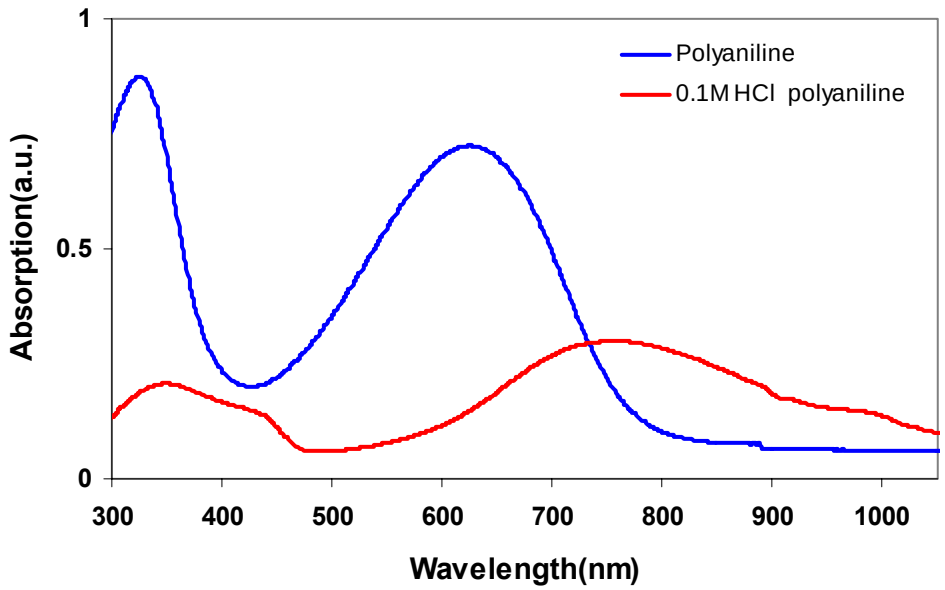

Figure 6.5 UV-vis absorption spectra of doped and undoped PANI

The doped Cd_2S_2(*pa*)/polyaniline composite films were fabricated by uniformly mixing 0.107g of Cd_2S_2(*pa*) and 3mL of doped polyaniline via ultrasonic irradiation (~10W) for 1min in air in DMSO. The solution was then drop casted onto clean glass and thermally grown oxidized silicon substrates (d_{SiO2} = 4000 Å) and dried at 40 ^{o}C for 8h in a vacuum oven. Figure 6.4 shows the diffraction patterns of pure Cd_2S_2(*pa*) and the composite films on glass. The structure of hybrid materials in polyaniline was retained within the polymer matrix after ultrasonic irradiations, even though peaks were slightly shifted as shown in Figure 6.4(a).

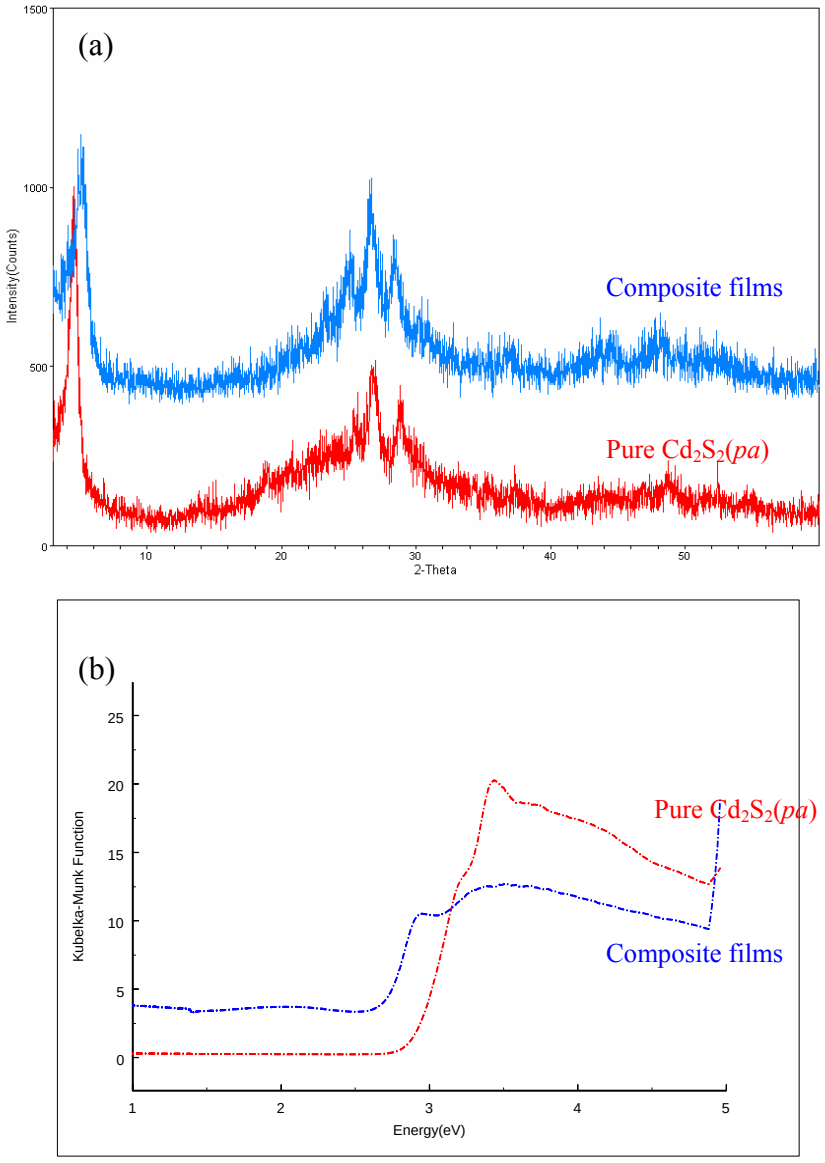

Figure 6.6 (a) X-ray diffraction data of the composite material (b) Diffuse reflectance data of composite material

Figure 6.6 (b) shows that the absorption edge of the composite films were found to be ~2.4eV which is red shifted from pure Cd_2S_2(*pa*) of 2.8eV due to the influence of the doped polyaniline on the hybrid material.

A uniform surface with few scattered hybrid particles is observed in the sample by

SEM image as shown in Figure 6.7(a). The thickness of the composite film was measured to be 625nm by cross sectional SEM imaging (Figure 6.7(b))

.

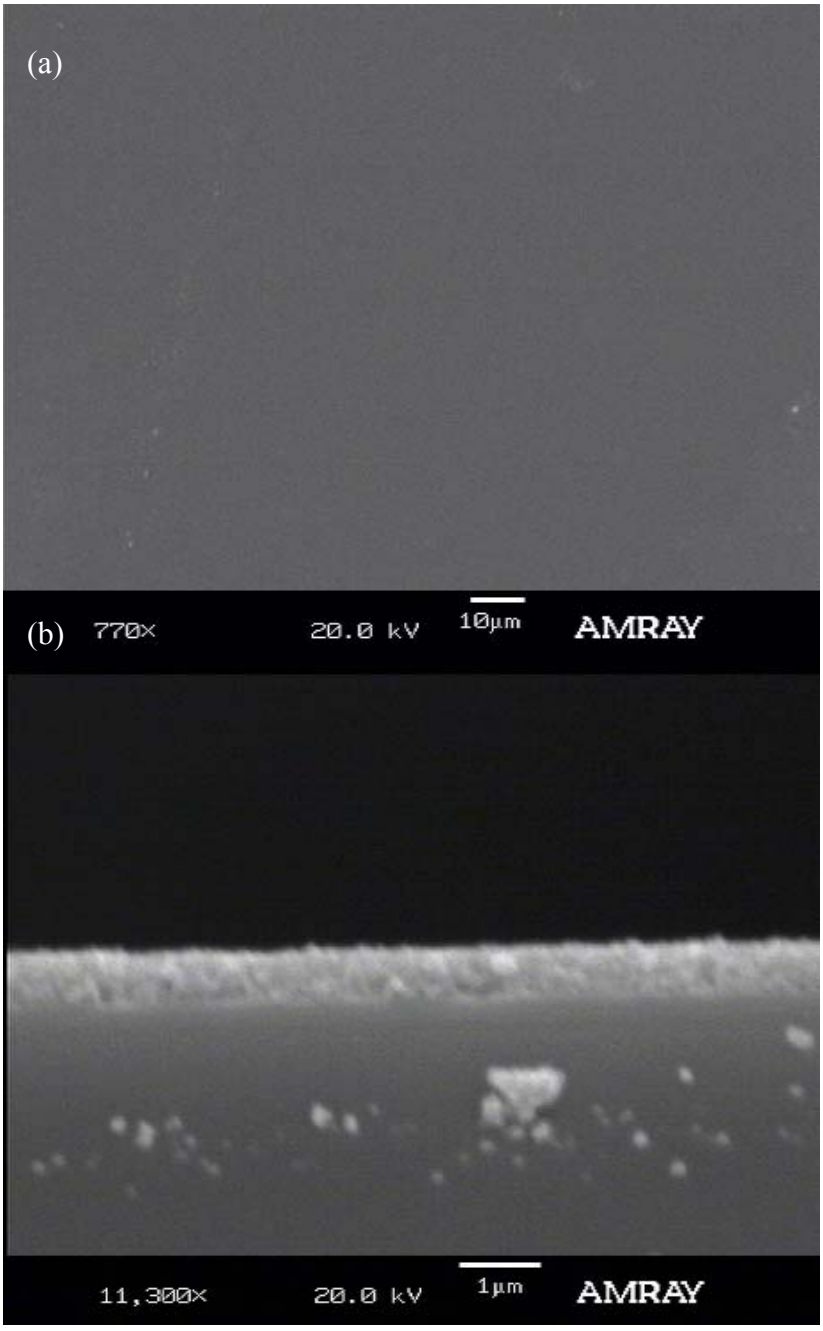

Figure 6.7 (a) a surface image by SEM (b) a cross-sectional SEM image of the composite films

The surface morphology of the films was also characterized by AFM as shown in Figure 6.8. Roughness was 36.85nm. Some of particles are seen in the surface, but most hybrid particles are imbedded into the polymer matrix as seen in the cross sectional SEM images.

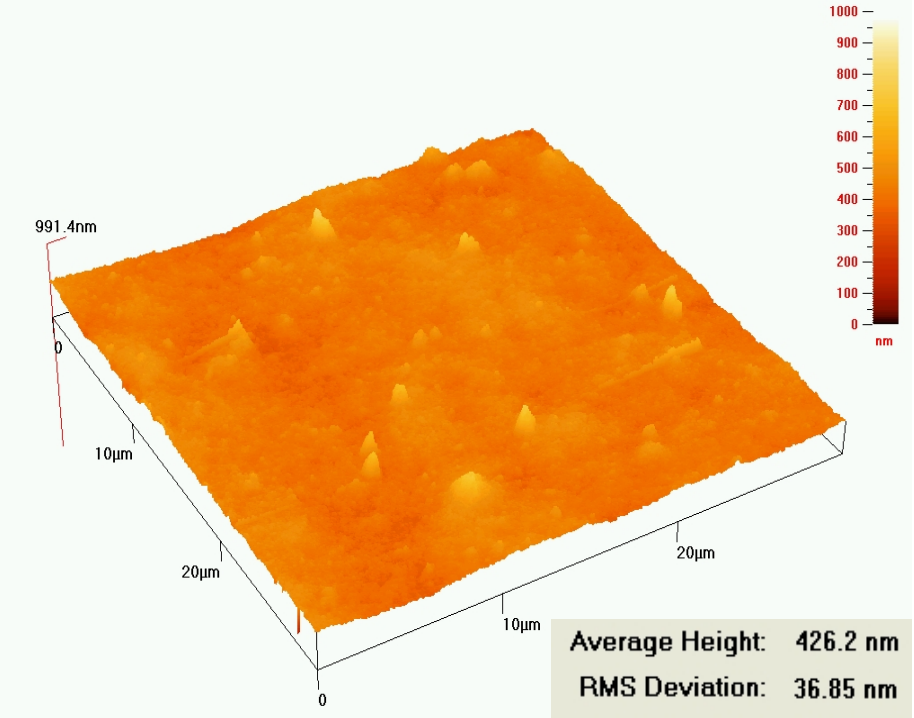

Figure 6.8 A surface morphology of the composite film by AFM.

The room temperature conductivity was measured on thin films using a four probe conductivity measurement. The results are represented in Table 1. Increasing the concentration of hybrid material (with respect to PANI) results in an increase in the resistivity. This is due to the fact that polyaniline has higher conductivity than the hybrid material under study. This same trend has been observed elsewhere.[4,5,7]

Table 6.1 Electrical conductivity of the composite film samples

	Sheet resistance(Ω)	Conductivity(S/cm)
Doped PANI	~0.64MΩ	~0.1
42wt% (hybrid/PANI)	~2.8MΩ	~$6x10^{-3}$
84wt%(hybrid/PANI)	~4.3MΩ	~$3x\ 10^{-3}$

Photoluminescence studies of the composite film were performed as shown in Figure 6.9. A band emission peak was found to be 410nm (~3.0eV). The calculated chromaticity coordinates for the composite film is (0.28, 0.36), well within the white region of the 1931 CIE diagram as seen in an inset of Figure 6.9.

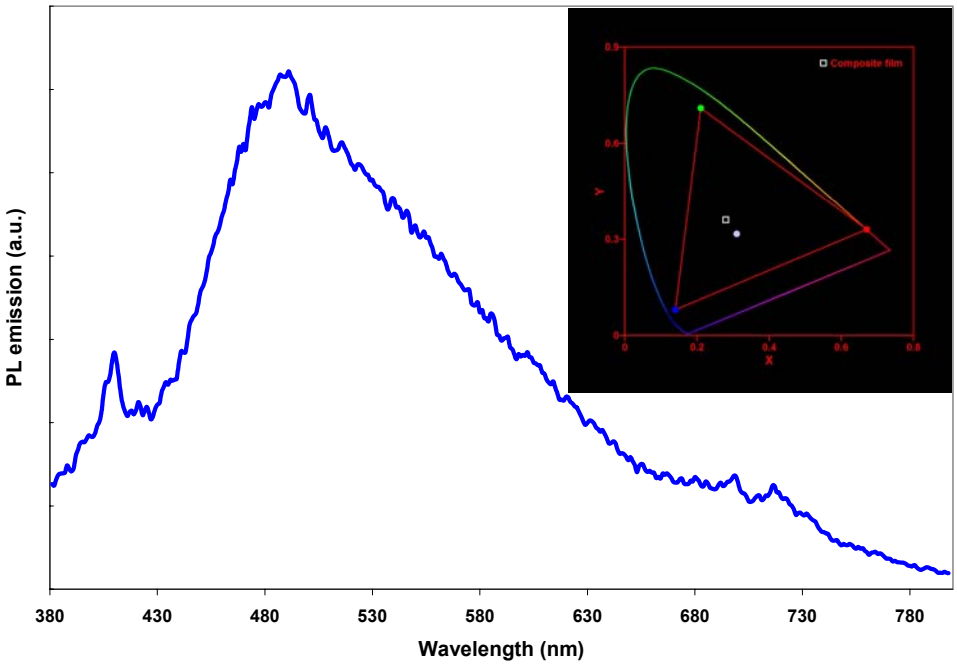

Figure 6.9 PL spectra of the composite film, Cd_2S_2(*pa*)/PANI (λ_{ex}: 360 nm) (Inset shows CIE diagram of the composite film)

6.4 Conclusions

We have attempted in making films of inorganic-organic hybrid semiconductors by two different routes: hydrazinium based depositions and ultrasonic irradiation assisted depositions. The latter of which was enhanced by blending a conducting polymer. In terms of surface morphologies, such as uniformity and roughness, hybrid/polyaniline composites processed by ultrasonic irradiation offer more uniform and smooth films. New synthesis procedures to make “gel-like” inorganic-organic semiconductors were useful for making a material that could better integrate into the conducting polymer. Ultrasonic irradiations also help to break the samples into micron or submicron sized particles and lead to more uniform blending. Our data also show that resistivity of the hybrid/conducting polymer blend increases as the concentration of hybrid was increased.

6.5 References

1. Mitzi, D. B.; Dimitrakopoulos C. D. and Kosbar, L. L. *Chem. Mater.*, **2001**, *13*, 3728.

2. Era M. and Oka, S. *Thin Solid Films*, **2000**, *376*, 232.

3. Hide, P.; Kozodoy, P.; DenBaars, S. P. and Heeger, A. J. *Appl. Phys. Lett.* **1997**, *70*, 2664.

4. Mosquedaa, Y.; Pe´rez-Cappea, E.; Aranab, J.; Longob, E.; Riesb, A.; Cilenseb, M.; Nascentec, P.A.P.; Arandad, P. and Ruiz-Hitzkyd, E. *J. Solid State Chem.* **2006,** *179*, 308–314.

5. Xia, H. and Wang, Q. *Chem. Mater.* **2002,** *14,* 2158-2165.

6. Mcdonald, S. A.; Konstantatosi, G.; Zhang, S.; Cyr. P. W.; Klemi, E.J.D.; Levina, L. and Sargenti, E. *Nature Mater.* **2005**, *4*, 138.

7. Khanna, P. K.; Kulkarni, M.V.; Singh, N.; Lonkar, S,P.; Subbarao, V.V.V.S. and Kasi Viswanath, A. *Mater. Chem. Phys*. **2006**, *95*, 24-28.

8. Riede, A.; Helmstedt, M.; Riede,V.; Zemek, J. and Stejskal, J. *Langmuir* **2000,** *16,* 6240-6244.

9. Uthirakumar, P.; Hong,C.H.; Suh, E. K. and Lee, Y. S. *Chem. Mater.* **2006,** *18,* 4990-4992.

10. Zhang, C.;and Heeger, A. J. *J. Appl. Phys.* **1998**, *84*, 1579.

11. Suslick, K. S. "Sonochemistry and Sonoluminescence" in *Encyclopedia of Physical Science and Technology*, 3rd ed. Academic Press: San Diego, 2001, vol. 17, pp. 363-376.

12. (a) Gaponik, N. P.; Talapin, D. V. and Rogach, A. L. *Phys. Chem.Chem. Phys.* **1999**, *1*, 1787-1789. (b) Vivekchand, S. R. C.; Kam, K. C.; Gundiah, G.; Govindaraj, A.; Cheetham, A. K. and Rao, C. N. R. *J. Mater. Chem.* **2005**, *15*, 4922 – 4927. (c) Xi, Y.; Zhou, J.; Guo, H.; Cai, C. and Lin, Z. *Chem. Phys. Lett*. **2005**,***412***, 60–64 (d) Zheng, Z. X.; Xi, Y. Y.; Dong, P.; Huang, H. G.; Zhou, J. Z.; Wu, L. L. and Lin, Z. H. *Phys. Chem. Commun.* **2002**, *5***,** 63.

13. Huang, X.; Li, J.; Zhang, Y. and Mascarenhas, A. *J. Am. Chem. Soc*. **2003,** *125*, 7049-7055

14. Huang, X.-Y.; Li, J. *J. Am. Chem. Soc.* **2007**, *129*, 3157.

15. Mitzi, D. B. *Inorg. Chem*. **2005**, *44*, 7078-7086.

16. MacDiarmid, A. G. and Epstein, A. J. *Synthetic Metals* **1995**, *69*, 85-92

17. Stafstrom, S.; Breadas, J. L.; Epstein, A. J.; Woo, H.-S.; Tenner, D. B.; Huang, W.-S. and Macdiarmid, A. G. *Phys. Rev. Lett*. **1987**, *59*, 1464.

18. Liu, H.; Hu, B.; Wang, J.Y, and Boughton, R. I. *Macromolecules* **2002**, *35*, 9414-9419.

APPENDICES

Appendices

Appendix I: PXRD patterns and optical absorption spectra of hybrid materials.

Conversion from 2D- ZnSe(*ba*) to 2D-ZnSe(*pa*)

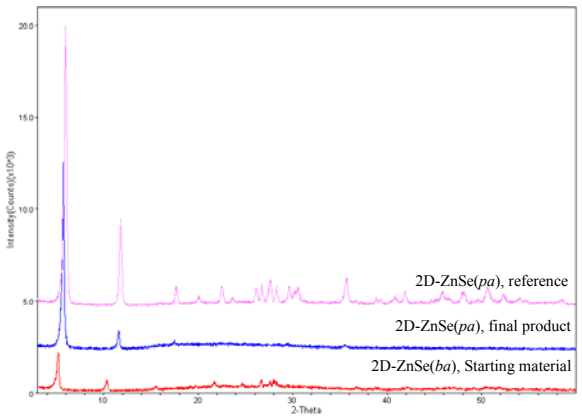

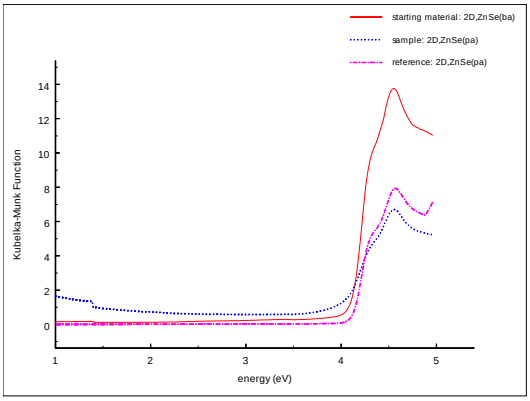

Conversion from 2D- ZnSe(*ba*) to 2D-ZnSe(*ha*)

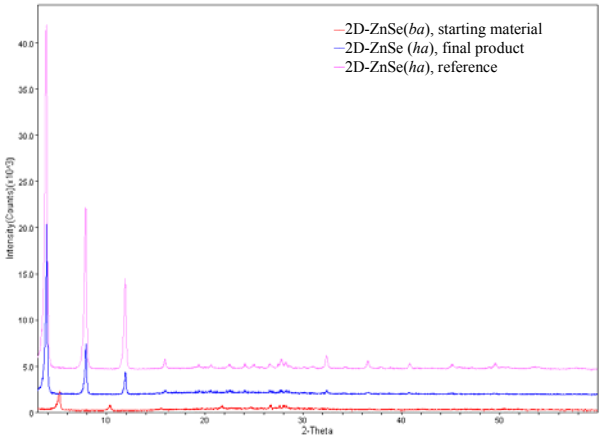

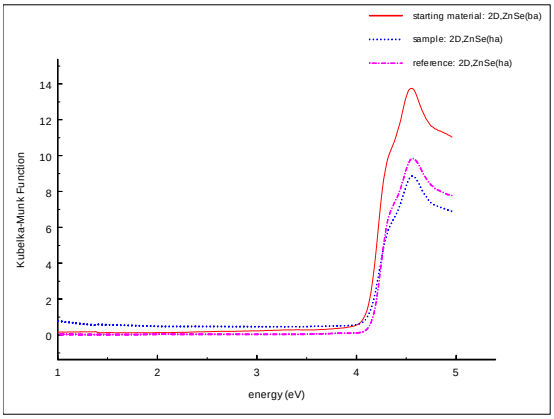

Conversion from 2D- ZnSe(*ba*) to 3D-ZnSe(*pda*)$_{1/2}$

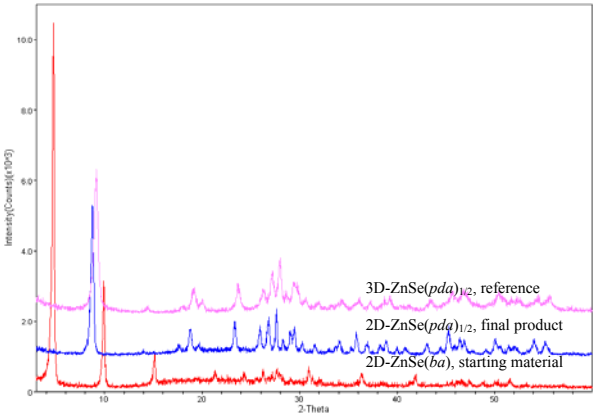

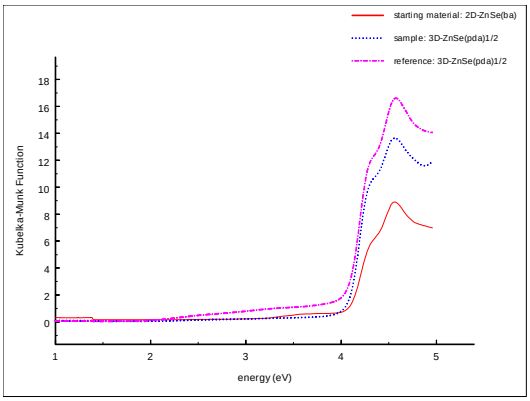

Conversion from 2D-ZnSe(*ba*) to 3D-ZnSe(*bda*)$_{1/2}$

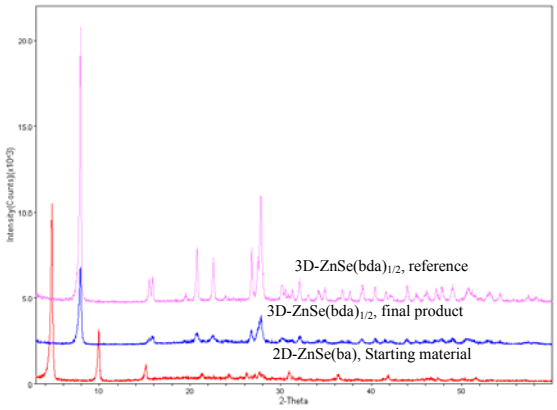

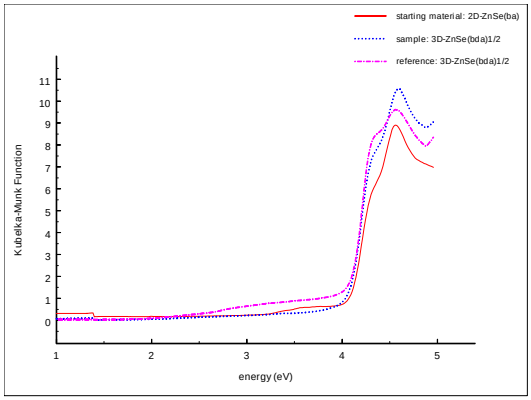

Conversion from 3D-ZnTe(*en*)$_{1/2}$ to 3D-ZnTe(*pda*)$_{1/2}$

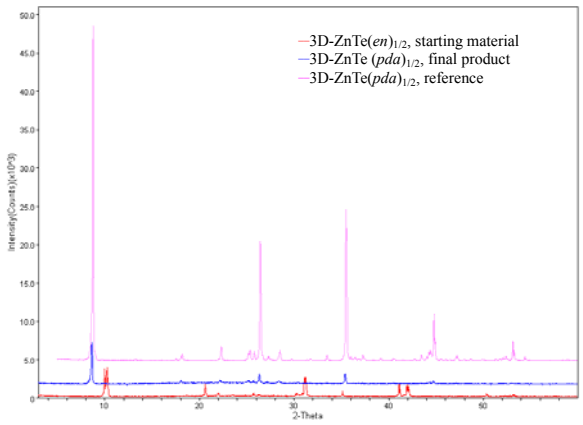

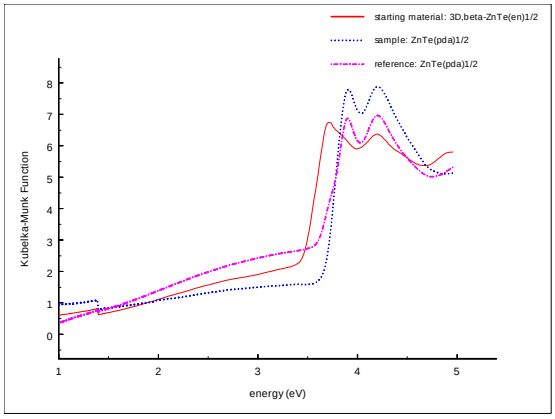

Conversion from 3D-ZnTe(*en*)$_{1/2}$ to 3D-ZnTe(N_2H_4)$_{1/2}$

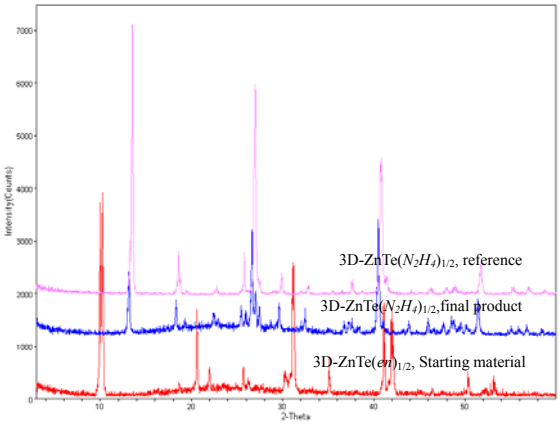

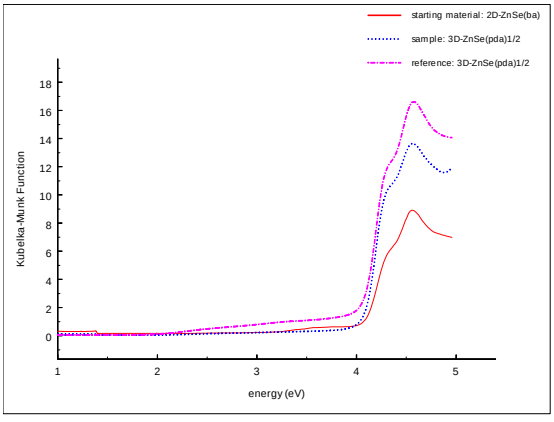

Appendix II: Spin coating techniques

A simplified spin coating process is illustrated in scheme A1.[1]

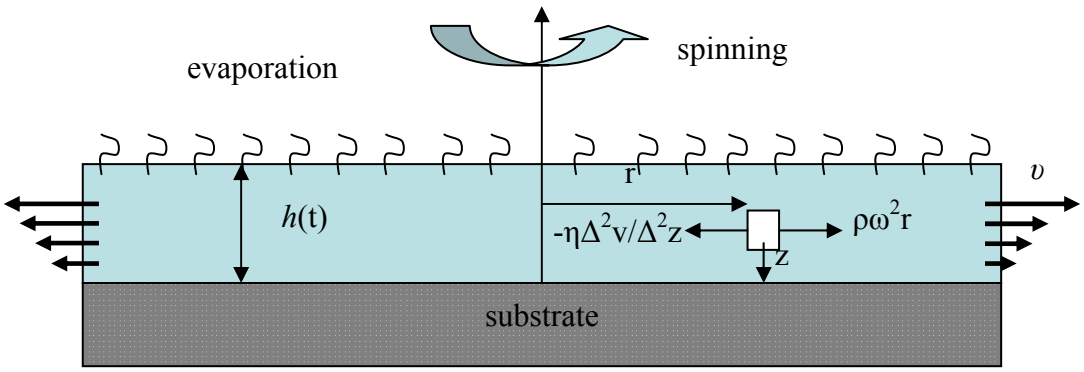

Scheme A1. Schematic diagram showing the spin coating process

The spin coating process can be characterized by several stages:[2] deposition of the coating solution onto the substrate, acceleration of substrate, solution thinning, and solvent evaporation. At the first stage, the coating solution is applied onto the substrate. A substantial excess of coating solution will be required to make final coating with acceptable thickness. In this step, the wettability and viscosity of the solution make an important effect to surface morphology and quality of the films. Poor wettability leads to incomplete coverage and flaws. In general, to avoid defects, surface cleaning and a sub micron sized filter is used before dropping the coating solutions. Substrate cleaning steps are also required to avoid flaws and improve wettability. In our study, thermally grown oxidized silicon substrates were used for film process and cleaned by the piranha method.[3] The substrates were dipped in a solution mixture containing a 4:1 volume ratio of 95% H_2SO_4 and 35% H_2O_2 and heated to 90 °C for 15 min. The cleaned silicon substrates were then rinsed by distilled water and cleaned again in a solution of 30%

NH_4OH, 35% H_2O_2, and H_2O in 1:1:5 (vol) ratio at 70 °C for 10 min and rinsed with distilled water. The second stage is when the substrate spins up to a desired speed. At this point, the solvent become thin enough to be balanced between viscous shear drag between the rotational accelerations. The third stage is characterized by gradual solution thinning. During this stage, the thickness varies depending on surface tension, viscosity, rotation speed, etc. A final stage is a solvent evaporation stage during spinning. Evaporation driven by surface tension effects can create striation defects as shown in Figure A1.[4]

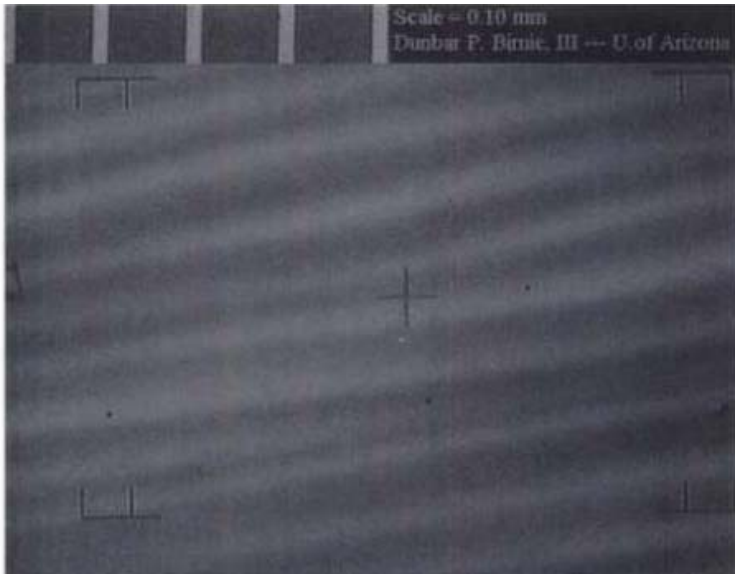

Figure A1 Sol-Gel processed $PbZrTiO_3$ film morphology via spin coating with 3000 rpm

Emslie *et al*. proposed a simple model of the spin-coating process predicting film thickness as a function of a number of physical parameters as follows:[5]

$$h = h_o/[1+ (4\omega^2 h_o^2 t/3\eta)]^{1/2}$$

where h_0 is initial film thickness, ω the spin speed, and η the viscosity.

Figure A1 shows a schematic representation of surface tension force and how to create striations because of capillary forces that become unbalanced during spinning.[6] A convenient way to avoid striation formation is to prevent evaporation during spinning. Because of this, hot-plate heating or furnace baking is required to evaporate the solution after spinning.

In order to improve coverage of thin film, we applied multi-step solution processed deposition, which gives a more continuous film. As shown in Figure A2, a precursor, $(CH_3NH_3)_2MoS_4$ in ethylene glycol solvent, was deposited by spin coating. It shows clearly that with increasing steps, coverage and continuous film are created.

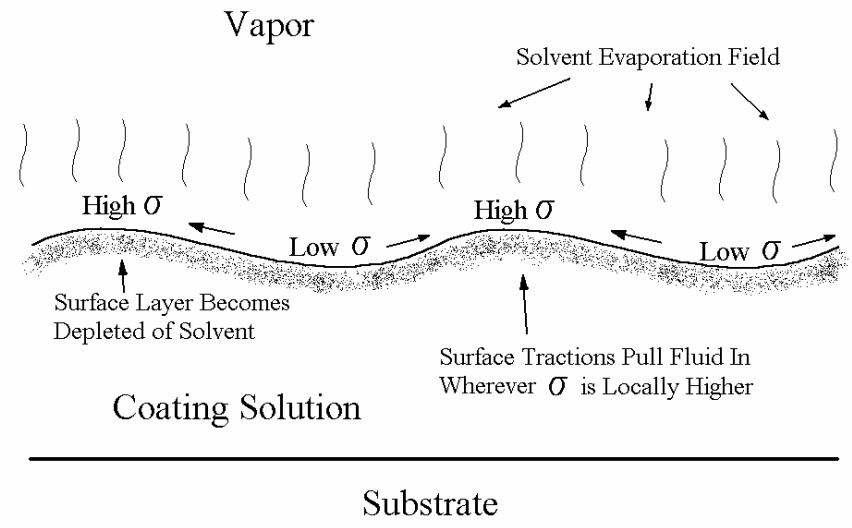

Figure A1. Schematic description of the surface tension forces that can result when solvent is being actively extracted during the spin coating process

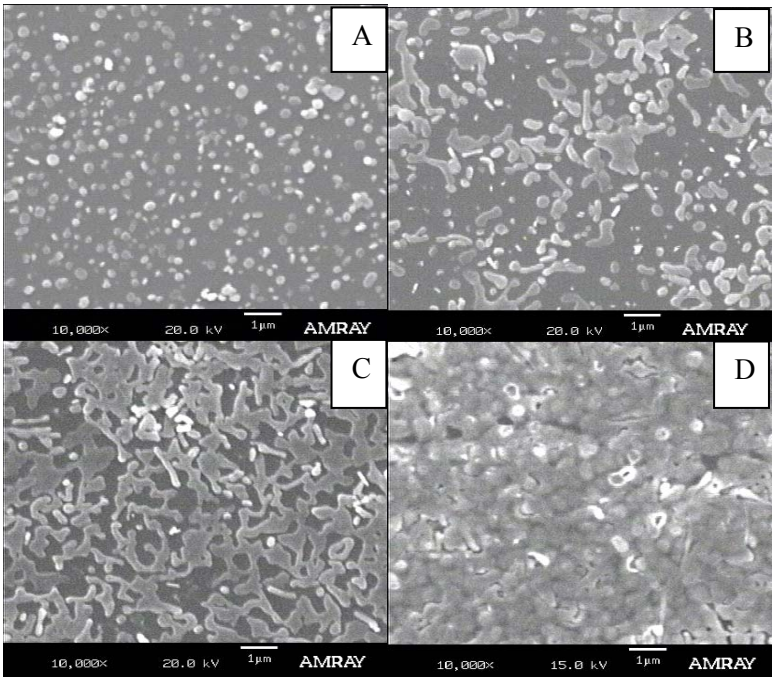

Figure A2. SEM pictures of thin films by spin coating at 3500rpm for 60s with a precursor, $(CH_3NH_3)_2MoS_4$ in ethylene glycol solvent. (A) after one application, (B) after two applications, (C) after three applications, and (D) after five applications.

It is worth noting that particle size is dependent on the concentration of the solution as shown in Figure A3.

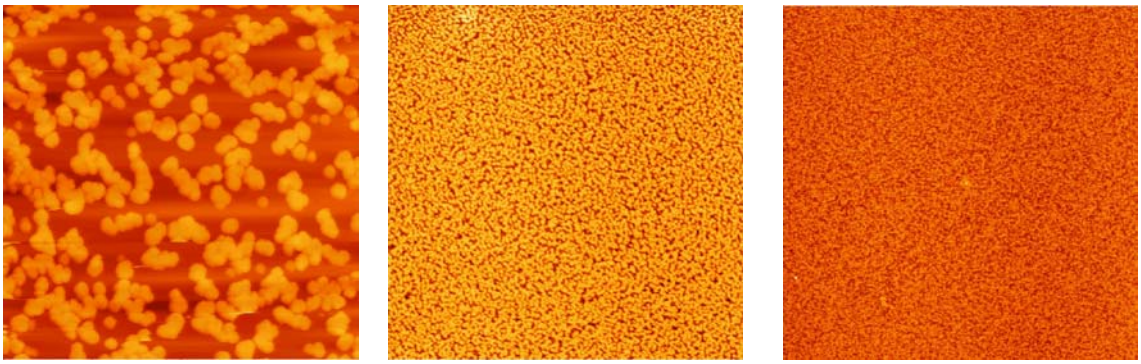

2M CdS 0.5M CdS 0.2M CdS

Figure A3. Morphological changes by different molar ration of CdS in DMSO (For example, 2M CdS is 2mmol of Cd source and S source in 1mL DMSO)

Appendix III: Quantum yield calculations.

Fluorescence quantum yield is defined as the ratio of photons emitted to photons absorbed during a fluorescence process. The process is governed by the radiative (κ_r) and nonradiative (κ_{nr}) rate constants of deactivation by the relationship:[7]

$$\Phi_F = \kappa_r /(\kappa_r + \kappa_{nr})$$

Absolute quantum yield measurement requires special equipment, such as integrating spheres and scattering agents or acinometers to calibrate the system.[8]

One reliable method gives comparative (or relative) quantum yields that uses standard dyes for measuring unknown samples. The fluorescence efficiency of unknown sample can be measured by following equation (1):[9]

$$\Phi_X = \Phi_{ST}\left(\frac{\mathrm{Grad}_X}{\mathrm{Grad}_{ST}}\right)\left(\frac{\eta_X^2}{\eta_{ST}^2}\right)$$

where the subscripts ST and X refer to the standard and to the unknown respectively, Φ is the fluorescence quantum yield, Grad the gradient from the graph of integrated fluorescence intensity verses absorbance, and η the refractive index of the solvent used. Grad_x and Grad_{ST} are produced from PL experiments. Other values are obtined from literature.

The standard samples should be well characterized and suitable for such use. To obtain reliable data, the standard samples should have identical excitation wavelength with the test sample. If possible, similar regions of emission peak should be chosen for the standard and test samples. Table 1 shows typical standard compounds and their literature quantum yield values. In order to minimize re-absorption effect, absorbance in the 10mm fluorescence cuvette should never exceed 0.1 at and above the excitation wavelength,

because it may affect quantum yield value stemming from inner filter effects.[10] Table A1 shows some examples of standard materials and their quantum yield values.

Table A1. Examples of standard materials [11]

Standard Compound	**Solvent**	**Quantum yield**	**Emission range / nm**	**Reference**
Cresyl violet	Methanol	0.54	600-650	*J. Phys. Chem*., 1979, **83**, 696
Rhodamine 101	Ethanol+ 0.01% HCl	1.00	600-650	*J. Phys. Chem*., 1980, **84**, 1871
Quinine sulfate	0.1M H_2SO_4	0.54	400-600	*J. Phys. Chem*., 1961, **65**, 229
Fluorescein	0.1M NaOH	0.79	500-600	*J. Am. Chem. Soc.,* 1945, 1099
Harmane	0.1M H_2SO_4	0.83	400-550	*J. Lumin.*, 1992, **51**, 269-74
2-methylharmane	0.1M H_2SO_4	0.45	400-550	*J. Lumin.*, 1992, **51**, 269-74
Benzene	Cyclohexane	0.05	270-300	*J. Phys. Chem*., 1968, **72**, 325
2-Aminopyridine	0.1M H_2SO_4	0.60	315-480	*J. Phys. Chem*., 1968, **72**, 2680
Anthracene	Ethanol	0.27	360-480	*J. Phys. Chem*., 1961, **65**, 229
Trans-Stilbene	Hexane Ethanol	0.11 0.05		*High Energy Chemistry* **2002**, *36*, 276.
Chlorophyll A	Ether	0.32	600-750	*Trans. Faraday Soc.*, 1957, **53**, 646

An example of sample preparation of double layered 2D-[Cd_2S_2(*ba*)] for quantum yield calculations

Sample Preparation: In general, solid powders are obtained after filtering with ethanol/water via solvothermal reactions. However, to prepare "gel-like" sample, the following procedures have been applied:

The "gel-like" sample was prepared by removing excess *n*-butylamine (*ba*) from the solvothermal reactions and the remaining powders were then transferred into a test tube, followed by adding ethanol/distilled water (8:2 v/v). Using a glass stirring rod, an ethanol/water mixture was vigorously stirred and followed by centrifugation. These steps were applied 5 times (or more) to get rid of remaining *ba*, until a neutral pH by a pH paper was obtained. Finally, DMSO was added into the "gel-like" sample and centrifuged to remove organic solvents. Other solvents can also be used, but in most cases DMSO gives much better "gel-like" sample that is well dispersed. The "gel-like" sample of ~10mg was then suspended in 10mL DMSO and treated by an ultrasonic processor (Model VCX-750, Sonics & Materials, Inc.) with 30W~40W for 30sec. (be aware that depending on the stability of hybrid samples, ultrasonic irradiation may cause damages to their crystal structures, so the power/time of ultrasonic irradiation procedure needs to be well controlled and by checking PXRD patterns and optical absorption spectra. After ultrasonic process, the sample was centrifuged. The diluted resultant solution was used for absorption, PL study, and quantum yield calculations.

Experimental procedures: One must pay special attention when setting up the UV-Vis spectrometer after the instrument is warmed up. In the configuration menu, slit width

(0~5) should be selected. The slit width must be identical for both standard and test samples. This rule is also applied to fluoremeter, when selecting excitation/emission slit, power, and scan control, etc.

1. Run UV-visible spectroscopy for solvent background using solvent that dissolves the standard samples, normally, powder or crystal forms. For example, solvent of quinine sulfate solvent will be 0.1M H_2SO_4 and that of trans-stilbene will be hexane or ethanol. In addtion, dilute stock solutions should be prepared. In general, standards with high quantum yield show very high absorbance. Thus, a very small amount of a standard sample is needed. For example, I've used ~0.9 mg of quinine sulfate in 20mL 0.1M H_2SO_4. In the case of trans-stilbene, ~1.5mg of trans-stilbene was dissolved in 10mL hexane. Those stock solutions give reasonable absorbance values.

2. After establishing baseline with solvents, ~50μL of stock solution of standard sample was added using a micro-pipette into 1cm cuvette in the solvents to record absorbance. Simultaneously, the same amount of the standard sample was added into a fluorescence cuvette to record PL emission. Before one drop standard solution, one must carry out a blank solvent-without standard samples- to calculate net integrated fluorescence intensity. Then, more ~50μL of the standard sample is added into both the absorption and fluorescence cuvette (Make sure that absorbance in the 1cm cuvette should never exceed 0.1 at the excitation wavelength to be used). An example is shown in Figure A4. Both the absorbance and PL emission of *trans*-stilbene in benzene are gradually increased by increasing concentration.

The absorbance data at the excitation wavelength with various concentrations are recorded. In Figure A4, a set of five data points of absorbance and PL emission at five

different concentrations are obtained. Each data point was obtained by increasing the concentration of *trans*-stilbene in benzene into absorption and fluorescence cuvette.

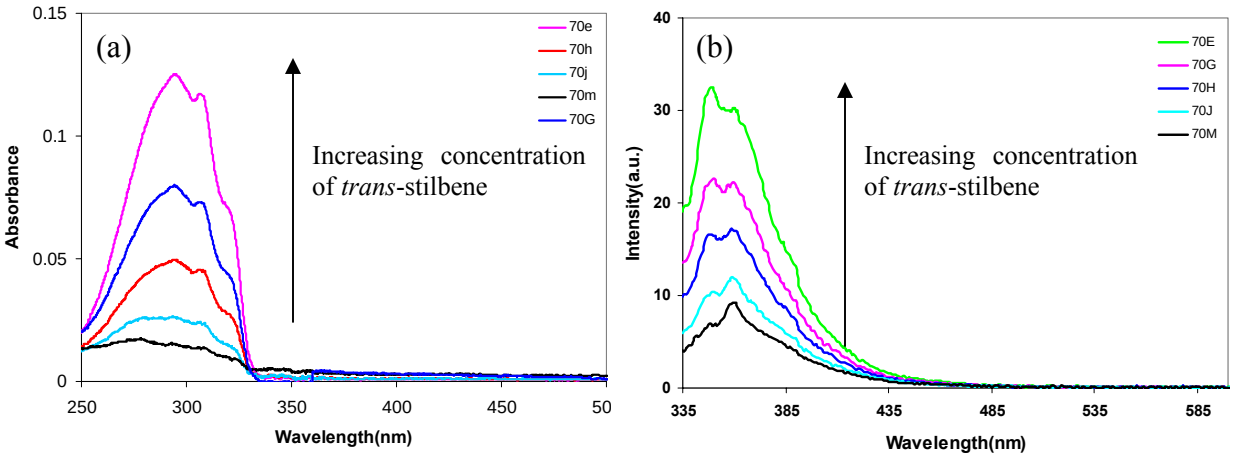

Figure A4 An example of the absorption (a) and emission data (b) obtained for five different concentrations of the standard sample of *trans*-stilbene.

3. Record the absorbance and fluorescence spectrum of the test samples in the same way as preparing the standard sample.

4. Plot graphs of integrated fluorescence intensity *vs* absorbance of both the standard sample and test sample. To integrate fluorescence intensity, softwares, like Origin, can be used. After integration, the result should be a straight line with gradient and intercept (= 0) as can be seen in the example of Figure A5. R^2 value should be close to 1.

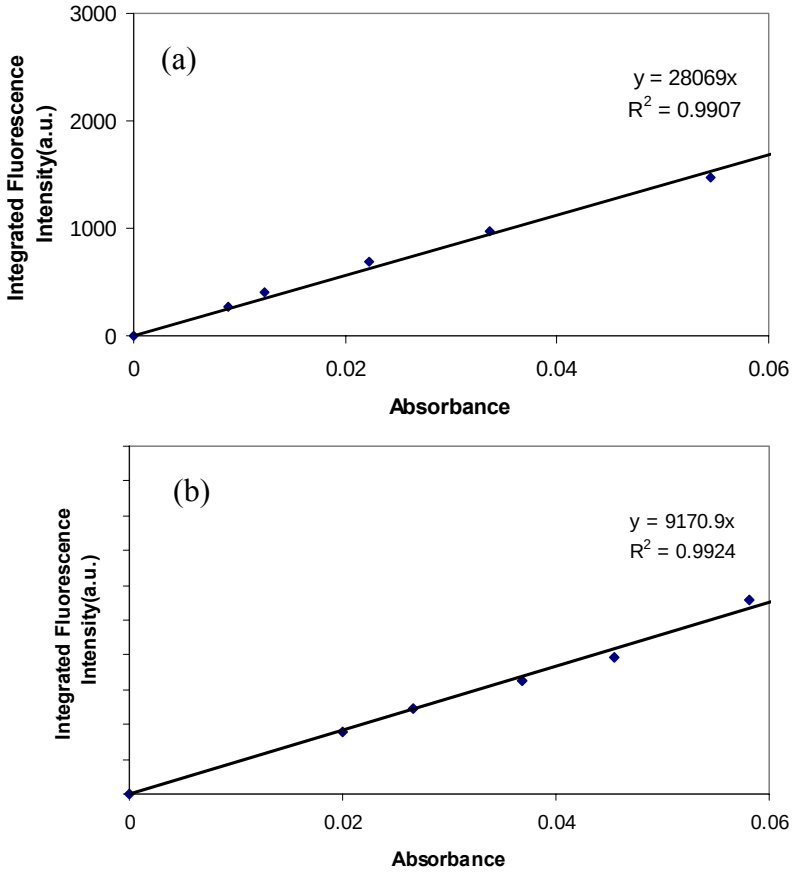

Figure A5. Linear plots for a standard sample, *trans*-stilbene (a) and a hybrid sample, 2D-[Cd_2S_2(*ba*)] (b)

5. Calculate quantum yield using Equation (1).

$$\Phi_X = \Phi_{ST}\left(\frac{Grad_X}{Grad_{ST}}\right)\left(\frac{\eta_X^2}{\eta_{ST}^2}\right)$$

For my experiments, I've used trans-stilbene as a standard in hexane. Hybrid material samples are dispersed in DMSO.

Data Given from literature:

Φ_{st} = 0.11 for trans-stilbene in hexane

η_{st} = 1.3749 (hexane) and η_x = 1.4785 (DMSO)

$Grad_x$= 9170.9, and $Grad_{ST}$ = 28069 from Figure A5.

Φ_x , is calculated using Equation (1).

References

1. Schubert, D. W. and Dunkel, T. *Mat Res Innovat.* 2003, *7*, 314–321.

2. http://www.coatings.rutgers.edu/KeyStages.htm

3. Mitzi, D.B.; Kosbar, L.L.; Murray, C.E.; Copel, M. and Afzall, A. *Nature* 2004,*428*, 299.

4. Lee, B.I and S.Komarneni, "Chemical Processing of Ceramics" p. 413 Published by CRC Press, 2005

5. Emslie, A.G.; Bonner, F.T. and Peck, L.G. *J. Appl. Phys* 1958, *29*, 858.

6. http://www.coatings.rutgers.edu/Defects.htm

7. Fery-Forgues, S. and Lavabre, D. *J. Chem. Edu.* **1999**, 76, 1260.

8. Demas, J. N. and Crosby, G. A. *J. Phys. Chem.* **1971**, 75, 991-1024

9. Jose, R.; Zhelev, Z.; Bakalova, R.; Baba, Y. and Ishikawa, M. *Appl. Phys. Lett.* **2006,** *89*, 013115.

10. Dhami, S.; de Mello, A. J.; Rumbles, G.; Bishop, S. M.; Philips, D. and Beeby, A. *Photochem. Photobiol.* **1995**, 61, 341

11. Jobin Yvon Ltd. "A Guide to Recording Fluorescence Quantum Yields" from the website: http://www.jobinyvon.com/SiteResources/Data/MediaArchive/files/Fluorescence/applications/quantumyieldstrad.pdf

Curriculum Vita

Wooseok Ki

EDUCATION:

2003~2008 Ph.D. in Chemistry, Department of Chemistry and Chemical Biology
Rutgers, The State University of New Jersey, New Brunswick, USA

2001~2003 M.S. in Materials Science,
Department of Chemical Engineering and Materials Science.
Stevens Institute of Technology, Hoboken, USA

1992~1998 B.S. in Materials Science Engineering,
Department of Materials Science and Engineering.
Ajou University, Suwon, South Korea

PUBLICATIONS:

• S. Park, W. Ki, J. Yu, and H. Du " Sol-gel Synthesis of Highly dispersed Cobalt Nanoparticles on Silica Thin Films" *J. Mater. Res*. 20, 3094 (**2005**)

• W. Ki, X. Huang, J. Li, D. Young and Y. Zhang " Highly Conductive Group VI Transition Metal Dichalcogenide Films by Solution Processed Deposition" *J. Mater. Res.* 22, 1390 (**2007**)

• J. Li, W. Bi, W. Ki, X. Huang, and S. Reddy "Nanostructured Crystals: Unique Hybrid Semiconductors Exhibiting Nearly Zero and Tunable Uniaxial Thermal Expansion Behavior" *J. Am. Chem. Soc*. 129, 14140 (**2007**)

• W. Ki and J. Li. "A Semiconductor Bulk Material That Emits Direct White Light"
J. Am. Chem. Soc. **2008**, 130, 8114-8115
(Highlighted in *C&EN*, 2008, 86, 24 and *Nature*, 2008,45, 256)